

DLR-IB-RM-OP-2016-327

**Modelling, Dynamic Analysis and
Robotic Control Strategies for the
Deorbiting Operations of the ESA
Satellite Envisat**

Masterarbeit

Mario Corso



DLR

**Deutsches Zentrum
für Luft- und Raumfahrt**

MASTERARBEIT

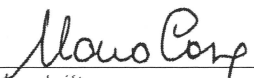
**MODELLING, DYNAMIC ANALYSIS AND
ROBOTIC CONTROL STRATEGIES FOR
THE DEORBITING OPERATIONS OF THE
ESA SATELLITE ENVISAT**

Freigabe:

Der Bearbeiter:

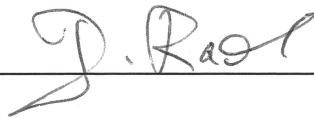
Unterschriften

Mario Corso



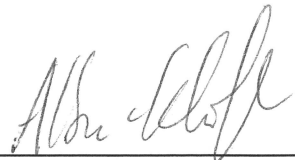
Betreuer:

Wolfgang Rackl



Der Institutsdirektor

Prof. Dr. Alin Albu-Schäffer



Dieser Bericht enthält 106 Seiten, 69 Abbildungen und 7 Tabellen



SAPIENZA
UNIVERSITÀ DI ROMA

MASTER IN SPACE & ASTRONAUTICAL ENGINEERING

**Modelling, Dynamic Analysis and Robotic
Control Strategies for the Deorbiting
Operations of the ESA Satellite Envisat**

Author

Mario CORSO

Supervisors

Prof. Paolo GASBARRI
Dr. Roberto LAMPARIELLO
MSc. Wolfgang RACKL

May 16, 2016

Abstract

This master thesis was developed in the context of the e.Deorbit project. Firstly, the force for the deorbiting manoeuvre was analysed in order to find a profile that does not induce detachment between the Servicer module and Envisat when a clamping mechanism is not considered.

Then, the proposed configurations with a four points clamping connection and a clamping to the payload adapter of Envisat were modelled and analysed. A special focus was posed on the flexibility of the 16 meter long solar panel of Envisat: this was considered divided in rigid sections and flexible joints.

Additionally, the detumbling manoeuvre was analysed in order to validate the feasibility of this manoeuvre with the robotic arm grasped to the target.

The main part of the work was to analyse a closed loop configuration: the aim was to reduce the oscillation of the solar panel during the deorbiting operations. In order to simulate that configuration, a the Loop Joint method by Featherstone was implemented and included in the SpaceDyn library. After testing the written algorithms, a damping control was simulated.

Contents

1	Introduction	1
1.1	Space Debris	1
1.2	Clean Space Programme	3
1.3	State of the Art	3
2	e.Deorbit Project	5
2.1	Envisat	5
2.2	Target Analysis	6
2.2.1	Overview	6
2.2.2	Solar Panel	8
2.2.3	Orbit & Attitude	9
2.3	Servicer Module Concept	10
2.3.1	General Design	10
2.3.2	Robotic Arm Configuration	10
2.3.3	Gripper Design	11
2.3.4	Clamping Mechanism	12
3	Mono Dimensional Analysis	14
3.1	Problem Statements	14
3.2	Model Definition	14
3.3	Detachment Analysis. Analytical Approach	15
3.4	Detachment Analysis. Parametrical Approach	17
3.4.1	Stiffness & Damping Parameters	18
3.4.2	Force Frequency Modulation	20
3.4.3	Force Amplitude Modulation	23
3.5	Torque on Robotic Arm	26
3.5.1	Model Assumptions	26
3.5.2	Results	27
4	Three Dimensional Analysis	29
4.1	Problem Statements	29
4.2	Theoretical Background	29
4.3	SpaceDyn Library	30

4.4	Simpack Environment	33
4.5	Deorbiting Scenarios	34
4.5.1	Clamping on Top	34
4.5.2	Clamping on Payload Adapter	43
4.5.3	Clamping on Payload Adapter - Rotated	53
4.6	Detumbling Scenarios	59
5	Closed Loop Systems	69
5.1	Problem Statements	69
5.2	Theoretical Background	69
5.2.1	Loop Constraint Equations	72
5.2.2	Constraint Stabilisation	73
5.2.3	Loop Joint Forces	74
5.2.4	Model Assumptions	74
5.2.5	Description of the Implemented Algorithm	75
5.2.6	Code Testing	77
5.3	Damping Control	78
5.3.1	Clamping on Payload Adapter - Configuration 1	78
5.3.2	Clamping on Payload Adapter - Configuration 2	85
6	Conclusion & Future Work	90
6.1	Conclusions	90
6.2	Future Works	91
	Appendix A Integration Methods	92
	References	94

List of Figures

1.1	Space objects around the Earth (diameter ≥ 10 cm). Credit ESA.	1
1.2	Effective number of objects in Earth orbit by object type. Credit NASA.	2
2.1	Concept of Envisat in orbit. Credit ESA.	6
2.2	Envisat dimensions. Credit Airbus Space & Defence.	7
2.3	Reference system of Envisat. Credit Airbus Space & Defence.	7
2.4	Envisat solar panel dimension and orientation. Credit Airbus Space & Defence.	9
2.5	The design of the 7-Dof manipulator in the stowed (a) and stretched (b) configurations.	11
2.6	Envisat payload adapter. Picture taken during the satellite integration. Credit ESA.	12
2.7	Current gripper design and grasped position.	13
2.8	Clamping mechanism in closed and open position.	13
3.1	1D model representation.	14
3.2	Representation of the connection between the chaser satellite and Envisat.	18
3.3	1D simulation with different stiffness parameters.	19
3.4	1D simulation with different damping parameters.	20
3.5	1D simulation with different force frequencies.	21
3.6	1D simulation with resonance response.	22
3.7	1D simulation with triggered force profile.	24
3.8	1D simulation with amplitude modulation of force profile.	25
3.9	2D Model representation.	26
3.10	Simulation on the torques produced by the detachment on the end effector.	28
4.1	Sample system with the enumeration of bodies.	32
4.2	Representation of the clamping on top deorbiting configuration.	34
4.3	2D Sketch of the Phase A configuration with reference frames.	35
4.4	Scheme of the system implemented for the target satellite.	36

4.5	Scheme of the system implemented for the servicer satellite. . .	37
4.6	Clamping in four point mechanism concept, opened and closed.	39
4.7	Position of the centre of gravity of the entire system during the simulation.	40
4.8	Velocity of the main bodies of the system.	41
4.9	Connection force acting in the clamping mechanism (sum). . .	42
4.10	Rotation of the section of Envisat's solar panel.	42
4.11	Representation of the clamping on payload adapter deorbiting configuration.	43
4.12	Scheme of the system implemented.	43
4.13	2D Sketch of the Phase B configuration with reference frames.	44
4.14	Velocity of the CoG of the system.	48
4.15	Position of the centre of gravity of the entire system during the simulation.	49
4.16	Connection force and torque provided by the clamping mech- anism in absolute value.	50
4.17	Rotation of the spherical joints of the boom.	51
4.18	Rotation of the section of Envisat's solar panel.	51
4.19	Position of the tip of the solar panel in Envisat RS.	52
4.20	Representation of the clamping on payload adapter in rotated configuration.	53
4.21	Position of the centre of gravity of the entire system during the simulation.	54
4.22	Velocity of the CoG of the system.	55
4.23	Connection force and torque provided by the clamping mech- anism in absolute value.	56
4.24	Rotation of the spherical joints of the boom.	57
4.25	Rotation of the section of Envisat's solar panel.	57
4.26	Position of the tip of the solar panel in Envisat RS.	58
4.27	Representation of the system for detumbling configuration. . .	59
4.28	Representation of the Chaser Geometry Fixed Frame.	59
4.29	Force applied by the thruster on the Chaser base to stabilize a rotation around x -axis (Scenario 1).	63
4.30	Torque applied by the thruster on the Chaser base to stabilize a rotation around x -axis (Scenario 1).	63
4.31	Torque in the arm Joint during the stabilisation of Scenario 1.	64
4.32	Force applied by the thruster on the Chaser base to stabilize a rotation around y -axis (Scenario 2).	65
4.33	Torque applied by the thruster on the Chaser base to stabilize a rotation around y -axis (Scenario 2).	65
4.34	Torque in the arm Joint during the stabilisation of Scenario 2.	66
4.35	Force applied by the thruster on the Chaser base to stabilize a rotation around z -axis (Scenario 3).	67

4.36	Torque applied by the thruster on the Chaser base to stabilize a rotation around z -axis (Scenario 3).	67
4.37	Torque in the arm Joint during the stabilisation of Scenario 3.	68
5.1	Representation of a closed loop configuration (left) with the selected loop joints in red and the corresponding spanning tree configuration (right).	70
5.2	Example of virtual cutting a closed loop system to an equivalent one that respect the assumptions made.	75
5.3	Model representations for the first configuration of the closed loops analysis.	79
5.4	Position of the end effector of the manipulator in the closed loop simulation compared with the position of the grasping point in the open loop simulation; grasping point: middle of the boom.	81
5.5	Position of the end effector of the manipulator in the closed loop simulation compared with the position of the grasping point in the open loop simulation; grasping point: end of the boom close to the first solar panel segment.	82
5.6	Position of the Envisat's solar panel tip.	83
5.7	Torques in the joint produced by the passive damping of the solar panel oscillations.	84
5.8	Model representations for the second configuration of the closed loops analysis.	85
5.9	Position of the end effector of the manipulator in the closed loop simulation compared with the position of the grasping point in the open loop simulation; grasping point: middle of the boom; tilted clamping position.	86
5.10	Position of the end effector of the manipulator in the closed loop simulation compared with the position of the grasping point in the open loop simulation; grasping point: end of the boom close to the first solar panel segment; tilted clamping position.	87
5.11	Position of the Envisat's solar panel tip; tilted clamping position.	88
5.12	Torques in the joint produced by the passive damping of the solar panel oscillations; tilted clamping position.	89

List of Tables

2.1	List of Envisat parameters with the uncertainties.	8
2.2	List of orbital parameters of Envisat at the end of the mission.	10
2.3	Denavit-Hartenberg parameters of the robotic arm.	12
4.1	List of parameters of Envisat used for the simulation.	37
4.2	List of parameters of the Chaser used for the simulation.	38
4.3	List of parameters of the model used for the simulation.	47
4.4	List of parameters of the model used for the Simpack simulation of the detumbling manoeuvre.	61
5.1	Code used to calculate the closed loops constraints.	77

Chapter 1

Introduction

1.1 Space Debris

Since the launch of Sputnik 1 in 1957 the number of man-made objects in space has been constantly increasing. More than 15 000 objects that can be tracked by radar and telescopes from the ground are currently in orbit around the Earth [1].

Of these only approximately 6% are active satellites. The rest can be classified as space debris i.e. non-operational satellites, derelict launch vehicle stages, mission-related hardware and fragments resulting from explosions or collisions [2].



Figure 1.1: Space objects around the Earth (diameter ≥ 10 cm). Credit ESA.

The Chinese anti-satellite demonstration in 2007 and the impact between an active U.S. Iridium satellite and a defunct Russian Cosmos spacecraft in 2009 have greatly worsen the situation, increasing dramatically the number of fragments (Figure 1.2).

While space seemed limitless 50 years ago, the space age has demonstrated how quickly the orbits around the Earth can be filled. Space debris has evolved from an environmental nuisance to a critical hazard to functioning satellites, as well as to human space activity. In fact, the International Space Station, the Space Shuttle and many satellites have often to carry out orbital manoeuvres to avoid collisions with space junk [3].

Given the high relative velocities involved (up to approximately 15 km/s), it is obviously also a realistic threat to human spaceflight and robotic missions.

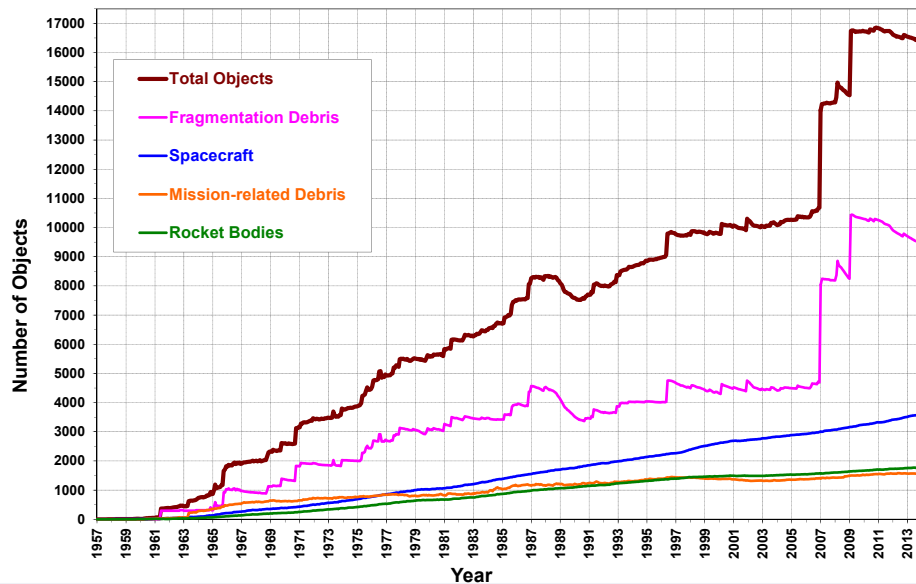


Figure 1.2: Effective number of objects in Earth orbit by object type. Credit NASA.

In particular, the LEO region, extending from the beginning of the space environment up to an altitude of 2000 km , is the most densely populated in terms of number of objects. At altitudes above the levels where atmospheric drag is significant, the time required for orbital decay is quite long. Many of these objects are going to remain in orbit for centuries or millennia [4].

Simulations have demonstrated that even if the orbital debris population remained as it is today with no further objects added to space, the level of fragmentation in LEO will continue to escalate exponentially.

This kind of instability indicates that the existing and currently proposed mitigation measures by international organizations (e.g. IADC, UN-COPUOS, space agencies) are not sufficient to stop the multiplication of space debris.

The only way to tackle this problem is to actively reduce the mass of debris in orbit. Many studies have suggested that removing five to ten large objects per year from the LEO region can prevent the debris collisions from cascading and guarantee safe access to space to future generations.

1.2 Clean Space Programme

Clean Space aims to make the European Space Agency (ESA) an exemplary space agency in the area of terrestrial and space environmental protection. It will ensure the sustainable forward-looking use of space by ESA to preserve it as a viable economic arena, continue to promote a high environmental standard for European citizens and position European industry at the foreground of new green technology markets.

Through expanding its knowledge of the environmental impact of its activities, ESA will identify environmentally friendly technologies and processes that will minimise the environmental impact of ESA's operations. Information gathered during the monitoring of environmental legislation compliance will be used to prepare and mitigate against possible supply chain disruptions through the development of alternative materials and processes.

ESA will also support and promote the interests of preserving Earth's orbital environment as a safe zone in which to operate satellites, by limiting or minimising causes of harmful interference in space activities.

1.3 State of the Art

Utilising space robotics for debris removal and servicing in orbit is a very promising approach as there have been multiple missions and investigations in the past to strengthen this line of technology. There are four major groups of robotic applications in space that can be defined. Using the Shuttle and Space Station Robotic Manipulator System (SRMS, SSRMS), respectively, the International Space Station (ISS) was assembled out of several modules by applying the principle of in-space robotic assembly (ISRA). Small robotic satellites are planned to serve for inspection purposes and NASA's Robonaut or comparable systems such as DLR's humanoid robot Justin are candidates for future EVA support operations [5].

Similar to ISRA and EVA support, dexterous robotic manipulators are planned to be utilised to capture, maintain and/or deorbit operational and defective satellites within on-orbit servicing missions. Finally, robotic exploration of other celestial bodies, such as the Moon, Near Earth Objects

(NEOs), or Mars is envisaged or has already been accomplished.

Currently, the deployment of regularly used robotic systems in space is limited to the Space Station Remote Manipulator Systems (SSRMS), the Japanese Experiment Module Remote Manipulator System (JEM-RMS), and the Mobile Servicing System (MBS) aboard ISS. The MBS also features a Special Purpose Dexterous Manipulator (SPDM). These systems can be tele-operated by the crew and are being used for extravehicular activity (EVA) support, space station assembly and vehicle docking [6].

The Shuttle Remote Manipulator System (SRMS) was also used for satellite repair operations (Hubble). In combination with the SRMS, the Orbiter Boom Sensor System (OBSS) was utilised for the inspection of the Shuttle's heat protection tiles. Recently, the Robotic Refuelling Mission (RRM) with the SPDM successfully demonstrated remote controlled robotic servicing, including refuelling with an experimental platform aboard the ISS. In addition to the robotic servicing capabilities that are bound to the Shuttle or the ISS, several satellite-based demonstrators have been brought to orbit in order to demonstrate the possibility of on-orbit servicing.

The most important demonstrators and missions are the Robot Technology Experiment (ROTEX), developed by the German Aerospace Center (DLR), the Ranger tele-robotic flight experiment (RTFX) from the University of Maryland, the Japanese Engineering Test Satellite VII (ETS-VII), the German Robotic Component Verification experiment aboard the ISS (ROKVISS), the Demonstration of Autonomous Rendezvous Technology (DART) NASA, the Experimental Small Satellite-10 and -11 (XSS-10/11), the Technology Experiment's (MiTEx), the Orbital Express mission by DARPA, as well as the German Orbital Servicing Mission (DEOS) [7] [8].

DEOS has been developed at DLR and was brought until Phase B2. The project investigated technologies to autonomously and manually perform rendezvous and proximity operations, as well as to capture a tumbling and uncooperative target satellite with a dexterous manipulator. Concerning robot technology, the results presented in this paper profited from this heritage and the gathered experience [10].

Chapter 2

e.Deorbit Project

The deorbiting of defective satellites may play a vital role in the fight against space debris: in the frame of the Clean Space Programme of ESA, a project called e.Deorbit was developed. Its main task is to develop a technology capable to capture the ESA satellite Envisat (described in Sections 2.1 and 2.2), stabilize and safely deorbit it.

e.Deorbit is designed to target debris items in well-trafficked polar orbits, between 800 km to 1000 km altitude. At around 1600 kg, e.Deorbit will be launched on ESA's Vega rocket.

A promising approach for this task is the use of a chaser satellite equipped with a robot arm. Since such a manoeuvre has never been attempted, it is important to examine whether such a task can be performed safely.

A robotic capture concept was developed that is based on a 7 Degrees of Freedom (DoF) dexterous robotic manipulator, a linear two-bracket gripper, and a clamping mechanism for achieving stiff fixation between target and chaser satellites prior to the de-tumbling and execution of the deorbit manoeuvre.

In space industry frame, e.Deorbit has completed its Phase-A preliminary analysis that began in January 2014. With many aspects already finalised, it is now moving in Phase-B1; the next milestone will be the Systems Requirements Review, due in late 2016.

2.1 Envisat

Envisat is the largest earth-observing satellite of ESA (Figure 2.1). It is an environmental satellite with a launch mass of 8221 kg which is orbiting the Earth on a sun-synchronous polar orbit at an altitude of 790 km.

Launched in 2002, it operated five years beyond its planned mission lifetime, delivering over a 1000 TByte of data. ESA was expecting to turn off the spacecraft in 2014, but the contact to Envisat was lost on April 8th, 2012. Since then, Envisat is not controllable anymore and is therefore



Figure 2.1: Concept of Envisat in orbit. Credit ESA.

considered as space debris.

At the 63rd International Astronautical Congress, Martha Mejia-Kaiser described Envisat as a large danger for other satellites. Due to little drag effects at the current altitude, Envisat will remain in the orbit of Earth for around 150 years. With the cross-section of 26 meters the probability of a collision with another satellite is very high [11].

Against the guidelines of the IADC, Envisat was operated until too little fuel was left for moving it to a lower orbit where a shorter lifetime would result. For this reason ESA could be held liable for occurring collisions.

2.2 Target Analysis

2.2.1 Overview

In this section all the data useful to the mission design and for modelling the target in this work are reported. The dimensions of the target are depicted in Figure 2.2, all the measures are expressed in mm . A definition of the first Reference Frame is also included (Figure 2.3); it is a right-handed orthogonal with the origin in the geometrical centre of the launcher interface plane:

- x -axis (pitch axis) going through the main body of Envisat directed towards the solar array,

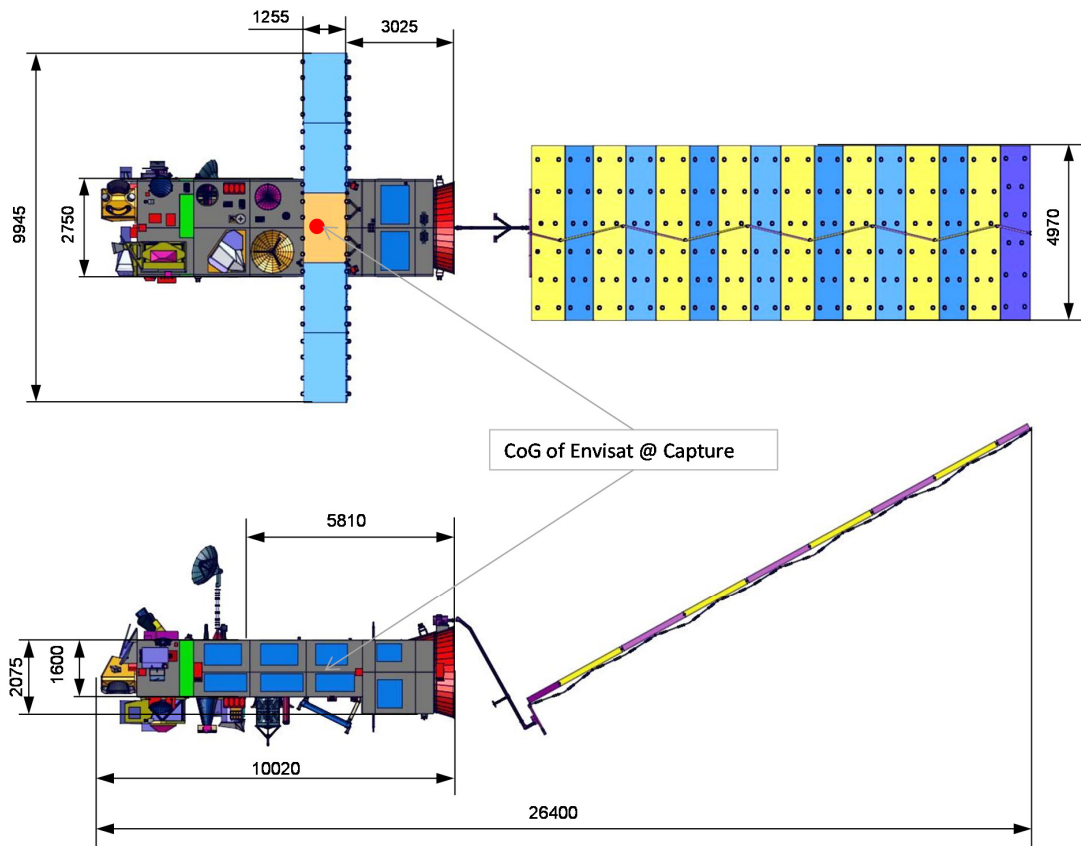


Figure 2.2: Envisat dimensions. Credit Airbus Space & Defence.

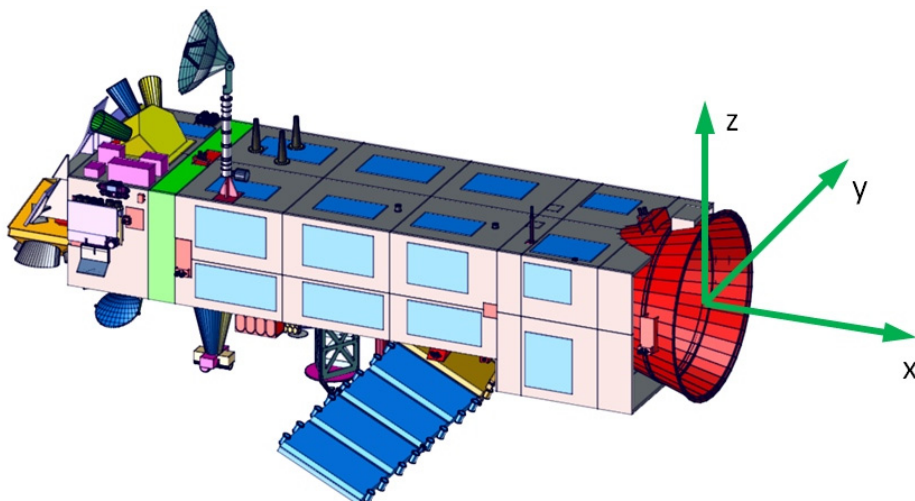


Figure 2.3: Reference system of Envisat. Credit Airbus Space & Defence.

- y -axis (roll axis) parallel to the ASAR antenna, antiparallel to the velocity direction,
- z -axis (yaw axis) roughly antiparallel to the direction of Earth completing the frame.

The mass parameter in Table 2.1 includes the propellant (hydrazine) left of about 36 kg . The Centre of Gravity (CoG) is calculated including the weight of the solar panel and the Inertia matrix is expressed with respect to the CoG [12].

	Value			Uncertainty		
Mass [kg]	7828			± 30		
CoG [mm]	X_G	-3905		± 0.01		
	Y_G	-9		± 0.004		
	Z_G	3		± 0.004		
Inertia Matrix [$kg\ m^2$]	17023	397.1	-2171	± 350	± 100	± 250
		124826	344.2		± 3000	± 150
	<i>sym</i>		129112	<i>sym</i>		± 3000

Table 2.1: List of Envisat parameters with the uncertainties.

2.2.2 Solar Panel

The size of the deployed solar array is 16 $m \times 4.972\ m$ and its weight is 338 kg . The solar array has two low frequencies of 0.05 Hz and 0.06 Hz . In the stowed configuration the 14 sections that composes the array were folded together.

The solar array is attached to the main body of Envisat by an axial boom: this can be rotated by the Solar Array Drive Mechanism (SADM). The SADM is located at the base of the Envisat’s payload adapter. The Primary Deployment Mechanism (PDM) provides a self-locking gear, so that no boom movements due to a back driving PDM should be expected if this mechanism is still in working conditions [13].

In Envisat operational mode the solar array was rotated to point continuously towards the sun. Seven days after the unrecoverable failure event, that resulted in the termination of the mission, the satellite was observed in-orbit by the Pleiades. These observations, on 15 April 2012, indicate that the solar panel is very close to the safe mode plane, but locked in an anti-canonical position which is unfavourable in terms of approaching Envisat directly at the payload adapter interface. This configuration is shown in Figure 2.4, all the dimensions reported are in mm .

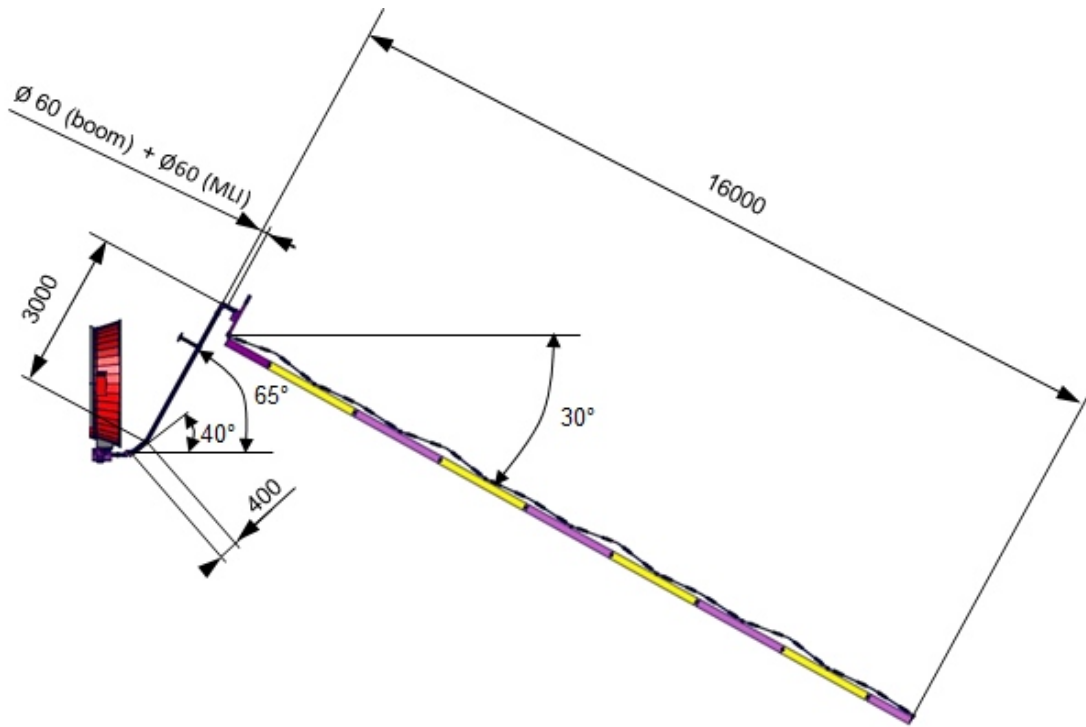


Figure 2.4: Envisat solar panel dimension and orientation. Credit Airbus Space & Defence.

2.2.3 Orbit & Attitude

ESA performed a prediction of the Envisat orbit for the period 2020-2023 relevant for the e.Deorbit mission. The prediction covers the main orbital element (reported in Table 2.2).

The prediction of the semi-major axis, eccentricity, inclination and RAAN (Descending Node, Ω) over a period of ten years is relatively robust against uncertainties in vehicle parameters, initial state and environmental conditions. Therefore this parameters should be used as reference values.

The prediction of the argument of latitude of Envisat at a certain epoch is very sensitive to uncertainties in the input parameters. Therefore, it is necessary to cover the range from 0° to 360° for the argument of latitude and other computations.

Orbital Parameter		Value
Semi-major Axis	a	7144.8 <i>km</i>
Perigee Altitude	h_p	773.1 <i>km</i>
Apogee Altitude	h_a	774.6 <i>km</i>
Eccentricity	e	0.0000982
Inclination	i	98.5°
Descending node	Ω	10:00 AM MLST

Table 2.2: List of orbital parameters of Envisat at the end of the mission.

2.3 Servicer Module Concept

2.3.1 General Design

The primary structure of the Servicer Module (SM) is a CFRP cylinder with the payload adapter at one end and the propulsion module at the other. The central cylinder is surrounded by a box-shaped metallic structure with aluminium honeycomb panels for accommodation of the electronic equipment.

The dimensions of the SM box are $2.360\text{ m} \times 2.750\text{ m} \times 2.075\text{ m}$.

The rigid capture system is composed of the robotic arm for capturing and stabilising the target satellite as well as a clamping mechanism for achieving stiff force closure during the deorbiting manoeuvre. The following sections presents the design of the arm, including the attached gripper and the clamping mechanism.

2.3.2 Robotic Arm Configuration

The 7-DoF manipulator arm has a stretched length of 4.2 m (Figure 2.5). The arm is composed of Aluminium cylindrical tubes that provide the structure for the kinematics and deal as housing for the required sensors, wiring and electronics.

A short base cylinder provides the interface to the Chaser platform by a bolted flange connection. There are four redundant electronic blocks integrated into the arm assembly for controlling the seven identical joints. The elbows of the manipulator arm are specially welded housings, providing access from the side to the interior via removable cover plates fixed on the sides.

Based on the third generation of lightweight robot (LWR) technology and thereof derived, robot joints that were previously space-proven for five years outside the Russian service module within the ROKVISS experiment, highly integrated and qualifiable joints were developed following ECSS specifications, in order to meet the requirements of future on-orbit servicing (OOS) missions [14].

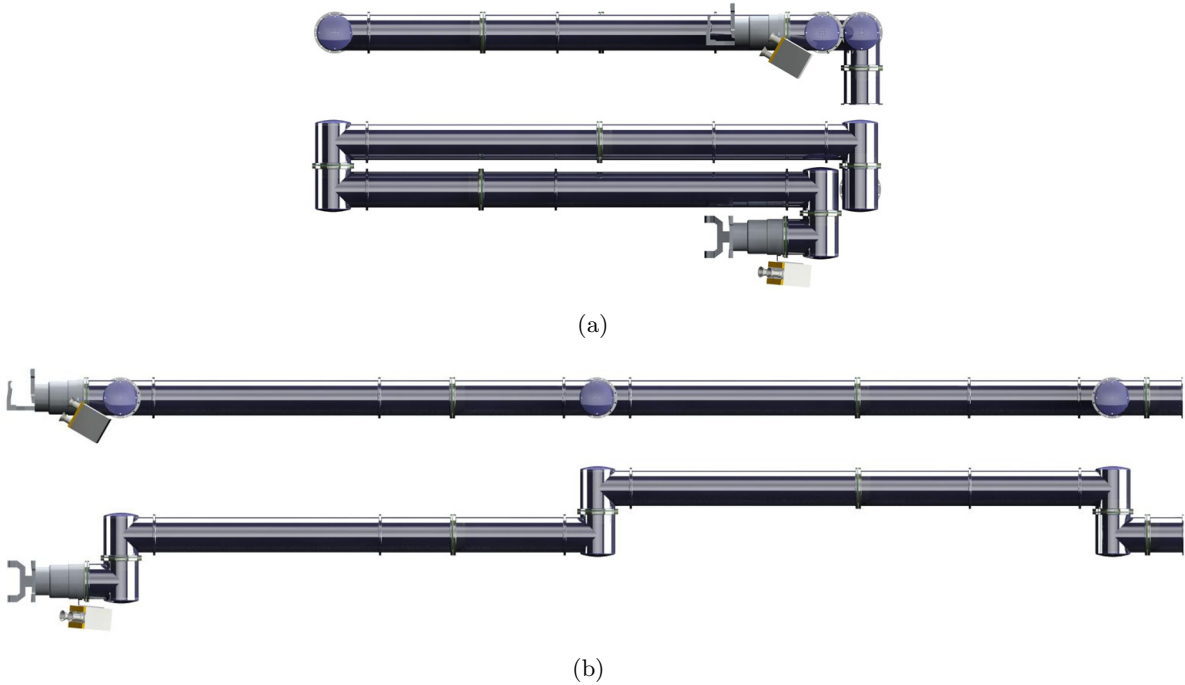


Figure 2.5: The design of the 7-Dof manipulator in the stowed (a) and stretched (b) configurations.

The Denavit-Hartenberg parameters for the manipulator are reported in Table 2.3. Following the joint specifications, the arm supports an approximate maximal torque of 160 Nm and a force of 35 N at its tool center point (TCP) or end-effector. The joints reach a max. speed of 10 deg/s .

2.3.3 Gripper Design

The design of the gripper for e.Deorbit is very target-oriented, as the payload adapter is a structure where effective force closure must be achieved (Figure 2.6).

Figure 2.7 shows the current gripper design and the initial grasp position. Due to the form of the brackets, the design is robust to possible positioning error up to $\pm 20 \text{ mm}$ in the x -direction and $\pm 30 \text{ mm}$ in y , while z is irrelevant through the radial form of the adapter ring. With the arm being in compliant mode during the grasp, it is pulled into the right position upon gripper closure.

During deorbit manoeuvre, after Envisat is secured using the clamping mechanism, the arm is repositioned and it can be used to hold onto the solar panel boom for position measurement and active damping of the occurring

Joint	Type	a [mm]	α [deg]	θ [deg]	d [mm]
1	Roll	0	0	0	256
2	Pitch	0	-90	0	168
3	Roll	0	90	180	1900
4	Pitch	0	-90	0	168
5	Roll	0	90	180	1730
6	Pitch	0	90	0	168
7	Roll	0	-90	0	350

Table 2.3: Denavit-Hartenberg parameters of the robotic arm.

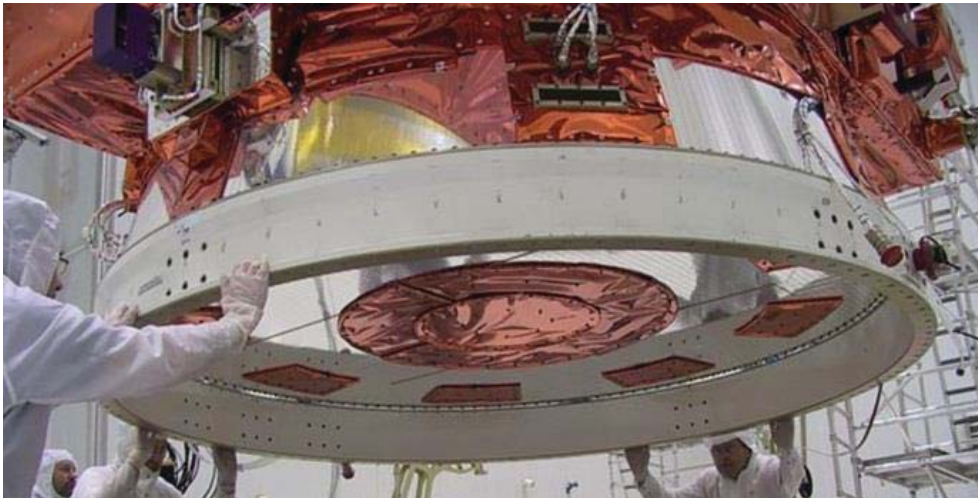


Figure 2.6: Envisat payload adapter. Picture taken during the satellite integration. Credit ESA.

oscillations. The gripper must at least support the forces and torque specification of the arm joint in order to be in line with the general arm design.

2.3.4 Clamping Mechanism

A stiff force closure between chaser and target spacecraft for detumbling and deorbit manoeuvres is achieved by a four-armed clamping device. The device consists of two similar mechanisms driven by spindle actuators as shown in Figure 2.8.

At four interface points the fixation is realised by form closure in y -direction and by friction in x and z -direction. The clamping force is dimensioned such, that deorbit and attitude control thrust can be transmitted by friction at a high safety margin, while assuring that sandwich panels on the target are not damaged [15].

The separate actuation of the two mechanisms allows compensating of

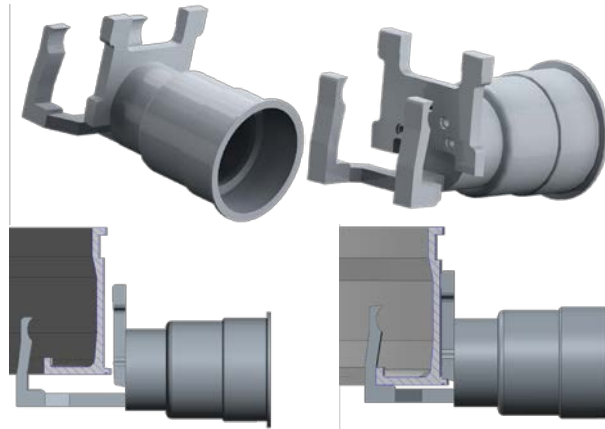


Figure 2.7: Current gripper design and grasped position.

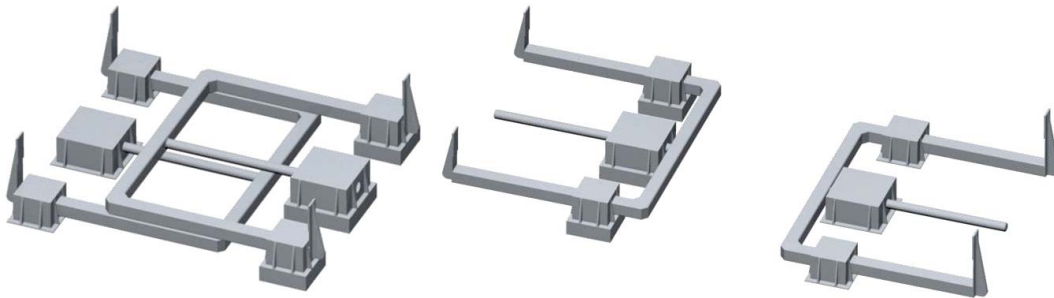


Figure 2.8: Clamping mechanism in closed and open position.

CoG mismatch and uncertainty of $\pm 100 \text{ mm}$ in y -direction. Surface irregularities on the Target surface of up to 50 mm can be tolerated. Finite Element analyses prove that a high stiffness of the chaser-target compound with eigenfrequencies above 2 Hz can be achieved.

Chapter 3

Mono Dimensional Analysis

3.1 Problem Statements

The deorbiting phase of this mission is complex and should be planned in the best possible configuration: in order to do this a first mono dimensional model was analysed. The aim was to find a force profile capable to do not induce detachment between the servicer module and Envisat, for every kind of connection proposed.

A configuration that allows this detachment is not acceptable, because this induce the system of the two satellite to be unstable. In fact, the multiple thrust phases (at least 5) are separated by the time necessary to get the perigee of the orbit and a detachment produced by the precedent phase could effect negatively the successive thrust phase.

For these reasons, a one dimensional dynamic case was analysed, that is based on a mass-spring-damper system. First the mathematical statements of the problem are established and an analytical solution is explained; then the parametric dependences of the detachment between the Servicer and Envisat are examined.

3.2 Model Definition

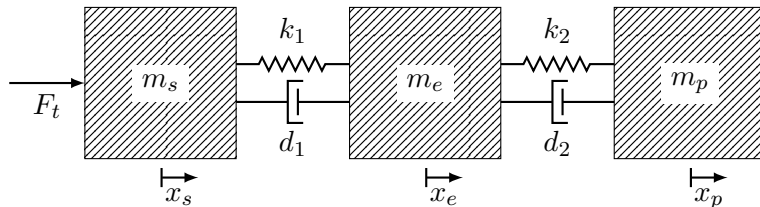


Figure 3.1: 1D model representation.

The mono dimensional system is composed by:

- the Servicer (m_s);
- Envisat (m_e);
- solar panel of Envisat (m_p).

The input force is derived from the deorbiting Thrust (F_t); a representation of this model is shown in Figure 3.1.

3.3 Detachment Analysis. Analytical Approach

This simple case can be solved analytically, so it is possible to find the minimum impulsive force applied that is not acceptable (since the condition $x_e - x_s \leq 0$ is not respected) [18].

The system to solve is:

$$m_s \ddot{x}_s - k_1 (x_e - x_s) = F_t \quad (3.1a)$$

$$m_e \ddot{x}_e + k_1 (x_e - x_s) - k_2 (x_p - x_e) = 0 \quad (3.1b)$$

$$m_p \ddot{x}_p + k_2 (x_p - x_e) = 0 \quad (3.1c)$$

By putting $\Delta x_1 = x_e - x_s$ and $\Delta x_2 = x_p - x_e$ and recaving the relative accelerations by subtracting Eq. (3.1a) from Eq. (3.1b) and Eq. (3.1b) from Eq. (3.1c):

$$\Delta \ddot{x}_1 + \left(\frac{1}{m_e} + \frac{1}{m_s} \right) k_1 \Delta x_1 - \frac{k_2}{m_e} \Delta x_2 = -\frac{F_t}{m_s} \quad (3.2a)$$

$$\Delta \ddot{x}_2 - \frac{k_1}{m_e} \Delta x_1 + \left(\frac{1}{m_e} + \frac{1}{m_p} \right) k_2 \Delta x_2 = 0 \quad (3.2b)$$

And writing it in a matricial form, it follows that:

$$\Delta \ddot{\mathbf{x}} + \mathbf{K} \Delta \mathbf{x} = \mathbf{F} \quad (3.3)$$

with:

$$\mathbf{K} = \begin{bmatrix} k_1/m_1 & -k_2/m_e \\ -k_1/m_e & k_2/m_2 \end{bmatrix}$$

$$m_1 = \frac{m_e m_s}{m_e + m_s} \quad m_2 = \frac{m_e m_p}{m_e + m_p}$$

$$\mathbf{F} = \begin{bmatrix} -F_t/m_s \\ 0 \end{bmatrix}$$

This solution of this system is the sum of the solution of the homogeneous associated problem and a particular solution.

$$\Delta \mathbf{x} = \Delta \mathbf{x}_{hom} + \Delta \mathbf{x}_{part} \quad (3.4)$$

$$\Delta \mathbf{x}_{hom} = A \boldsymbol{\varphi}_1 \sin(\omega_1 + \psi_1) + B \boldsymbol{\varphi}_2 \sin(\omega_2 + \psi_2) \quad (3.5)$$

In which ω_i^2 are the eigenvalues of \mathbf{K} and $\boldsymbol{\varphi}_i$ are the correspondent eigenvector and the constants A, B, ψ_1 and ψ_2 are chosen by imposing the initial conditions ($\Delta \dot{\mathbf{x}} = 0$ and $\Delta \mathbf{x} = 0$).

$$\Delta \mathbf{x}_{part} = \mathbf{K}^{-1} \mathbf{F} = -\frac{F_t}{m_s} \frac{m_1 m_e}{m_e^2 - m_1 m_2} \begin{bmatrix} m_e/k_1 \\ m_2/k_2 \end{bmatrix} \quad (3.6)$$

After some calculations, it is possible to know the exact formula of relative distances, in dependence of masses, spring constants (resulting from structural elasticity) and force applied by thrusters.

The eigenvalues, eigenvectors and constants A, B, ψ_1 and ψ_2 can be obtained as:

$$\lambda_{1,2} : \quad |\mathbf{K} - \lambda_i \mathbf{I}| = 0 \quad (3.7)$$

$$\omega_{1,2}^2 = \lambda_{1,2} = \frac{1}{2} \left(\frac{k_1}{m_1} + \frac{k_2}{m_2} \pm \alpha \right) \quad (3.8)$$

$$\text{with} \quad \alpha = \sqrt{\left(\frac{k_1}{m_1} - \frac{k_2}{m_2} \right)^2 + 4 \frac{k_1 k_2}{m_e^2}}$$

$$\boldsymbol{\varphi}_1 = \begin{bmatrix} \varphi_{11} \\ \varphi_{12} \end{bmatrix} = \begin{bmatrix} \frac{m_e}{2k_1} \left(\frac{k_2}{m_2} - \frac{k_1}{m_1} + \alpha \right) \\ 1 \end{bmatrix} \quad (3.9a)$$

$$\boldsymbol{\varphi}_2 = \begin{bmatrix} \varphi_{21} \\ \varphi_{22} \end{bmatrix} = \begin{bmatrix} \frac{m_e}{2k_1} \left(\frac{k_2}{m_2} - \frac{k_1}{m_1} - \alpha \right) \\ 1 \end{bmatrix} \quad (3.9b)$$

$$\psi_1 = \psi_2 = \pi/2 \quad (3.10)$$

$$A = \frac{F_t}{m_s} \frac{m_1 m_e}{m_e^2 - m_1 m_2} \left(\frac{m_e}{k_1} + \varphi_{21} \frac{m_2}{k_2} \right) \frac{1}{\varphi_{11} - \varphi_{21}} \quad (3.11a)$$

$$B = \frac{F_t}{m_s} \frac{m_1 m_e}{m_e^2 - m_1 m_2} \left(\varphi_{11} \frac{m_2}{k_2} - \frac{m_e}{k_1} - 2\varphi_{21} \frac{m_2}{k_2} \right) \frac{1}{\varphi_{11} - \varphi_{21}} \quad (3.11b)$$

In conclusion, with this simple analysis it is possible to know in which case there is detachment, depending upon the value of the stiffness and the force applied by thrusters.

It is also possible to verify that if the force is constant and positive the detachment is not occurring, but when the force ceases (end of the thrust profile) the detachment occurs. This would be explained and shown better in the following parametrical analysis.

3.4 Detachment Analysis. Parametrical Approach

The same system (Figure 3.1) is used for the Matlab implementation, by adding the damping to the Eq. (3.1) and remembering the definitions of $\Delta x_1 = x_e - x_s$ and $\Delta x_2 = x_p - x_e$, the governing equations to solve are:

$$m_s \ddot{x}_s - k_1 \Delta x_1 - d_1 \Delta \dot{x}_1 = F_t \quad (3.12a)$$

$$m_e \ddot{x}_e + k_1 \Delta x_1 + d_1 \Delta \dot{x}_1 - k_2 \Delta x_2 - d_2 \Delta \dot{x}_2 = 0 \quad (3.12b)$$

$$m_p \ddot{x}_p + k_2 \Delta x_2 + d_2 \Delta \dot{x}_2 = 0 \quad (3.12c)$$

The relative accelerations are obtained by subtracting:

$$\Delta \ddot{x}_1 + \left(\frac{1}{m_e} + \frac{1}{m_s} \right) (k_1 \Delta x_1 + d_1 \Delta \dot{x}_1) - \frac{1}{m_e} (k_2 \Delta x_2 + d_2 \Delta \dot{x}_2) = -\frac{F_t}{m_s} \quad (3.13a)$$

$$\Delta \ddot{x}_2 - \frac{1}{m_e} (k_1 \Delta x_1 + d_1 \Delta \dot{x}_1) + \left(\frac{1}{m_e} + \frac{1}{m_p} \right) (k_2 \Delta x_2 + d_2 \Delta \dot{x}_2) = 0 \quad (3.13b)$$

And writing it in matrices:

$$\Delta \ddot{\mathbf{x}} + \mathbf{D} \Delta \dot{\mathbf{x}} + \mathbf{K} \Delta \mathbf{x} = \mathbf{F} \quad (3.14)$$

with:

$$\mathbf{D} = \begin{bmatrix} d_1/m_1 & -d_2/m_e \\ -d_1/m_e & d_2/m_2 \end{bmatrix}$$

$$\mathbf{K} = \begin{bmatrix} k_1/m_1 & -k_2/m_e \\ -k_1/m_e & k_2/m_2 \end{bmatrix}$$

$$m_1 = \frac{m_e m_s}{m_e + m_s} \quad m_2 = \frac{m_e m_p}{m_e + m_p}$$

$$\mathbf{F} = \begin{bmatrix} -F_t/m_s \\ 0 \end{bmatrix}$$

The impulsive force F_t could vary in frequency, but it has a fixed module of 450 N. All the masses are constant, because they are not the subject of the study and the parameter that could vary are the stiffness and damping constants:

- mass of chaser sat., $m_s = 1599 \text{ kg}$;
- mass of Envisat, $m_e = 7827 \text{ kg}$;
- mass of solar panel, $m_p = 338 \text{ kg}$;

The connection between Envisat and its solar panel has been represented as a low stiffness and low damping connection:

- $k_2 = 800 \text{ N/m}$;
- $d_2 = 800 \text{ Ns/m}$.

3.4.1 Stiffness & Damping Parameters

The connection between the Chaser and Envisat is the first subject of the parametric study conducted. It is assumed to be a rigid connection with high stiffness and low damping coefficients.

The stiffness parameter is evaluated representing the connection as a plate in contact with Envisat and with two boundaries fixed to the chaser (Figure 3.2). In this case, there is a simple formula to evaluate the stiffness of this plate (setting the characteristic of iron or aluminium, for a thickness h of 10 mm):

$$k_1 = \frac{2Eh^3}{3(1-\nu^2)} \quad (3.15)$$

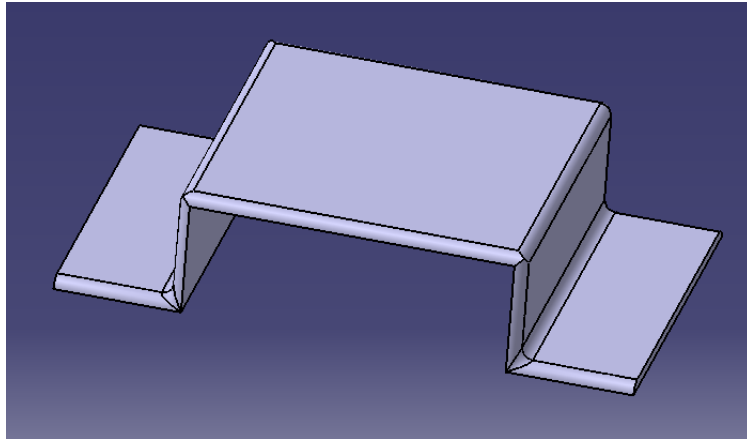


Figure 3.2: Representation of the connection between the chaser satellite and Envisat.

According to Eq. (3.15), the ranges considered were:

- k_1 from 60 000 to 100 000 N/m ;

- d_1 from 1200 to 4000 Ns/m .

Varying the stiffness coefficient means to change the steady state value of the displacement, while varying the damping constant means to reach the steady state in different times.

These assumptions are confirmed by the results: in Figure 3.3 are showed the variations about the stiffness parameter and in Figure 3.4 about the damping.

In every case there is detachment when the force is switched off, as previously supposed in the analytical approach. It is necessary to analyse better if it is possible to avoid the detachment only modifying the force frequency or its amplitude.

The constant parameters used in these analyses are: $k_2 = 800 N/m$, $d_2 = 800 Ns/m$, $F_t = 450 N$ at $t = 1 s$.

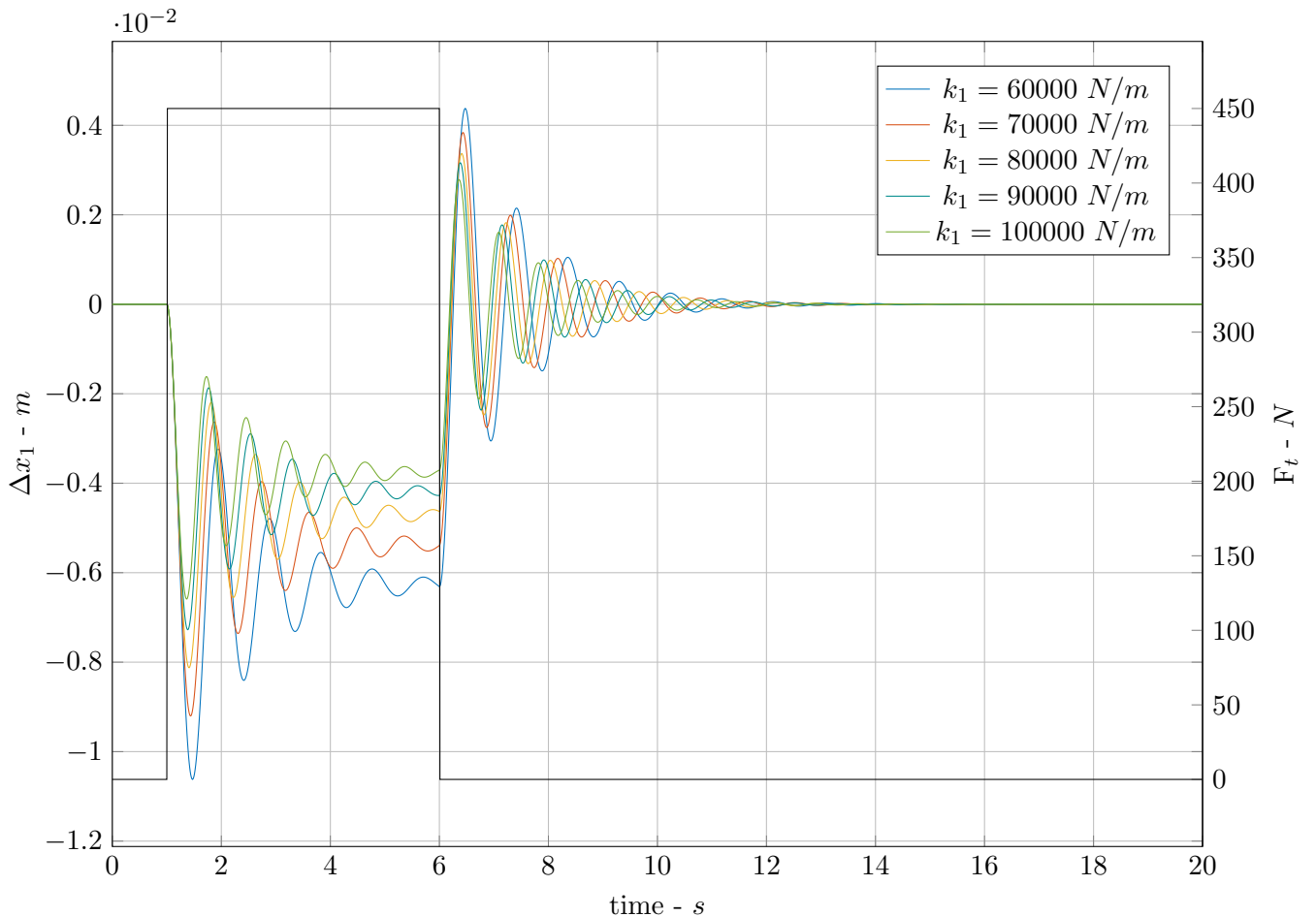


Figure 3.3: 1D simulation with different stiffness parameters.

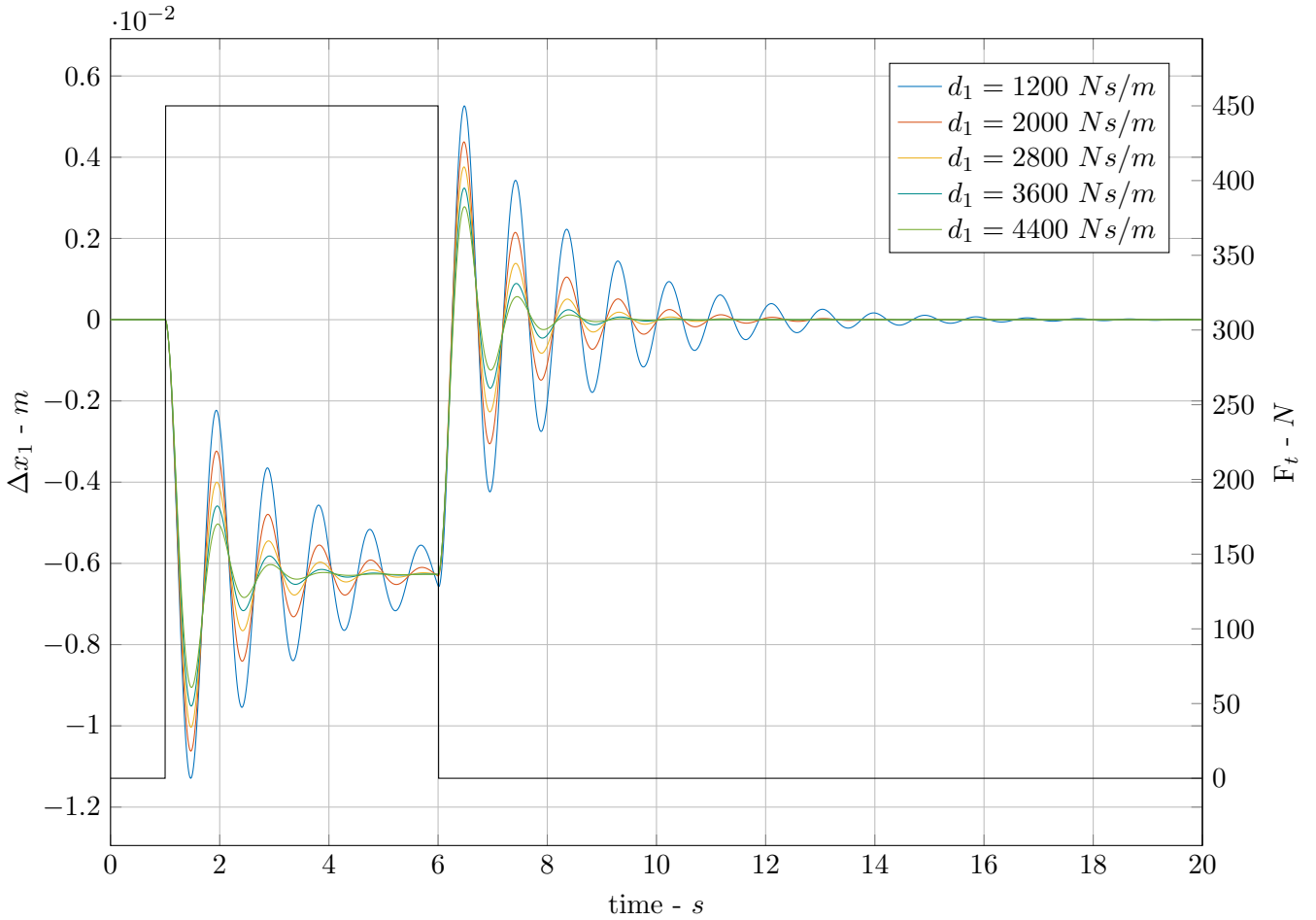


Figure 3.4: 1D simulation with different damping parameters.

3.4.2 Force Frequency Modulation

For the previous analysis a single step force of 5 s was taken into account: it is possible to turn on and off the thrusters and provide a frequency to the force.

This analysis is conducted to find a particular force profile that does not provide the detachment. The result are in Figure 3.5 and the constant parameters used in this analysis are: $k_1 = 60000 \text{ N/m}$, $d_1 = 1200 \text{ Ns/m}$, $k_2 = 800 \text{ N/m}$, $d_2 = 800 \text{ Ns/m}$, $F_t = 450 \text{ N}$ at $t = 1 \text{ s}$.

Depending on the stiffness parameters used, there are two frequency which are not safe for the system because the amplitude increase indefinitely. These derives from the eigenvalues and from Eq. (3.8) one could calculate them. The simulation with this two values is reported in Figure 3.6.

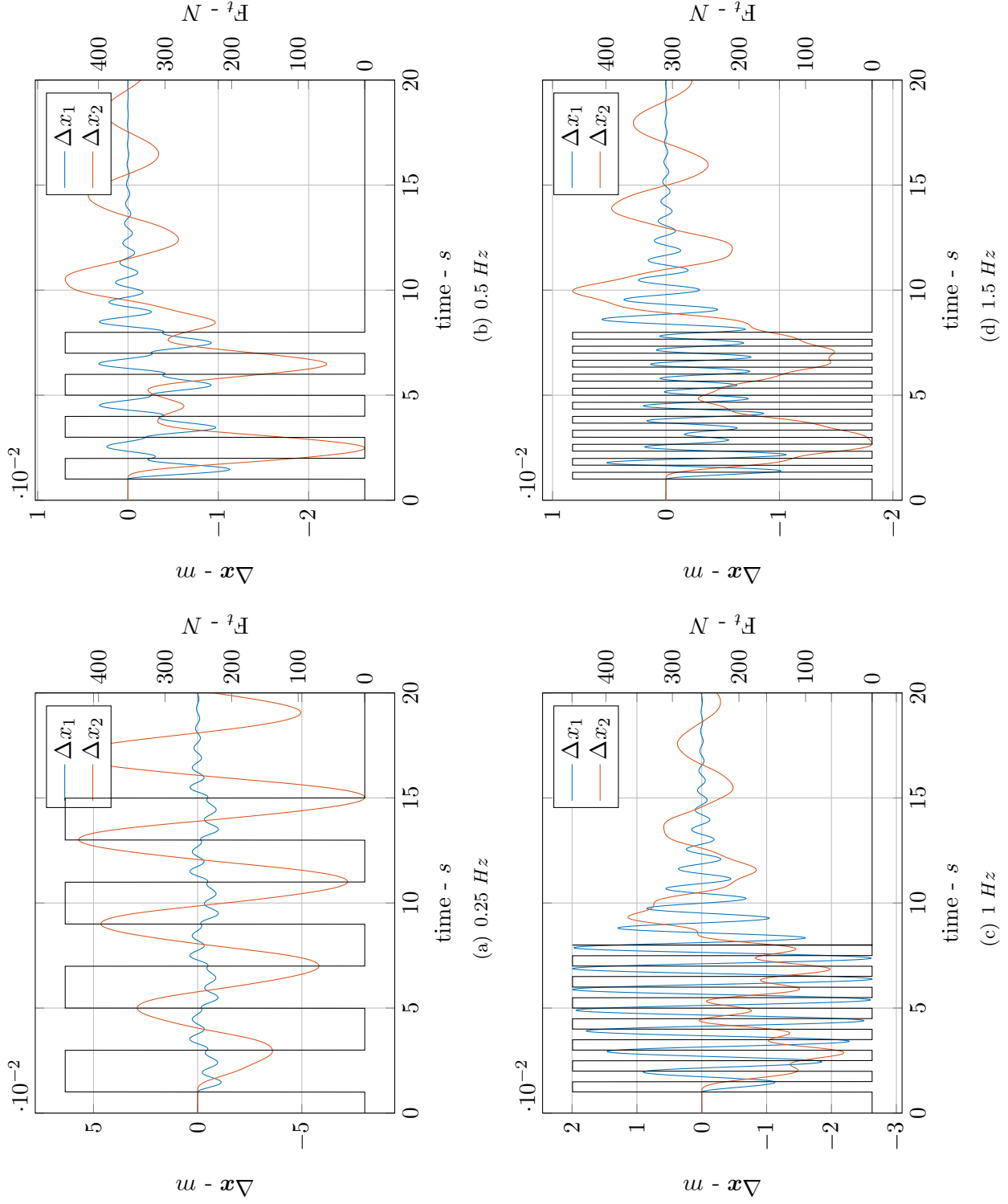
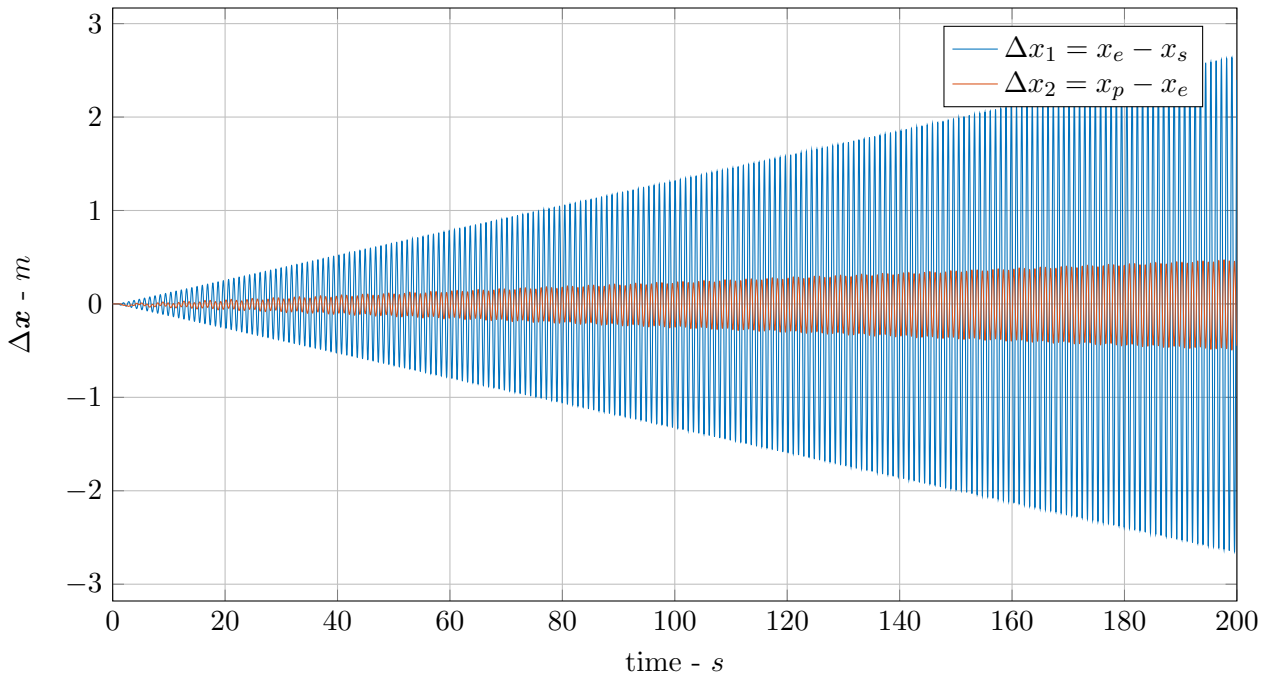
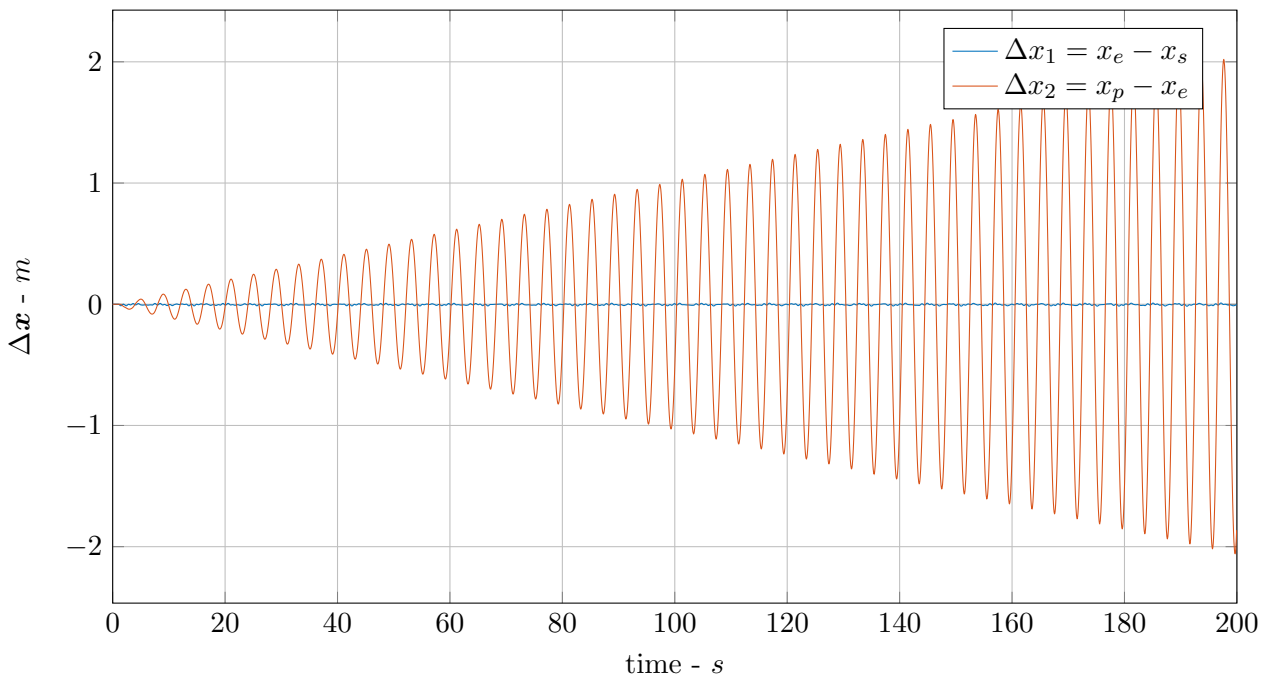


Figure 3.5: 1D simulation with different force frequencies.



(a) 1.0701 Hz



(b) 0.24915 Hz

Figure 3.6: 1D simulation with resonance response.

As shown in Figure 3.5, the end of the thrust profile is always critical for detachment in all of the selected frequencies: for this reason another approach was taken in account.

The idea was to detect the initial behaviour of the detachment (when the relative distance between chaser and Envisat is close to zero) and turn on the thrusters. This kind of system varies length of each step and the pause between each step.

A simulation of that was performed and the result are shown in Figure 3.7; the constant parameters were $k_1 = 60000 \text{ N/m}$, $d_1 = 1200 \text{ Ns/m}$, $k_2 = 800 \text{ N/m}$, $d_2 = 800 \text{ Ns/m}$. In both cases presented the thrust force is starting at $t = 1 \text{ s}$ with 450 N and in the case (a) is switched off after 3 s , in case (b) after 5 s .

The final phase is critical in both cases and also it is possible that the thruster is not capable to provide the force in the timing required and also in this case the detachment is induced.

3.4.3 Force Amplitude Modulation

In conclusion, the force cannot be switched to zero in one single step and the only solution is trying to reduce gradually the amplitude.

Even in this case some rules should be imposed to the thrust force profile to avoid detachment:

- the modulation should be at low frequency, to give the system the time to reach its steady state
- every step could be, at most, half the amplitude of the previous, because the value of the overshoot is related to the amplitude of the exciting force.

In Figure 3.8 there is an example of this kind of force profile and the response in terms of relative position between the chaser and Envisat. The data used for this analysis were the same of the previous ($k_1 = 60000 \text{ N/m}$, $d_1 = 1200 \text{ Ns/m}$, $k_2 = 800 \text{ N/m}$, $d_2 = 800 \text{ Ns/m}$) and the thrust force starts from 450 N and it reduces every 5 s .

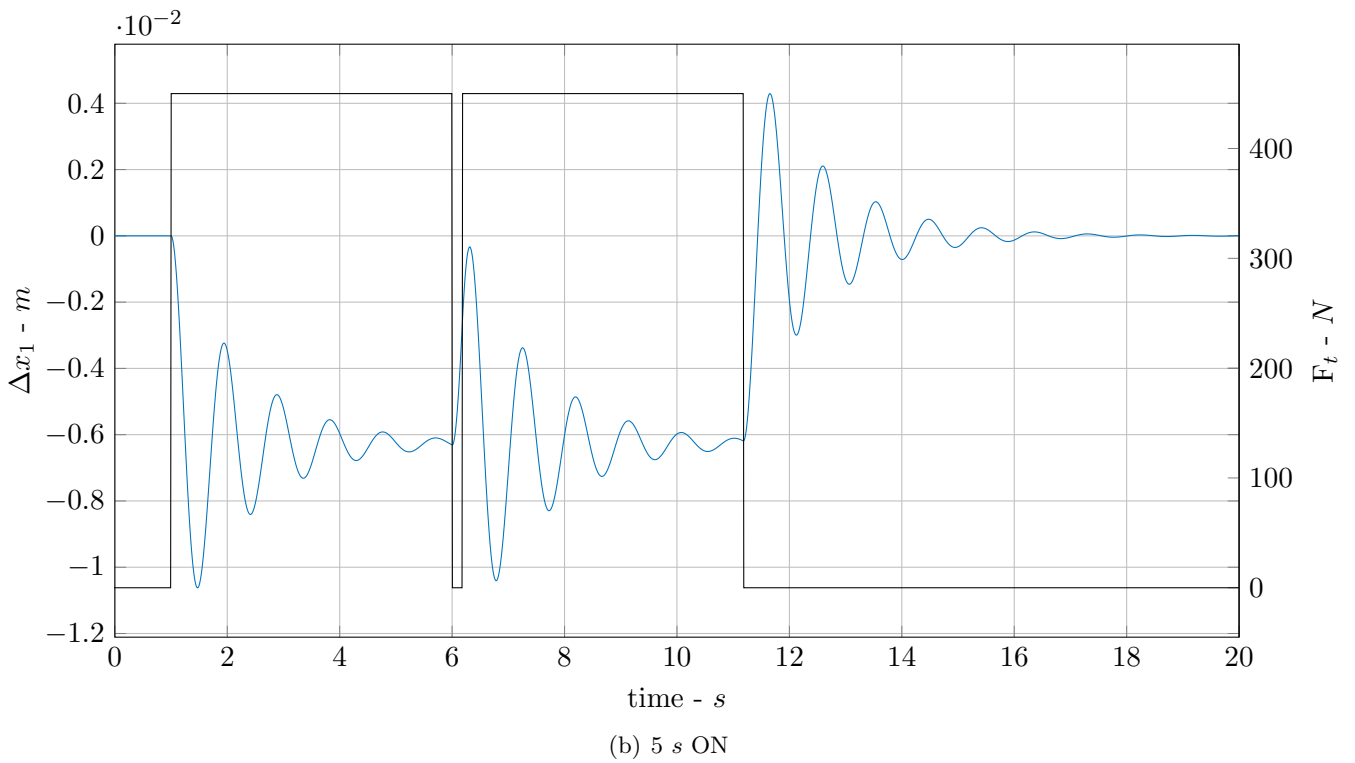
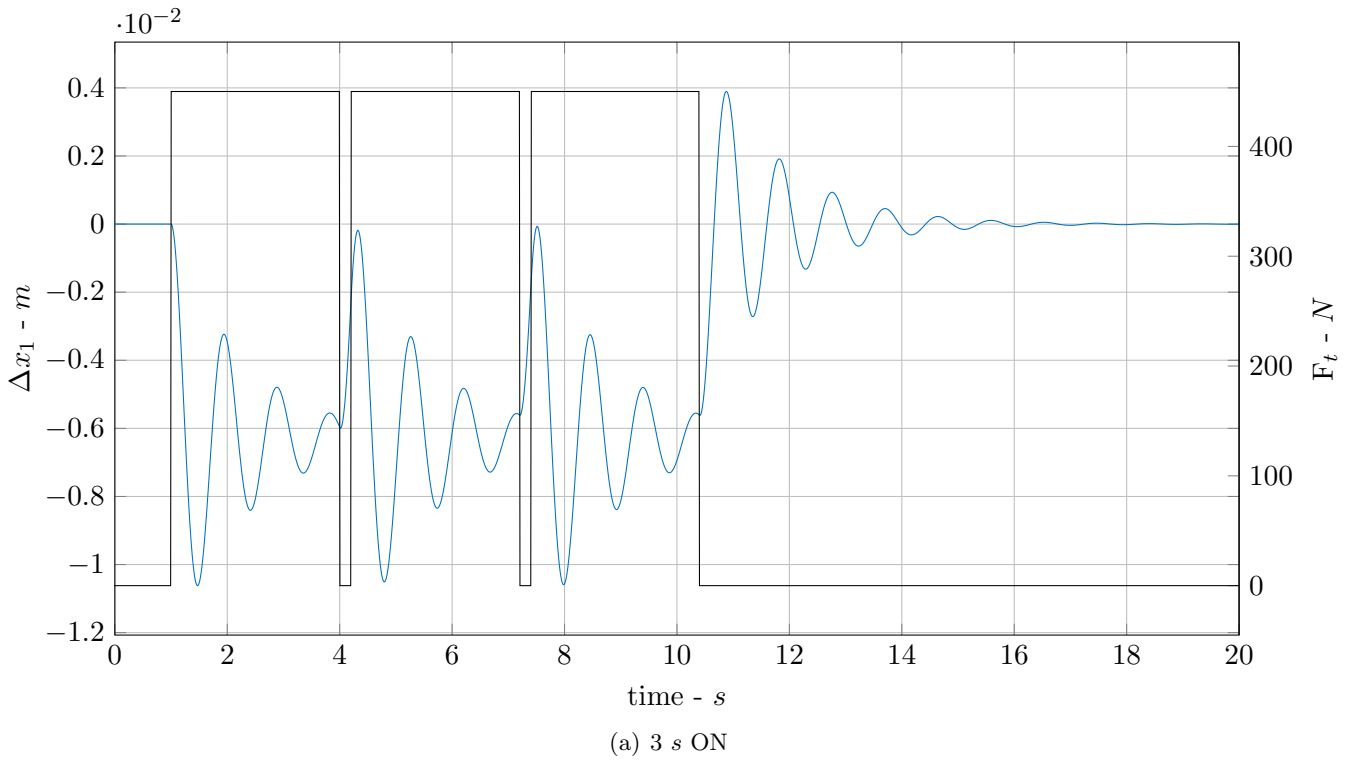


Figure 3.7: 1D simulation with triggered force profile.

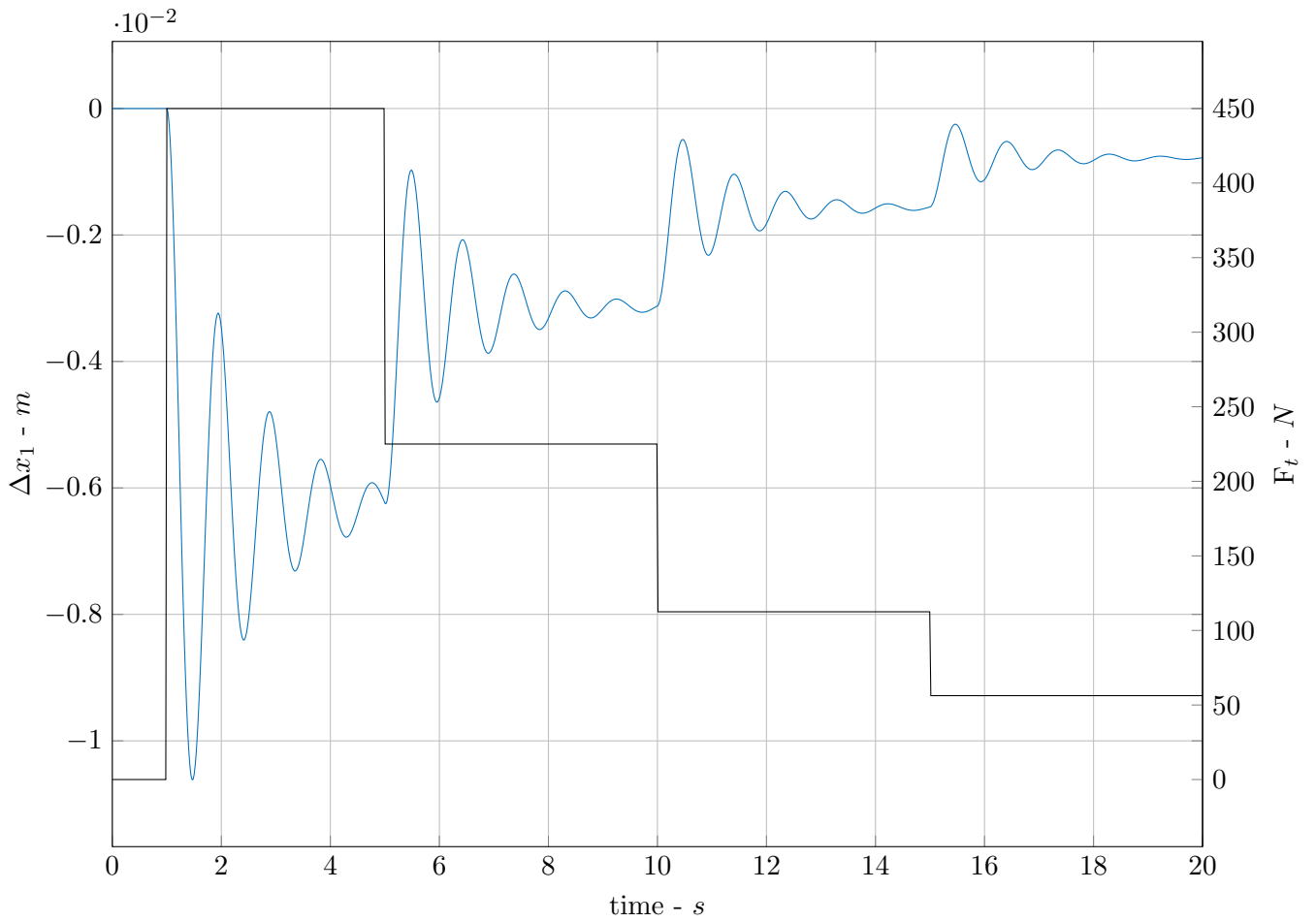


Figure 3.8: 1D simulation with amplitude modulation of force profile.

3.5 Torque on Robotic Arm

The knowledge of the joint torques applied to the robotic arm is of great interest, especially in the case of detachment.

To perform this analysis a simplified 2D model was set up: the displacement between the chaser and Envisat was considered the same as the displacement at the end effector of the manipulator.

Another assumption was that the manipulator has only two rigid links and two rotational joints in the same plane, as showed in Figure 3.9.

3.5.1 Model Assumptions

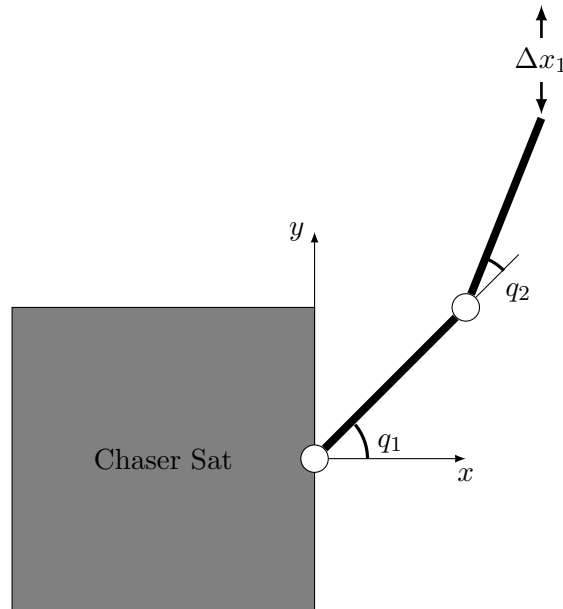


Figure 3.9: 2D Model representation.

The Δx_1 previously calculated (3.4) is applied only in y -direction and, referring to Figure 3.9, the unknowns are q_1 and q_2 . Assuming L_1 and L_2 as the lengths of the two links, the position of the end effector is:

$$\mathbf{x}_{ee} = \mathbf{T}(q_1) \begin{bmatrix} L_1 \\ 0 \end{bmatrix} + \mathbf{T}(q_1 + q_2) \begin{bmatrix} L_2 \\ 0 \end{bmatrix} \quad (3.16)$$

the matrix $\mathbf{T}(\cdot)$ is the rotation matrix:

$$\mathbf{T}(\cdot) = \begin{bmatrix} \cos(\cdot) & -\sin(\cdot) \\ \sin(\cdot) & \cos(\cdot) \end{bmatrix} \quad (3.17)$$

The value of the joint angle after the application of displacement can be obtained by solving the equations:

$$\begin{bmatrix} 0 \\ \Delta x_1 \end{bmatrix} = \mathbf{x}_{ee}(t) - \mathbf{x}_{ee}(t_0) \quad (3.18)$$

3.5.2 Results

This very simple case as results from the hypothesis that the robotic arm does not move and the internal joint torque is obtained by a given stiffness and the deflection around the constant joint position equilibrium. This simple flexible joint model can be used because the robotic arm is not actively moved.

The torque on joints depends on their stiffness; the parameter used were taken from the data sheet of real components (Harmonic Drive Systems) and the stiffness is the same for the two joints: $K_t = 5 \cdot 10^4 \text{ Nm/rad}$.

Multiplying this spring rate with the joint angle, it is possible to obtain the torque:

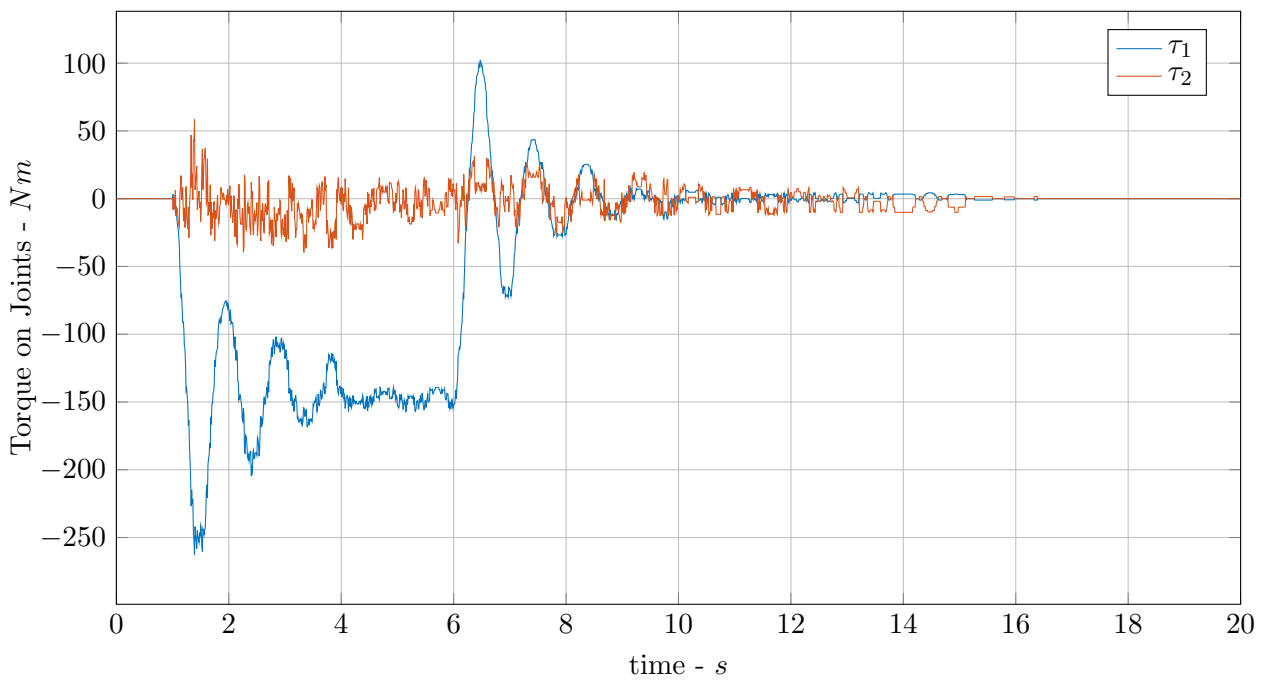
$$\tau_1 = K_t(q_1(t) - q_1(t_0)) \quad (3.19a)$$

$$\tau_2 = K_t(q_2(t) - q_2(t_0)) \quad (3.19b)$$

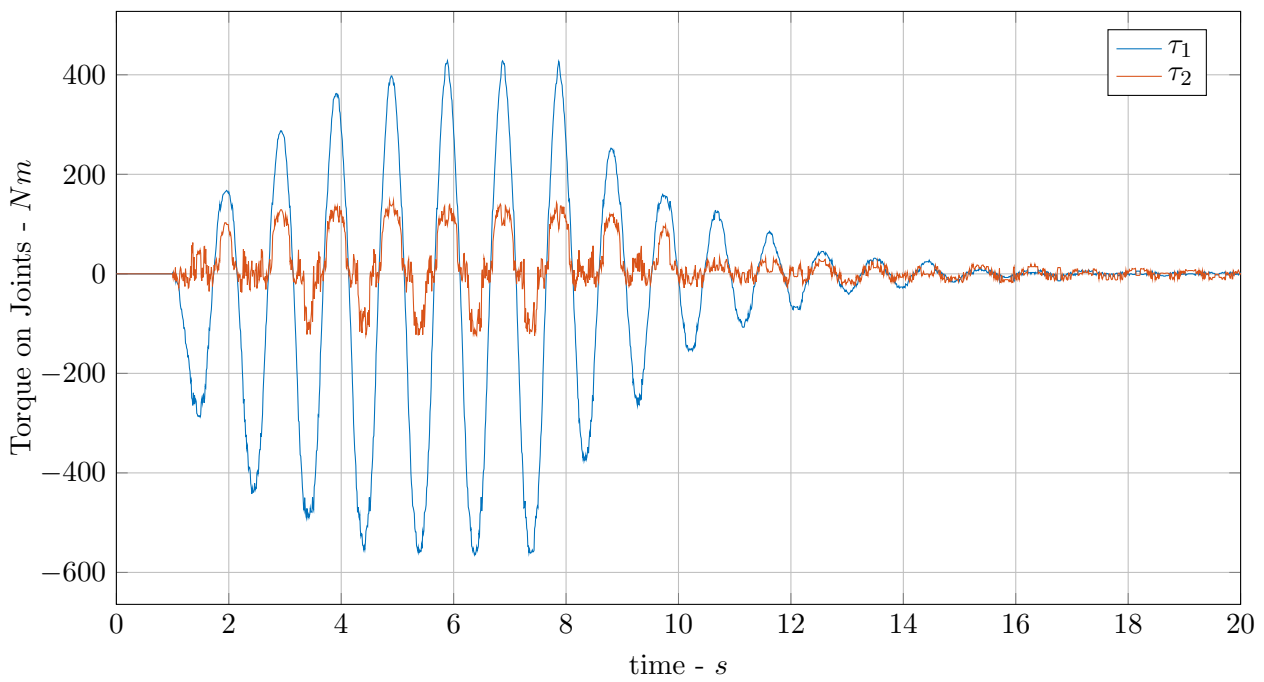
Two simulations were performed in order to analyse two different worst cases:

- (a) stiffness of connection $k_1 = 60000 \text{ N/m}$, Figure 3.3;
- (b) force at resonant frequency (1 Hz), Figure 3.5(c).

In Figure 3.10 the results of these simulations are shown.



(a)



(b)

Figure 3.10: Simulation on the torques produced by the detachment on the end effector.

Chapter 4

Three Dimensional Analysis

4.1 Problem Statements

This Chapter describes the analyses about the two most important manoeuvres: during the stabilisation and in the deorbiting scenario. To perform these simulations, a calculation of the complete forward dynamic of the multi-body system is necessary.

The simulations were performed in two different software environments: in Simulink, with the usage of SpaceDyn Library (explained in detail in Section 4.3), and in Simpack, a software especially developed for multi-body analysis.

4.2 Theoretical Background

The following section describes the mathematical theory of free-floating and free-flying robot dynamics. An initial global definition of the system is necessary, even if it will slightly change in the different scenarios.

As a space satellite, the model should take in account the movements of the base, so a free floating or free flying (if actively controlled by thruster or reaction wheels) system is considered.

In this Chapter all the multi-body structures considered are arranged in open branches (or equivalently, in kinematic tree), this means that it is not possible to trace a circuit from one link back to itself, without traversing any joint more than once. The closed loop chains are explained and analysed in the next Chapter.

The dynamic modelling represents the coupling between the motion of a robot and the forces that act on a robot. These forces are the forces and torques that are applied to the actuators of the robot as well as the external forces that result due to the contact of the robot with other objects.

There are two different approach for dynamic analysis:

forward dynamics, that is the calculation of the acceleration response of a given system to a given applied force,

inverse dynamics, that is the calculation of the force that must be applied to a given system in order to produce a given acceleration response.

This work was mainly concerned on the forward dynamics.

The general equation of motion of a free-flying robot describes the relationship between the forces acting on the system and the accelerations they produce: for this reason these equations are a relevant part of the dynamic analysis. The canonical form for the equation of motion of a free floating system is defined as:

$$\begin{bmatrix} \mathbf{H}_b & \mathbf{H}_{bm} \\ \mathbf{H}_{bm}^T & \mathbf{H}_m \end{bmatrix} \begin{bmatrix} \ddot{\mathbf{x}}_b \\ \ddot{\mathbf{q}} \end{bmatrix} + \begin{bmatrix} \mathbf{c}_b \\ \mathbf{c}_m \end{bmatrix} = \begin{bmatrix} \mathbf{F}_b \\ \boldsymbol{\tau}_m \end{bmatrix} + \begin{bmatrix} \mathbf{J}_b^T \\ \mathbf{J}_m^T \end{bmatrix} \mathbf{F}_{ee} \quad (4.1)$$

with the following definitions:

\mathbf{H}_b	$\in R^{6 \times 6}$: Inertia matrix of the base
\mathbf{H}_{bm}	$\in R^{6 \times N_q}$: Coupling inertia matrix
\mathbf{H}_m	$\in R^{N_q \times N_q}$: Inertia matrix of manipulator
\mathbf{x}_b	$\in R^{6 \times 1}$: Position and rotation of the base
\mathbf{q}	$\in R^{N_q \times 1}$: Joint rotations
\mathbf{C}_b	$\in R^{6 \times 1}$: Non linear terms (base)
\mathbf{C}_m	$\in R^{N_q \times 1}$: Non linear terms (manipulator)
\mathbf{F}_b	$\in R^{6 \times 1}$: Force and torques on the base
$\boldsymbol{\tau}$	$\in R^{N_q \times 1}$: Joint torques
\mathbf{J}_b	$\in R^{6 \times 6}$: Jacobian matrix for base variables
\mathbf{J}_m	$\in R^{6 \times N_q}$: Jacobian matrix for joint variables
\mathbf{F}_{ee}	$\in R^{6 \times 1}$: External force and moment on the end effector

This equation should be solved for the accelerations of the base and the joints, then an integration should be performed. This is a crucial part of the calculations, because with different integrations methods, one could obtain different results, both in terms of accuracy and in computational time.

4.3 SpaceDyn Library

The SpaceDyn is a Matlab based library for the kinematic and dynamic analysis and simulation of articulated multi-body systems with a moving base. Examples of such systems include a satellite with mechanical appendages, a free flying space robot and a robotic system with structural flexibility, all of which makes motions in the environment with or without gravity.

The SpaceDyn library was developed by Prof. Joshida (Japan) and extended at the DLR since 2007. The integration in the Simulink environment is performed by the use of Matlab S-functions (system-functions): these are a computer language description of a Simulink block written in Matlab, C, C++, or Fortran.

The following paragraphs provide a quick summary on the mathematical modelling of the multi-body system and the computational procedures used [20].

Model of the System. Assuming that the system is composed of $n + 1$ bodies, connected by n joints. Let the body 0 be a reference body (also called base). Multiple branches can attach on any single body, as far as the system keeps a topological tree configuration. There must be a single joint between two bodies. A terminal point or a point of interest, such as manipulator hand, is termed as end effector. Each body, except body 0, can have one end effector.

Force and Torque Inputs. The inputs of the system could be forces or torques applied on the centroid of the reference body as \mathbf{F}_b , or on each end effector, or on each joint as $\boldsymbol{\tau}$. Specification of these force/torque are open, for examples could be control inputs or any physical constraints written in the form of forces and torques. The computation as results of the forward solution of dynamics with numerical integration are the acceleration, velocity and position of the centroid of the reference body, each joint and each endpoint.

Attitude Representation. For the representation of attitude or orientation, the direction cosine matrices are used (3×3), coded with a symbol \mathbf{C} . For example, \mathbf{C}_O is the direction cosines to represent the attitude of the body 0. The advantages of direction cosine are singularity free, easy translation to Roll-Pitch-Yaw angles, Euler angles, or quaternions and a mathematically clear relationship with angular velocity.

Connection Graph Representation. In order to mathematically describe the interconnection of the bodies, the method used in the mathematical graph theory was used with the simplification provided by additional rules on the assignment of link and joint indices. In plain sentences the rules can be described as: the index number of a link located in between the base and link j , must be bigger than 0 and lower than j , and the joint that connects links i and j ($i < j$) is numbered by j . Figure 4.1 depicts an example of a system with multiple branches numbered with this manner.

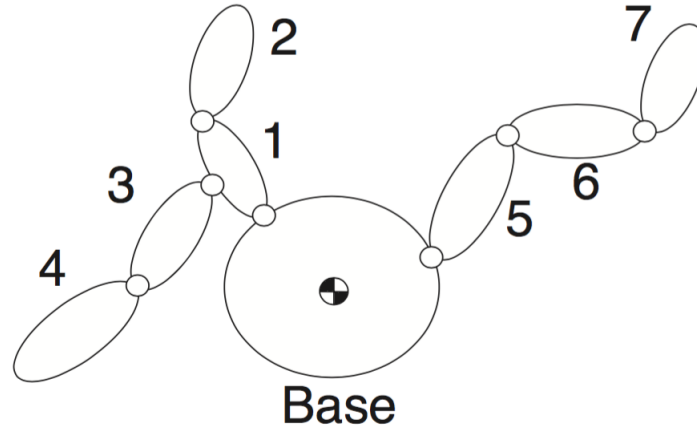


Figure 4.1: Sample system with the enumeration of bodies.

Coordinate System. The inertial reference coordinate frame is stationary or moving with constant velocity in the inertial space. It is not physically precise, but in practice the orbital fixed frame is considered as the inertial frame. The other moving coordinate frames are fixed on each link of the articulated bodies and on the base. The orientation of principle axes is arbitrary, but it is recommended to orient these axes being parallel to the principle axes of the body inertia. For the assignment of moving coordinate frames on other links, one of the way commonly used in the field of manipulator kinematics is the Denavit-Hartenberg convention. This is known as advantageous in unique assignment of coordinate systems with minimum link parameters. However this convention locates sometimes the coordinate origin away from the location of the actual joint and for the dynamic analysis this is not reasonable. Therefore another set of rules was used:

1. if joint i is revolute
 - locate the origin of the coordinate frame on joint i and fixed to link i ,
 - set its z -axis to coincide with the joint rotation axis,
 - orient its x -axis toward joint $i + 1$;
2. if joint i is prismatic
 - locate the origin of the coordinate frame on the point when joint i has zero displacement and fixed to link $i - 1$,
 - set its z -axis to coincide with the joint displacement axis with the positive direction,
 - orient its x -axis toward joint $i + 1$.

Direction Cosine and Coordinate Transformation Matrices. The direction cosine matrices \mathbf{C}_i are commonly used to represent the attitude or orientation of a body in the field of aerospace engineering. On the other hand, the coordinate transformation matrices with the notation of ${}^I\mathbf{A}_i$, are commonly used in the field of robotics. These two are the same thing, but in a transposed way:

$$\mathbf{C}_i = {}^i\mathbf{A}_I$$

Since we define the link coordinate system as above, the three axis rotations are needed:

$$\mathbf{C}_i = \mathbf{C}(\gamma_i) \mathbf{C}(\beta_i) \mathbf{C}(\alpha_i)$$

where α_i , β_i and γ_i are Roll, Pitch and Yaw angles respectively of the joint i . The direction cosines are redundant parameters to represent attitude, but the advantage is that the relationship between attitude and angular velocity can be expressed by a simple equation, such that:

$$\dot{\mathbf{C}}_i = -\boldsymbol{\omega}_i \times \mathbf{C}_i$$

This relationship is used in the routines of singularity-free integration from angular velocity to attitude.

4.4 Simpack Environment

Simpack is a commercial multi-body simulation software tool used for mechanical system design. It is able to simulate the dynamics of different systems for example in aerospace, automotive and rail applications.

Simpack is used at DLR for the simulation and demonstration of robotic systems both with or without the use of flexible bodies. In this work the main use of this software was for testing and validation of the results obtained from the Simulink analyses.

The workflow to perform a Simpack multi-body simulation can be divided into following steps:

1. **Pre-Processing**, is the environment in which every body that compose the system is defined within its physical and graphical proprieties;
2. **Solver**, it the core of the calculation, when the integration and the measurements are performed;
3. **Post-Processing**, is different environment, built in especially for the analysis of the results of simulations.

Detailed informations about the Solver can be found in Appendix A; the Post-Processing of Simpack was not used for this work.

4.5 Deorbiting Scenarios

The different scenarios analysed are reported in the following Sections, with a detailed explanation of the simulation results.

4.5.1 Clamping on Top

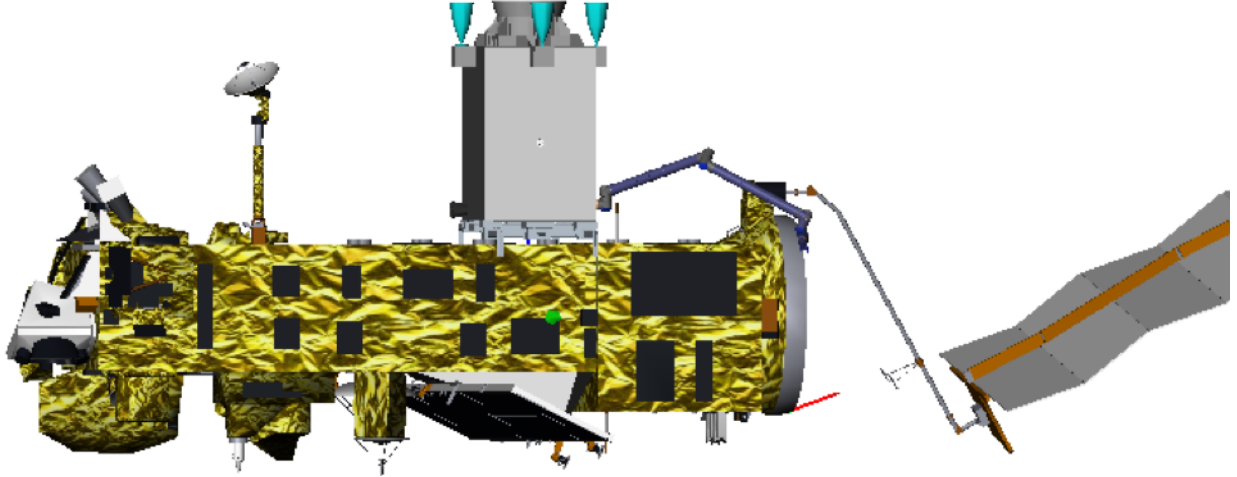


Figure 4.2: Representation of the clamping on top deorbiting configuration.

For this analysis two main rigid bodies were considered, one for Envisat with its solar panel and the other for the Servicer Module. Following, a detailed description of each model is provided.

In Figure 4.3 the reference frames of each body and their orientation with respect to the inertial reference frame are represented. As it is shown, the main hypothesis of the model is that the thrust force is directed to the centre of mass of the system and of Envisat, in order to perform a correct deorbiting manoeuvre.

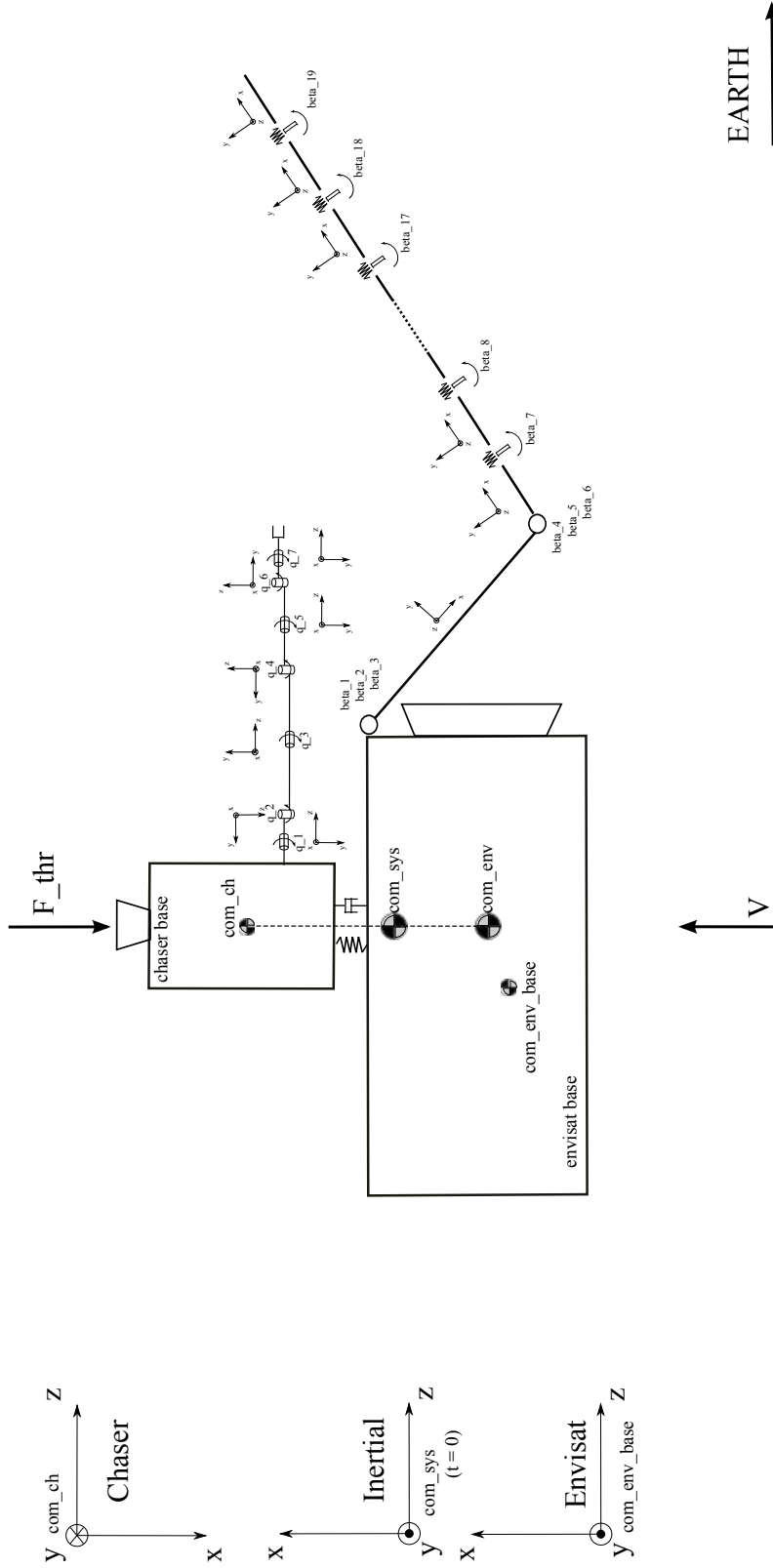


Figure 4.3: 2D Sketch of the Phase A configuration with reference frames.

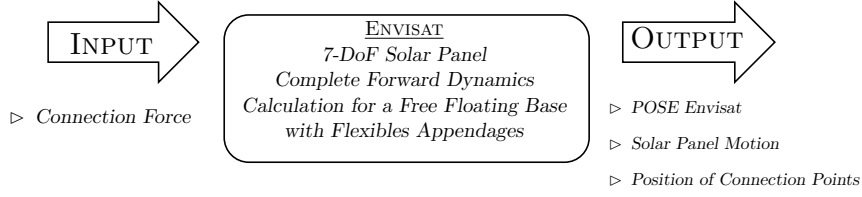


Figure 4.4: Scheme of the system implemented for the target satellite.

The Envisat's model has 7-DoF: the solar panel was divided into six sections and one additional DoF was for the axial boom that connects the panel to the main body. The scheme of input/output of that model is represented in Figure 4.4. The panel was treated as a flexible appendage, for this reason each joint acceleration must be calculated with the equation of motion, Eq. (4.1). Simplifying that by the force acting on the end effector, one could obtain:

$$\begin{bmatrix} \mathbf{H}_b & \mathbf{H}_{bm} \\ \mathbf{H}_{bm}^T & \mathbf{H}_m \end{bmatrix} \begin{bmatrix} \ddot{\mathbf{x}}_b \\ \ddot{\mathbf{q}} \end{bmatrix} + \begin{bmatrix} \mathbf{c}_b \\ \mathbf{c}_m \end{bmatrix} = \begin{bmatrix} \mathbf{F}_b \\ \boldsymbol{\tau}_m \end{bmatrix} \quad (4.2)$$

However the flexibility of the panel should be taken in account: the differential deflection angle and velocity (with respect to the initial configuration) multiplied by the stiffness and damping coefficients are the torques acting on the joints $\boldsymbol{\tau}_m$.

$$\boldsymbol{\tau}_m = -K_{pan}\Delta\mathbf{q} - D_{pan}\Delta\dot{\mathbf{q}} \quad (4.3)$$

The stiffness parameters of the panel was made taking into account the real frequency of the structure and the damping was chosen to be the 10%; for simplicity all the parameters was set as the same value, so that $K_{pan} = 10000 \text{ Nm/rad}$ and $D_{pan} = 1000 \text{ Nms/rad}$.

The Table 4.1 is a list of proprieties of Envisat base, boom and solar panel; for the latter was reported one single section.

The Servicer satellite has the 7-DoF manipulator fully controlled, so the angular position, velocity and acceleration of each link are known at each time. For this reason the equation to solve is only the first row of the equation of motion Eq. (4.1), and considering that there is no force acting on the end effector, it is possible to obtain:

$$\mathbf{H}_b\ddot{\mathbf{x}}_b + \mathbf{H}_{bm}\ddot{\mathbf{q}} + \mathbf{c}_b = \mathbf{F}_b \quad (4.4)$$

The input of the block is the thruster force and the connection force (Figure 4.5).

In the Table 4.2 are listed all the data of the Chaser and manipulator.

Base					
<i>Mass [kg]</i>	7490			<i>Dimension [m]</i>	10 x 2.75 x 2.075
<i>Inertia Matrix [kg m²]</i>	11113.1	397.1	848	<i>Orientation [deg]</i>	<i>r</i> 0
	397.1	117837.3	344.2	<i>p</i>	0
	848	344.2	126686.9	<i>y</i>	0
Boom (Rotational Joint)					
<i>Mass [kg]</i>	10.8			<i>Dimension [m]</i>	3
<i>Inertia Matrix [kg m²]</i>	0.007	0	0	<i>Orientation [deg]</i>	<i>r</i> -90
	0	8.1035	0	<i>p</i>	0
	0	0	8.1035	<i>y</i>	-155
Solar Panel Section (Rotational Joint)					
<i>Mass [kg]</i>	23.3714			<i>Dimension [m]</i>	1.3333 x 4.97
<i>Inertia Matrix [kg m²]</i>	54.5333	0	0	<i>Orientation [deg]</i>	<i>r</i> 0
	0	50.6518	0	<i>p</i>	0
	0	0	2.54383	<i>y</i>	95

Table 4.1: List of parameters of Envisat used for the simulation.

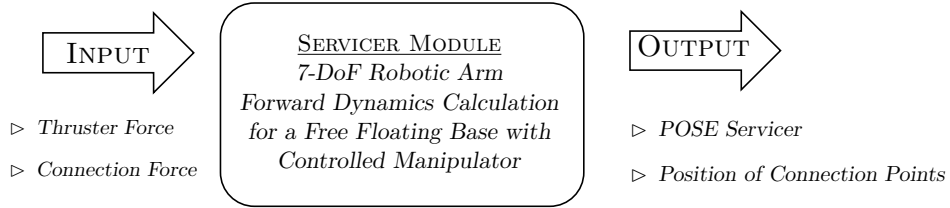


Figure 4.5: Scheme of the system implemented for the servicer satellite.

The connection between the Chaser Satellite and Envisat is a rigid contact surface and it is attached on the Chaser. The force acting on Envisat base depends on the relative distance between Envisat and the Chaser. The same force with opposite sign is acting on the Chaser.

$$\mathbf{F}_{conn} = k\Delta\mathbf{R} + d\Delta\mathbf{V} \quad (4.5)$$

with:

$$\Delta\mathbf{R} = [\mathbf{x}_{conn}]_{env} - [\mathbf{x}_{conn}]_{ch} \quad (4.6a)$$

$$\Delta\mathbf{V} = [\dot{\mathbf{x}}_{conn}]_{env} - [\dot{\mathbf{x}}_{conn}]_{ch} \quad (4.6b)$$

Base						
<i>Mass [kg]</i>	850			<i>Dimension [m]</i>	2.38 x 1.5 x 1.695	
<i>Inertia Matrix [kg m²]</i>	362	0	0	<i>Orientation [deg]</i>	<i>r</i>	0
	0	604	0		<i>p</i>	0
	0	0	560		<i>y</i>	0
Link 1 (Rotational Joint)						
<i>Mass [kg]</i>	0.0001			<i>Dimension [m]</i>	0.256	
<i>Inertia Matrix [kg m²]</i>	0.0001	0	0	<i>Orientation [deg]</i>	<i>r</i>	-90
	0	0.0001	0		<i>p</i>	0
	0	0	0.0001		<i>y</i>	0
Link 2 (Rotational Joint)						
<i>Mass [kg]</i>	0.0001			<i>Dimension [m]</i>	0.168	
<i>Inertia Matrix [kg m²]</i>	0.0001	0	0	<i>Orientation [deg]</i>	<i>r</i>	90
	0	0.0001	0		<i>p</i>	0
	0	0	0.0001		<i>y</i>	180
Link 3 (Rotational Joint)						
<i>Mass [kg]</i>	0.0001			<i>Dimension [m]</i>	1.450	
<i>Inertia Matrix [kg m²]</i>	0.0001	0	0	<i>Orientation [deg]</i>	<i>r</i>	-90
	0	0.0001	0		<i>p</i>	0
	0	0	0.0001		<i>y</i>	180
Link 4 (Rotational Joint)						
<i>Mass [kg]</i>	0.0001			<i>Dimension [m]</i>	0.168	
<i>Inertia Matrix [kg m²]</i>	0.0001	0	0	<i>Orientation [deg]</i>	<i>r</i>	90
	0	0.0001	0		<i>p</i>	0
	0	0	0.0001		<i>y</i>	0
Link 5 (Rotational Joint)						
<i>Mass [kg]</i>	0.0001			<i>Dimension [m]</i>	1.050	
<i>Inertia Matrix [kg m²]</i>	0.0001	0	0	<i>Orientation [deg]</i>	<i>r</i>	-90
	0	0.0001	0		<i>p</i>	0
	0	0	0.0001		<i>y</i>	180
Link 6 (Rotational Joint)						
<i>Mass [kg]</i>	0.0001			<i>Dimension [m]</i>	0.168	
<i>Inertia Matrix [kg m²]</i>	0.0001	0	0	<i>Orientation [deg]</i>	<i>r</i>	90
	0	0.0001	0		<i>p</i>	0
	0	0	0.0001		<i>y</i>	0
Link 7 (Rotational Joint)						
<i>Mass [kg]</i>	0.0001			<i>Dimension [m]</i>	0.371	
<i>Inertia Matrix [kg m²]</i>	0.0001	0	0	<i>Orientation [deg]</i>	<i>r</i>	-90
	0	0.0001	0		<i>p</i>	0
	0	0	0.0001		<i>y</i>	0

Table 4.2: List of parameters of the Chaser used for the simulation.

The position of the connection point and its velocity are evaluated from the positions of the CoM of the bases and their orientations.

The two parameters selected for the contact force evaluation are: $k = 60000 \text{ N/m}$ and $d = 120 \text{ Ns/m}$.

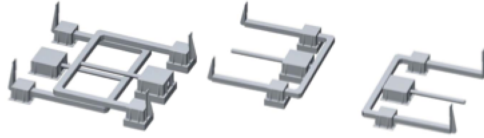


Figure 4.6: Clamping in four point mechanism concept, opened and closed.

For this simulation a thrust force of 450 N for 5 s was applied, starting from 1 s . This force is given in the reference frame of the chaser (Figure 4.3) and it must be reported in the inertial base (using the orientation matrix of the chaser).

The results of this simulation are reported in the following pages.

Regarding the position of the CoG of the system, shown in Figure 4.7, it is possible to observe a small deviation in the directions where the force is not directed, this is given by the dynamics of the flexible system. A similar oscillation behaviour is visible in the components of velocity shown in Figure 4.8, both for the Chaser and for the target satellite.

The connection force plotted in Figure 4.9 is a really useful result for the construction of the clamping mechanism and for the definition of requirements about it.

The last result, for this analysis, is the behaviour of the huge flexible panel of Envisat: in Figure 4.10 the angular rotations of each section are shown.

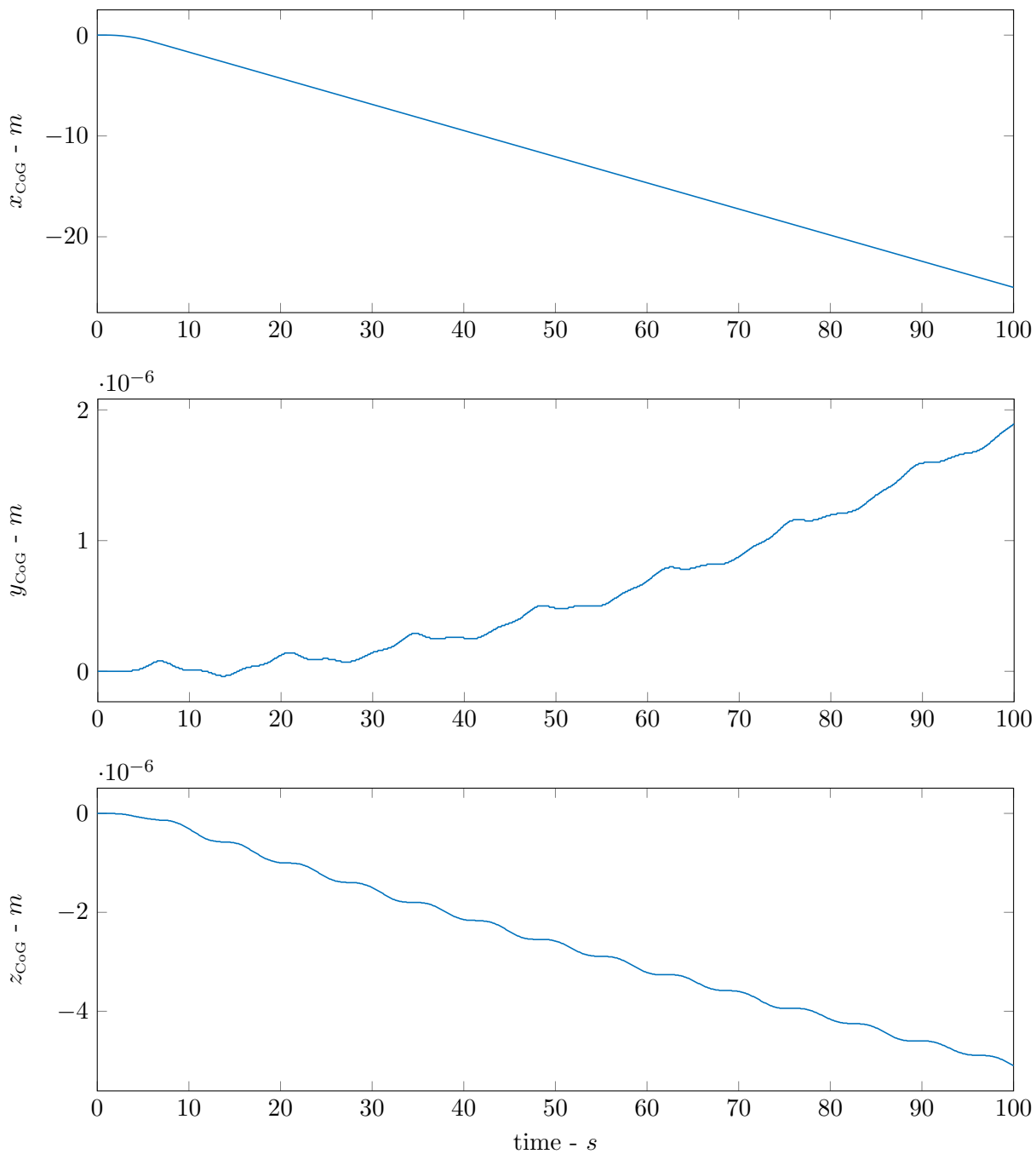
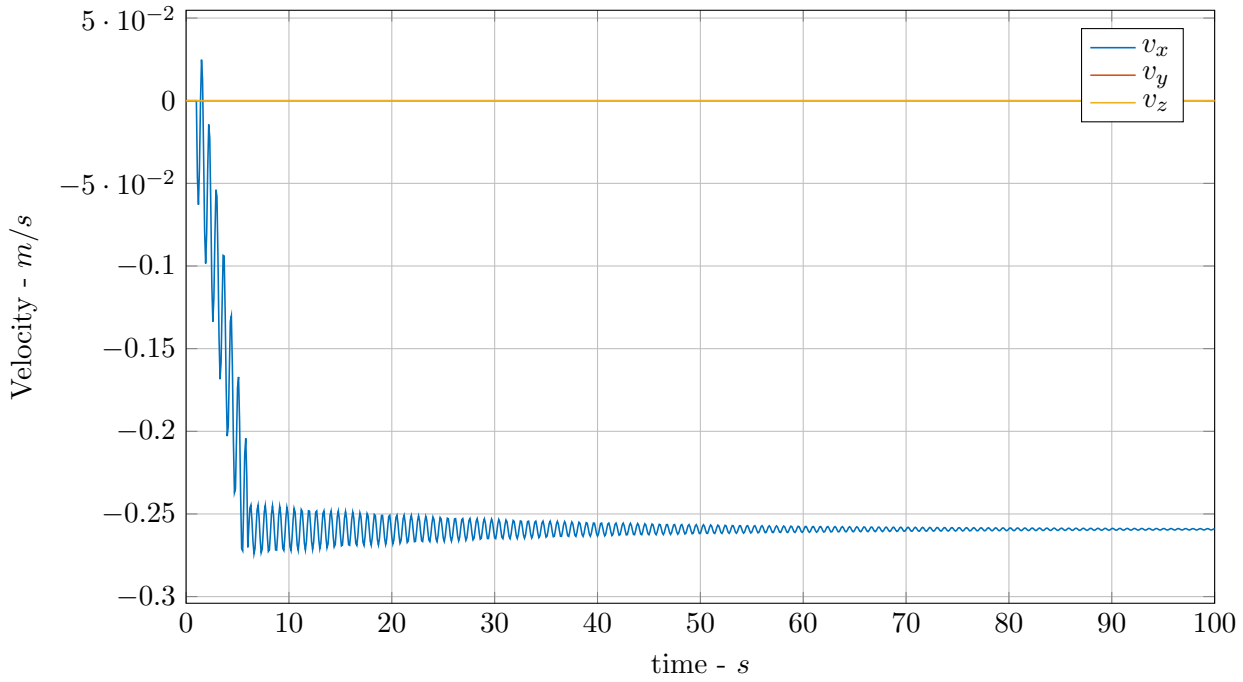
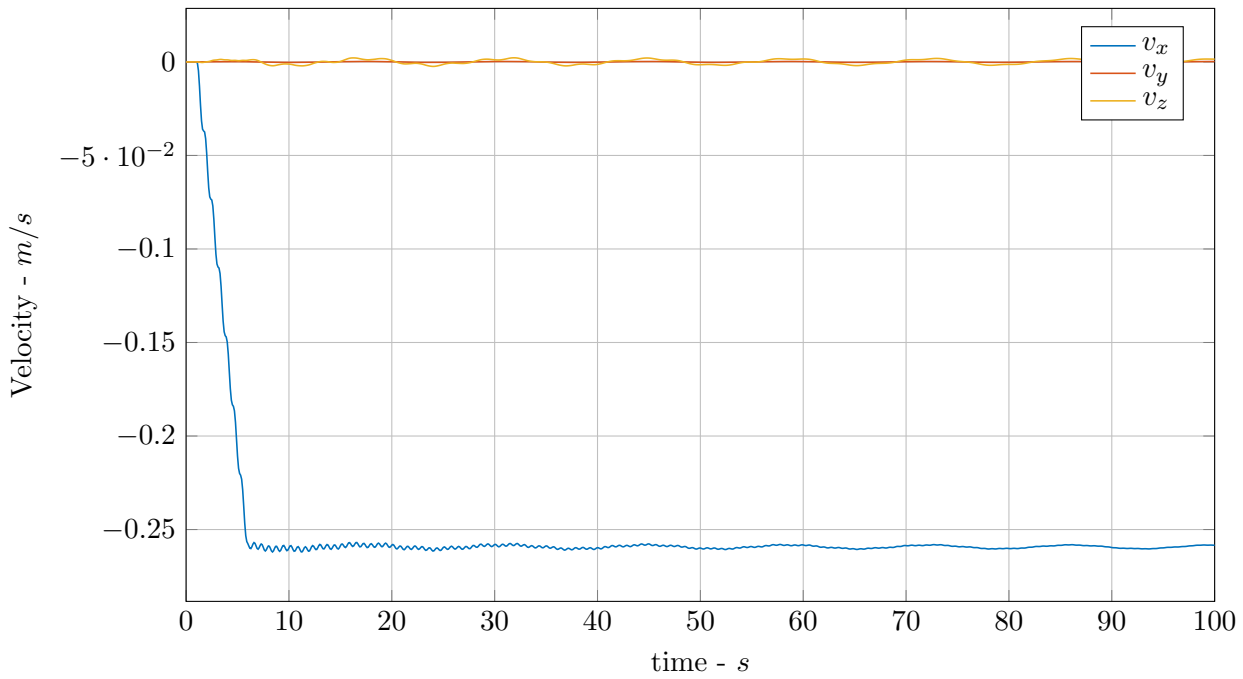


Figure 4.7: Position of the centre of gravity of the entire system during the simulation.



(a) Chaser



(b) Envisat

Figure 4.8: Velocity of the main bodies of the system.

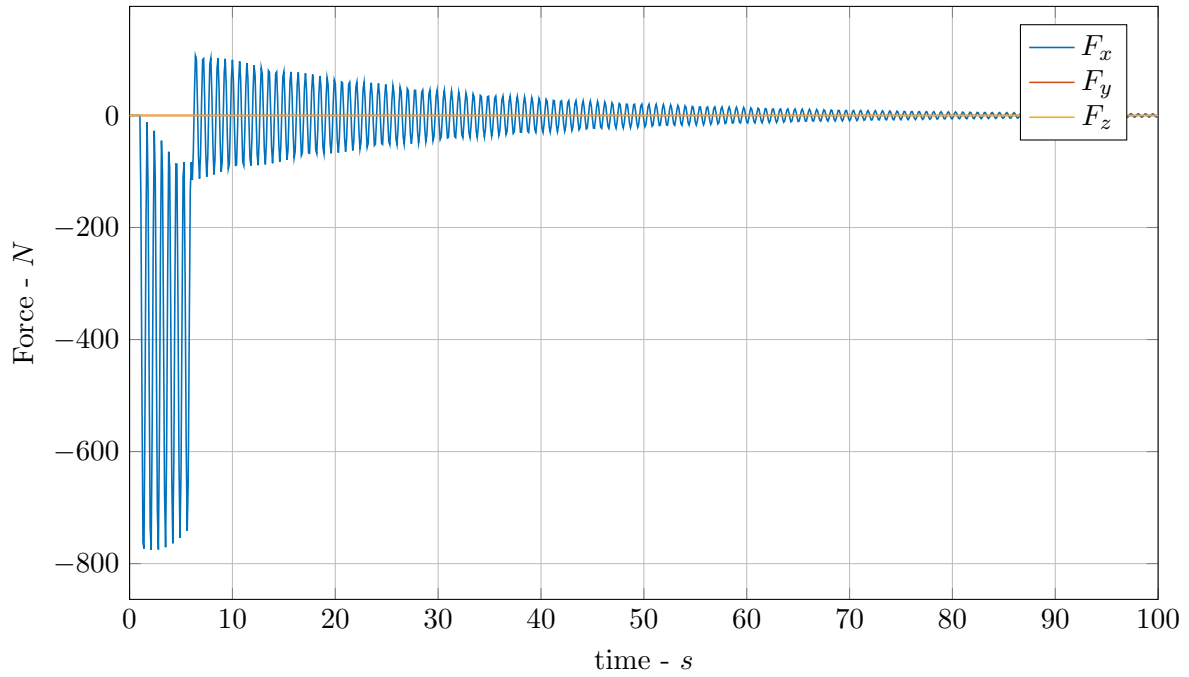


Figure 4.9: Connection force acting in the clamping mechanism (sum).

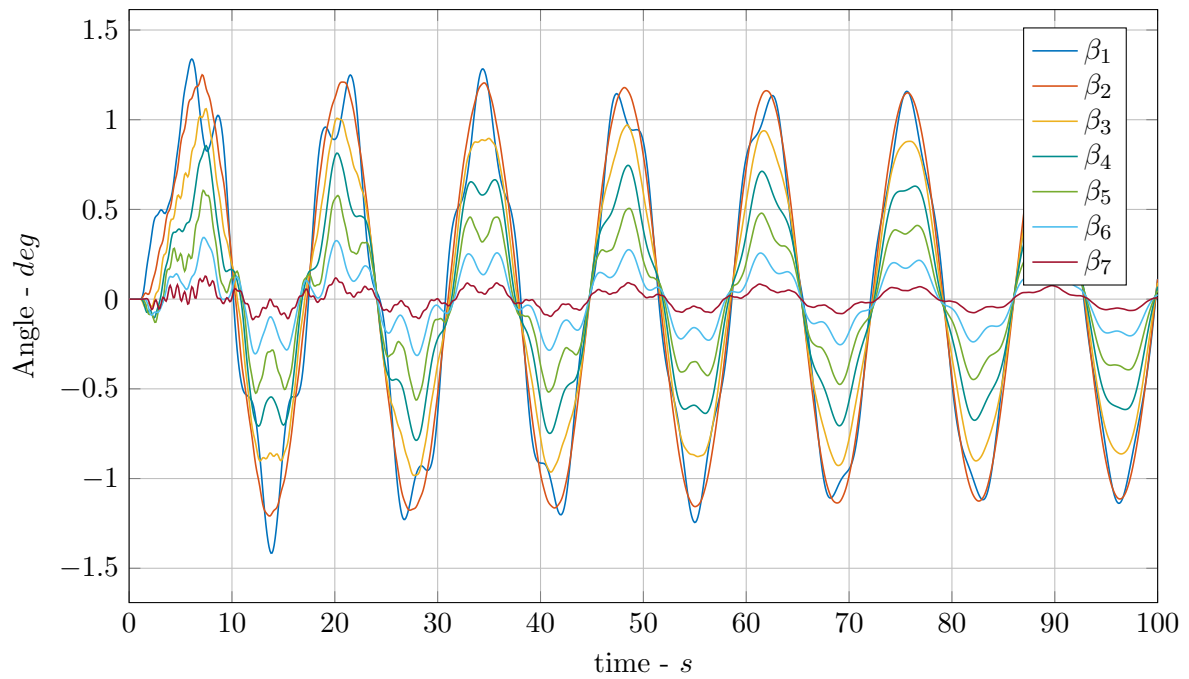


Figure 4.10: Rotation of the section of Envisat's solar panel.

4.5.2 Clamping on Payload Adapter

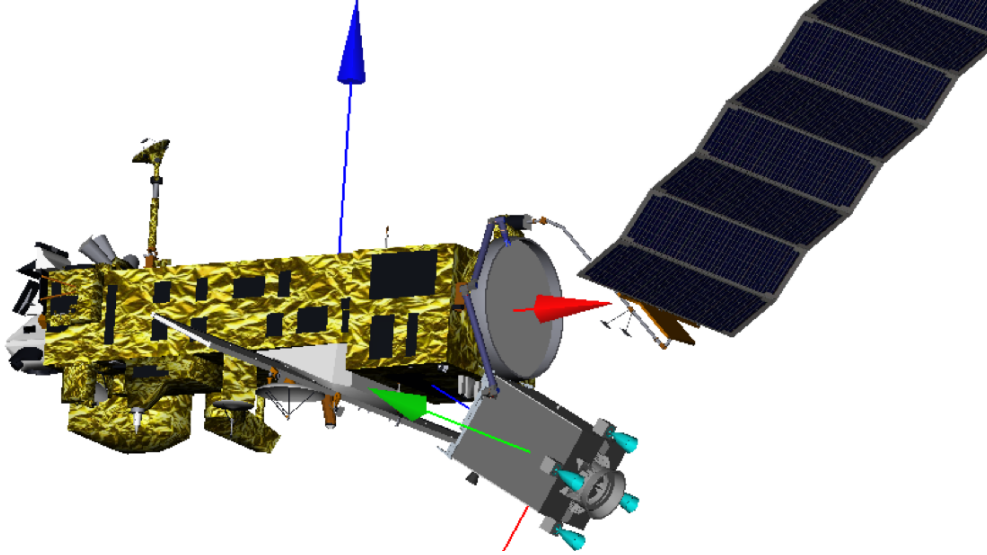


Figure 4.11: Representation of the clamping on payload adapter deorbiting configuration.

The configuration in Figure 4.11 is the latest proposed, in B1 Phase of the project; it presents some differences with respect to the previous simulation done, the main are:

- the Servicer Module is tilted of 60° with respect to the Envisat base;
- the connection is not a clamping with four connection points, but it is made up by a single clamp attached to the payload adapter of Envisat;
- the thrust force is 800 N instead of 450 N and it is directed always along the CoM of the system, thanks to the configuration of the connection.

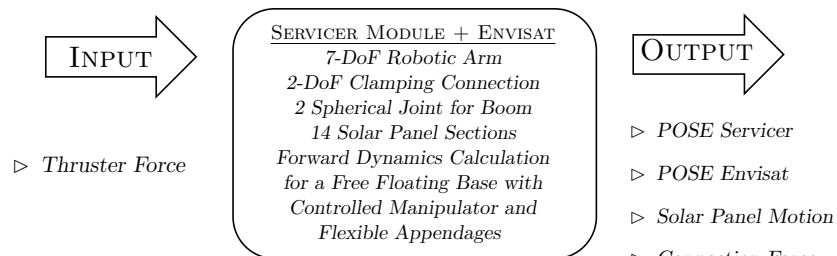


Figure 4.12: Scheme of the system implemented.

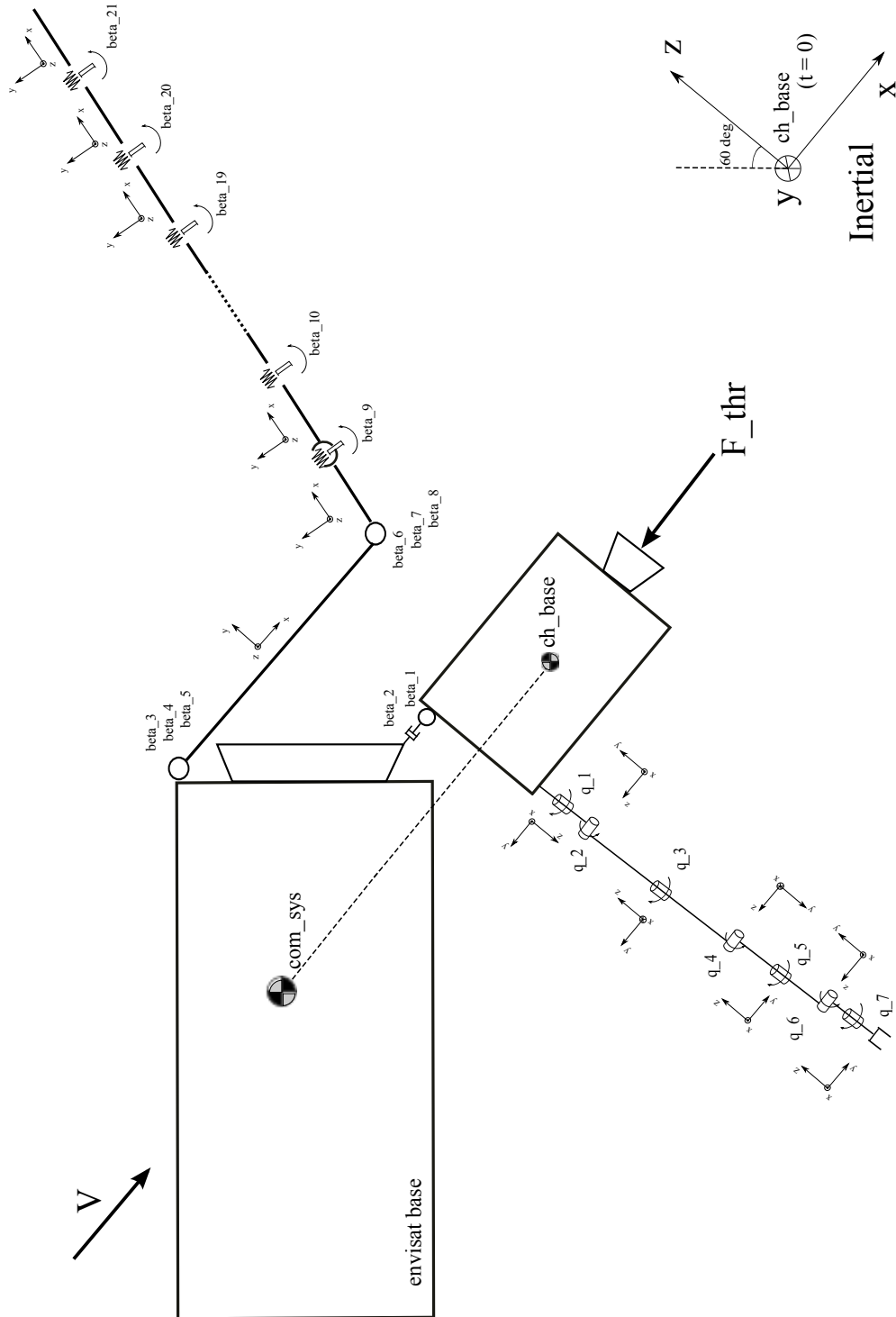


Figure 4.13: 2D Sketch of the Phase B configuration with reference frames.

For the previous analysis two different model parts were created, one for the Chaser and one for Envisat; the connection was an input forces of both models. With this new analysis only one model was created: as shown in Figure 4.12, this model include the 2-DoF connection, instead of calculating it externally.

In that case there are 28 degrees of freedom plus the 6-DoF of the floating base, as shown in Figure 4.13:

- 7-DoF controlled manipulator of the Chaser;
- 2-DoF connection to Envisat's payload adapter (the first rotational, the second translational);
- 6-DoF as two spherical joints that connects Envisat to the boom and the latter to the solar panel sections;
- 13-DoF as the rotational joints of the solar panel sections.

The manipulator of the Servicer module is active, but Envisat and its solar panel are considered as flexible appendages, for this reason the equation of motion Eq. (4.1) should be divided in order to consider the active variables (\mathbf{q}) and the flexible passive ones ($\boldsymbol{\beta}$). The re-written equation of motion is:

$$\begin{bmatrix} \mathbf{H}_b & \mathbf{H}_{bm} & \mathbf{H}_{b\beta} \\ \mathbf{H}_{bm}^T & \mathbf{H}_m & \mathbf{H}_{m\beta} \\ \mathbf{H}_{b\beta}^T & \mathbf{H}_{m\beta}^T & \mathbf{H}_\beta \end{bmatrix} \begin{bmatrix} \ddot{\mathbf{x}}_b \\ \ddot{\mathbf{q}} \\ \ddot{\boldsymbol{\beta}} \end{bmatrix} + \begin{bmatrix} \mathbf{c}_b \\ \mathbf{c}_m \\ \mathbf{c}_\beta \end{bmatrix} = \begin{bmatrix} \mathbf{F}_b \\ \boldsymbol{\tau}_m \\ -\mathbf{K}_{pan}\boldsymbol{\beta} - \mathbf{D}_{pan}\dot{\boldsymbol{\beta}} \end{bmatrix} + \begin{bmatrix} \mathbf{J}_b^T \\ \mathbf{J}_m^T \\ \mathbf{J}_\beta^T \end{bmatrix} \mathbf{F}_{ee} \quad (4.7)$$

with the following definitions:

$$\begin{array}{lll} \mathbf{H}_{b\beta} & \in & R^{6 \times N_\beta} : \text{Coupling inertia matrix} \\ \mathbf{H}_{m\beta} & \in & R^{N_q \times N_\beta} : \text{Coupling inertia matrix} \\ \mathbf{H}_\beta & \in & R^{N_\beta \times N_\beta} : \text{Inertia matrix for the flex append} \\ \mathbf{q} & \in & R^{N_q \times 1} : \text{Manipulator Joints} \\ \boldsymbol{\beta} & \in & R^{N_\beta \times 1} : \text{Flex Joints} \\ \mathbf{C}_\beta & \in & R^{N_q \times 1} : \text{Non linear terms (flex append)} \\ \mathbf{K}_{pan} & \in & R^{N_\beta \times 1} : \text{Stiffness param of flex joints} \\ \mathbf{D}_{pan} & \in & R^{N_\beta \times 1} : \text{Damping param of flex joints} \end{array}$$

The only unknown of the system of equation are the flexible states and the base motion ($\boldsymbol{\beta}$ and \mathbf{x}_b). In Table 4.3 all the data of the model used for the analysis are listed.

The connection between Envisat and the Servicer module has 2-DoF representing:

1. the rotational DoF, for the correct orientation with respect to the CoG of the entire system;

Base						
<i>Mass [kg]</i>	1535			<i>Dimension [m]</i>	2.36 × 2.75 × 2.075	
<i>Inertia Matrix [kg m²]</i>	1263.2	0	0	<i>Orientation [deg]</i>	<i>r</i>	0
	0	1679.8	0		<i>p</i>	0
	0	0	1518.1		<i>y</i>	0
Rotational Joint 1 - Manipulator						
<i>Mass [kg]</i>	3.2405			<i>Dimension [m]</i>	0.256	
<i>Inertia Matrix [kg m²]</i>	0.02288	0	0	<i>Orientation [deg]</i>	<i>r</i>	-90
	0	0.01037	0		<i>p</i>	0
	0	0	0.02288		<i>y</i>	90
Rotational Joint 2 - Manipulator						
<i>Mass [kg]</i>	2.1266			<i>Dimension [m]</i>	0.168	
<i>Inertia Matrix [kg m²]</i>	0.0084	0	0	<i>Orientation [deg]</i>	<i>r</i>	-90
	0	0.0068	0		<i>p</i>	0
	0	0	0.0084		<i>y</i>	0
Rotational Joint 3 - Manipulator						
<i>Mass [kg]</i>	24.0506			<i>Dimension [m]</i>	1.900	
<i>Inertia Matrix [kg m²]</i>	7.2737	0	0	<i>Orientation [deg]</i>	<i>r</i>	90
	0	0.0769	0		<i>p</i>	0
	0	0	7.2737		<i>y</i>	180
Rotational Joint 4 - Manipulator						
<i>Mass [kg]</i>	2.1266			<i>Dimension [m]</i>	0.168	
<i>Inertia Matrix [kg m²]</i>	0.0084	0	0	<i>Orientation [deg]</i>	<i>r</i>	-90
	0	0.0068	0		<i>p</i>	0
	0	0	0.0084		<i>y</i>	0
Rotational Joint 5 - Manipulator						
<i>Mass [kg]</i>	21.8987			<i>Dimension [m]</i>	1.730	
<i>Inertia Matrix [kg m²]</i>	5.4968	0	0	<i>Orientation [deg]</i>	<i>r</i>	90
	0	0.0701	0		<i>p</i>	0
	0	0	5.4968		<i>y</i>	180
Rotational Joint 6 - Manipulator						
<i>Mass [kg]</i>	2.1266			<i>Dimension [m]</i>	0.168	
<i>Inertia Matrix [kg m²]</i>	0.0084	0	0	<i>Orientation [deg]</i>	<i>r</i>	-90
	0	0.0068	0		<i>p</i>	0
	0	0	0.0084		<i>y</i>	0
Rotational Joint 7 - Manipulator						
<i>Mass [kg]</i>	4.4304			<i>Dimension [m]</i>	0.350	
<i>Inertia Matrix [kg m²]</i>	0.0523	0	0	<i>Orientation [deg]</i>	<i>r</i>	90
	0	0.0141	0		<i>p</i>	0
	0	0	0.0523		<i>y</i>	0

Rotational Joint 8 - Connection					
<i>Mass [kg]</i>	0.0001			<i>Dimension [m]</i>	0.0001
<i>Inertia Matrix [kg m²]</i>	0.0001	0	0	<i>Orientation [deg]</i> r	0
	0	0.0001	0	p	0
	0	0	0.0001	y	0
Translational Joint 9 - Connection (Envisat Base)					
<i>Mass [kg]</i>	7490			<i>Dimension [m]</i>	10 x 2.75 x 2.075
<i>Inertia Matrix [kg m²]</i>	11113.1	397.1	848	<i>Orientation [deg]</i> r	0
	397.1	117837.3	344.2	p	60
	848	344.2	126686.9	y	0
Rotational Joint 10 → 15 - Solar Panel Boom (Spherical Connections)					
<i>Mass [kg]</i>	10.8			<i>Dimension [m]</i>	3
<i>Inertia Matrix [kg m²]</i>	0.007	0	0	<i>Orientation [deg]</i> r	-90
	0	8.1035	0	p	0
	0	0	8.1035	y	-155
Rotational Joint 16 → 28 - Solar Panel Sections					
<i>Mass [kg]</i>	23.3714			<i>Dimension [m]</i>	1.1428 x 4.97
<i>Inertia Matrix [kg m²]</i>	48.1079	0	0	<i>Orientation [deg]</i> r	0
	0	50.6518	0	p	0
	0	0	2.5438	y	0

Table 4.3: List of parameters of the model used for the simulation.

2. the translational DoF is to simulate a slip behaviour of the clamping.

To set all flexibilities of the appendages, first an analysis on the panel was done: the closer stiffness parameter to the real value of 0.05 Hz for the first eigenfrequency mode was 11000 Nm/rad. The damping parameter was arbitrary set as the 10%, $D_{pan} = 1100 \text{ Nms/rad}$.

The other stiffness and damping coefficient were estimated as follows:

- for the two spherical joints, $K_{sph} = 11000 \text{ Nm/rad}$, $D_{sph} = 1100 \text{ Nms/rad}$;
- for the rotational joint of the connection, $K_{conn} = 10000 \text{ Nm/rad}$, $D_{conn} = 1000 \text{ Nms/rad}$;
- for the prismatic joint of the connection, $K_{conn} = 60000 \text{ N/m}$, $D_{conn} = 6000 \text{ Ns/m}$.

The results of this simulation are reported in the following pages: the thrust force was applied for a duration of 400 s as a single profile and the overall simulation time was defined as 1000 s to investigate the system answer after the thrust force.

As in the previous section the CoG of the system is shown in Figure 4.15. In this case the oscillation of system CoG position is not clearly visible, due

to the fact that the thrust force is not directed exactly through the systems CoG. This causes a drift in the secondary components. In Figure 4.14 the CoG velocity is reported and also here the small oscillation are not really visible.

The connection gives to the clamping mechanism a force and a torque: in Figure 4.16 these values are shown. These forces are useful to determine the stiffness of the connection structure.

The rotations are shown in Figure 4.17 and Figure 4.18, these are divided for the solar panel sections and for the spherical joints.

The displacement as regarding rotations produces a global oscillation of the solar panel, the motion of the tip is reported in Figure 4.19: this motion is calculated in the reference frame of Envisat.

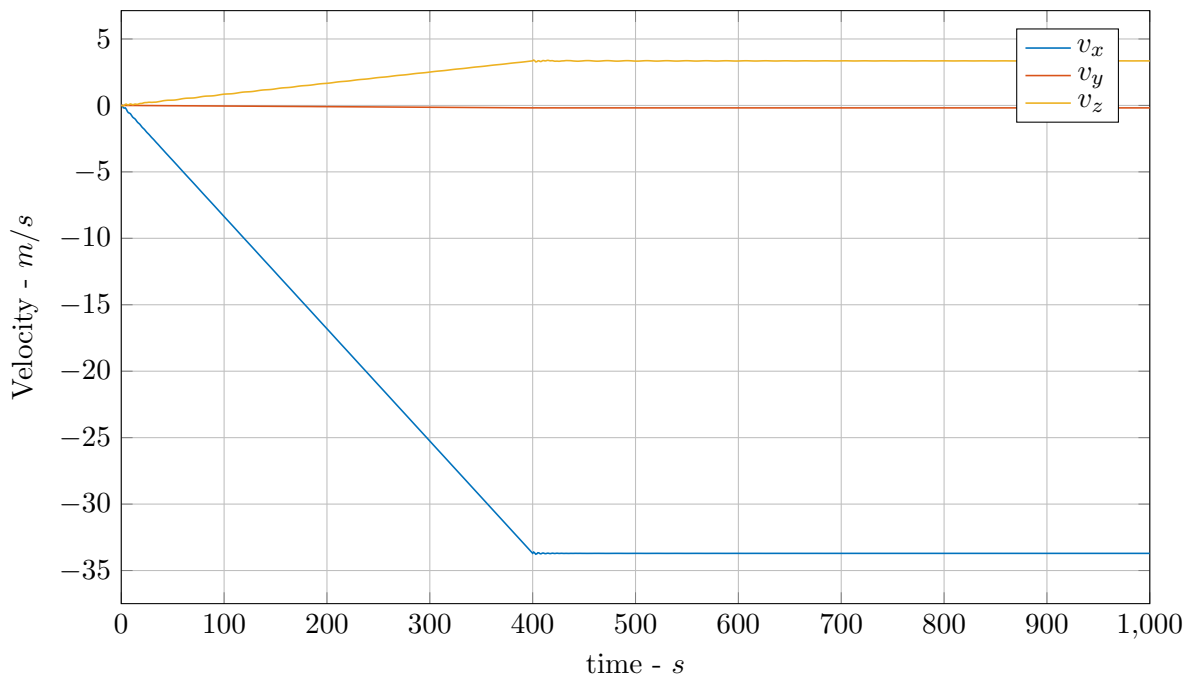


Figure 4.14: Velocity of the CoG of the system.

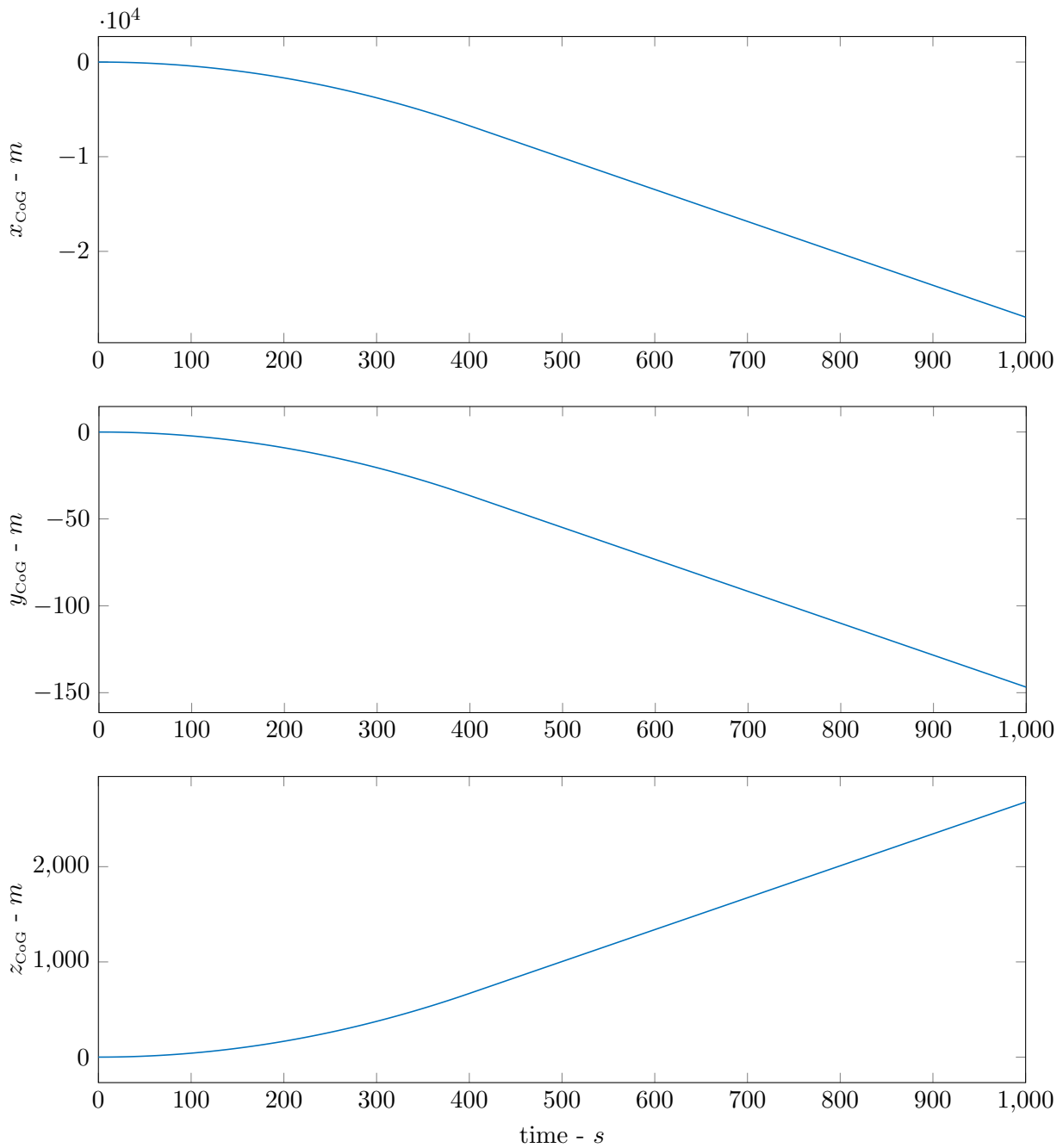
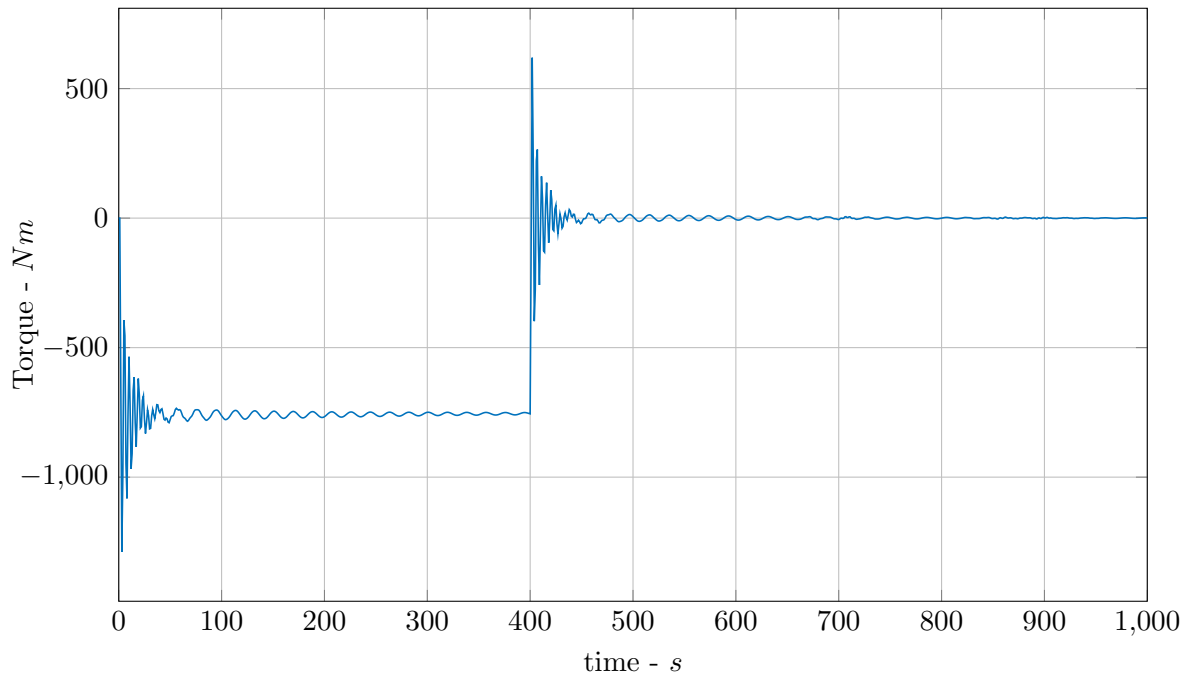
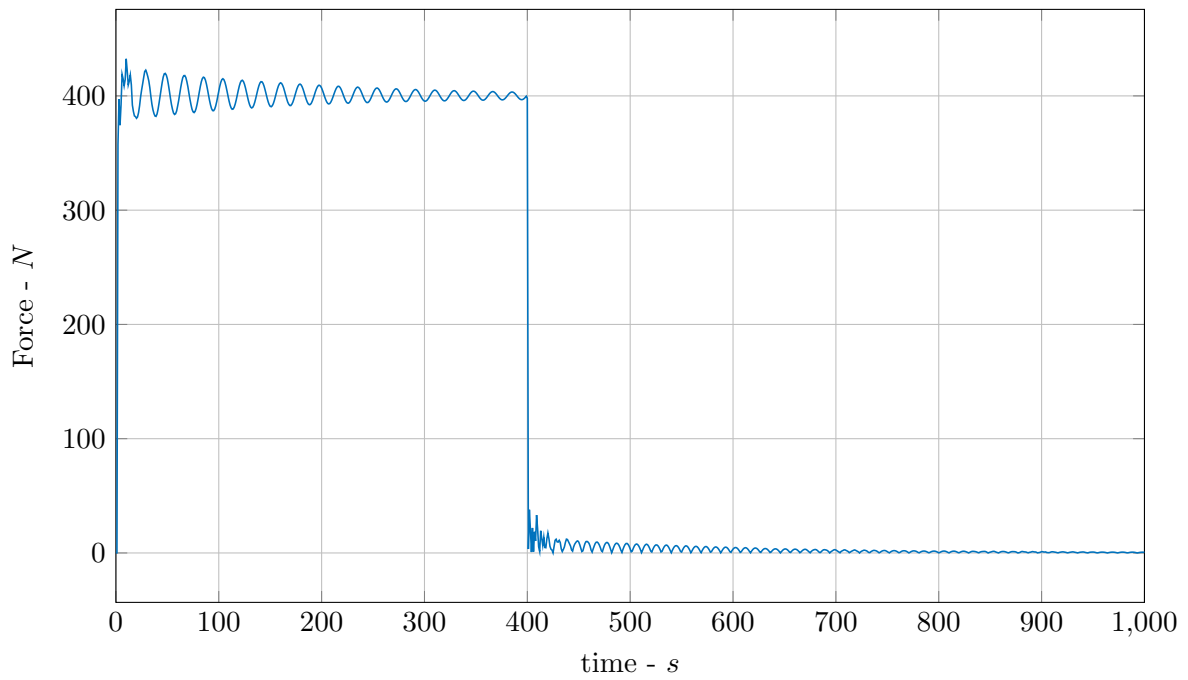


Figure 4.15: Position of the centre of gravity of the entire system during the simulation.



(a) Rotational



(b) Translational

Figure 4.16: Connection force and torque provided by the clamping mechanism in absolute value.

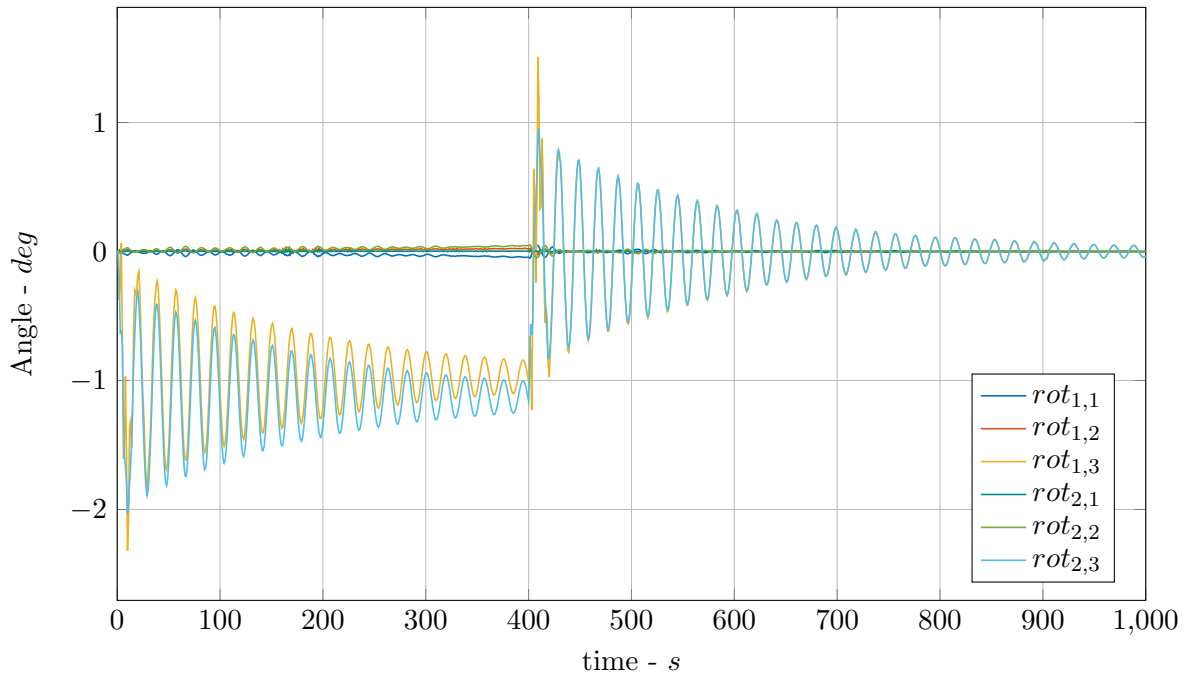


Figure 4.17: Rotation of the spherical joints of the boom.

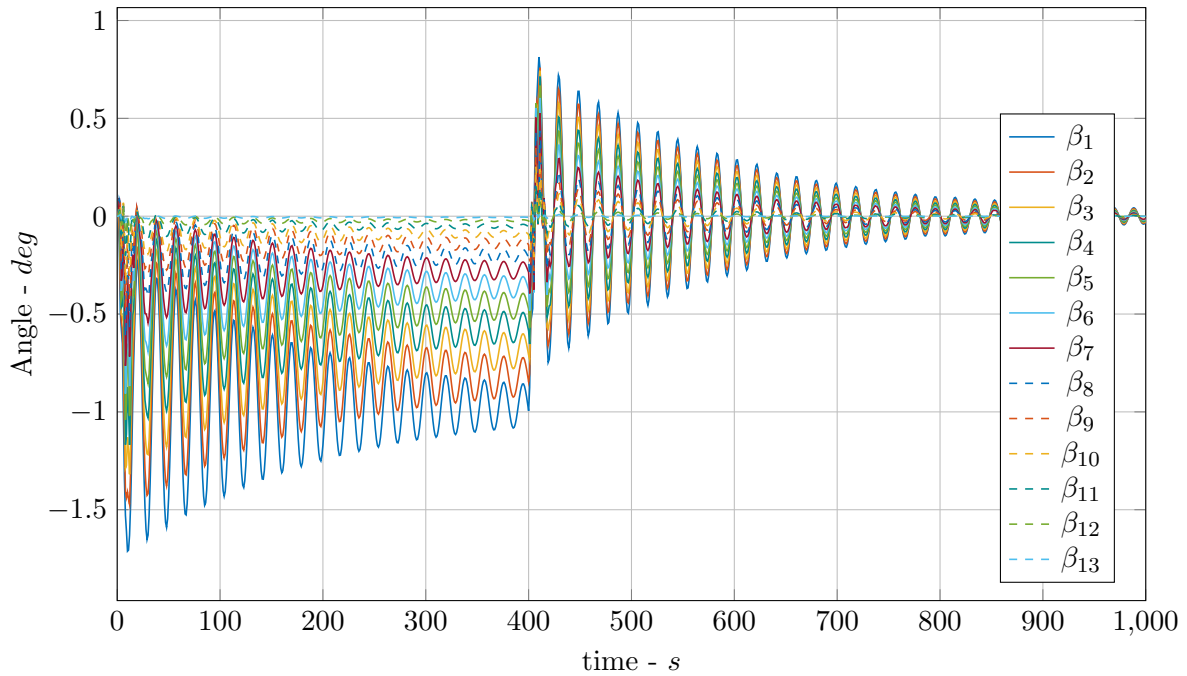


Figure 4.18: Rotation of the section of Envisat's solar panel.

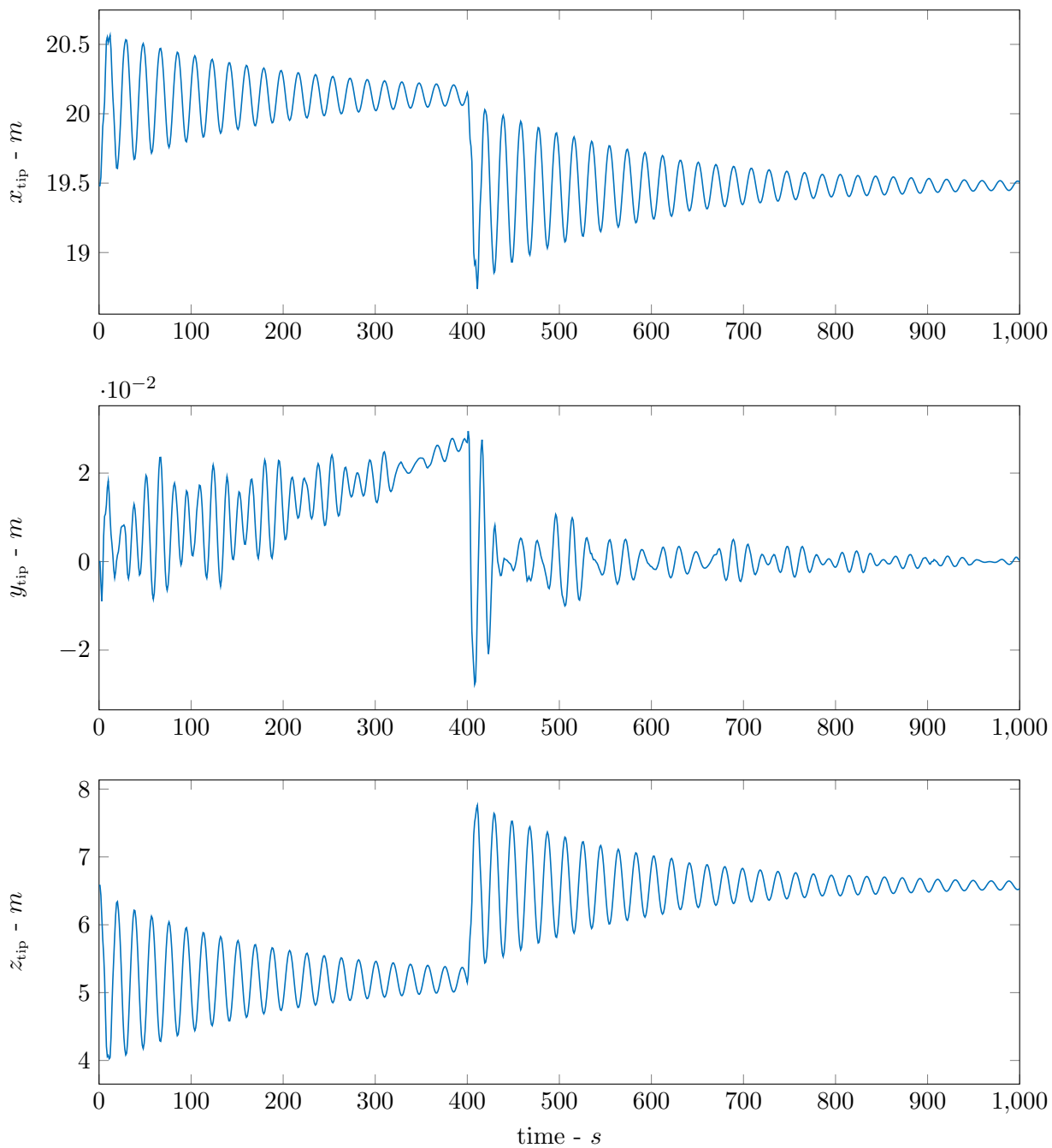


Figure 4.19: Position of the tip of the solar panel in Envisat RS.

4.5.3 Clamping on Payload Adapter - Rotated

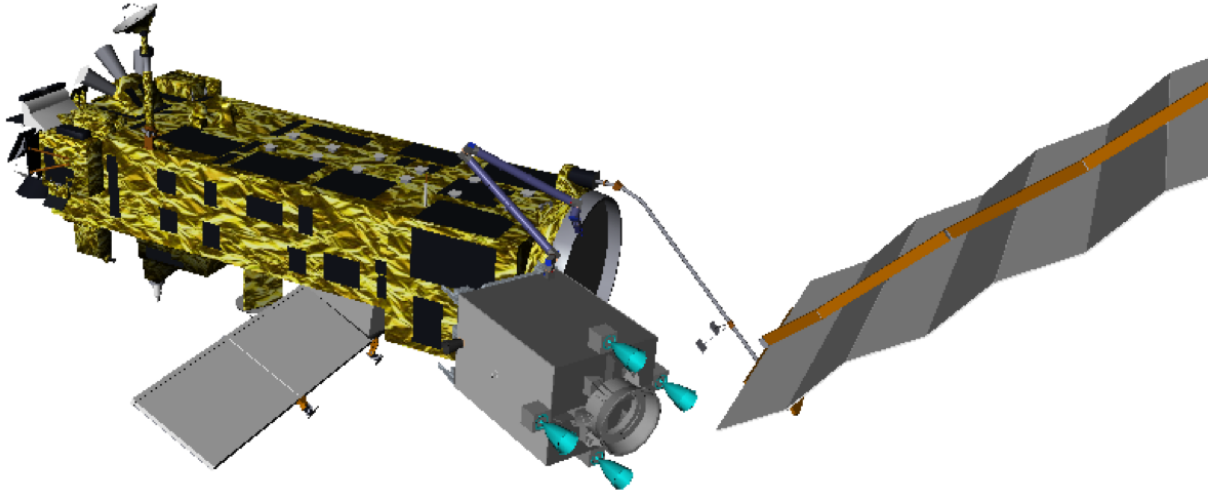


Figure 4.20: Representation of the clamping on payload adapter in rotated configuration.

The new configuration analysed is also referring to the phase B of the project, but it is slightly different from the previous: the clamping position on Envisat's Payload Adapter was changed in order to reduce the drag force in the atmosphere re-entry and also the oscillation of the solar panel when the thrust force is active.

As shown in Figure 4.20, the Chaser is still tilted with respect to the Envisat base, but there is an additional rotation of 90° around the x -axis; all the body reference frames and the proprieties of the links are not changed from the previous configuration (Figure 4.13 and Table 4.3).

As result also in this case are shown the position of the entire system CoG and its velocity (Figure 4.21 and Figure 4.22); the difference is not significant with respect to the previous configuration.

A big reduction could be noticed in terms of amplitude of relative angles of the solar panel section, in Figure 4.25: in this case the displacement is 30% of the previous configuration. A different trend is shown in Figure 4.24 regarding the spherical joints, because more directions are excited even if the higher value is not changed (1°).

This corresponds in a different behaviour of the oscillation of the solar panel tip, as shown in Figure 4.26. The maximum value is less than the previous case, but the y -direction component is not zero any more. This motion is allowed by the spherical connection, so the most stressed structure is the boom that connects the main body to the panel and its mechanisms.

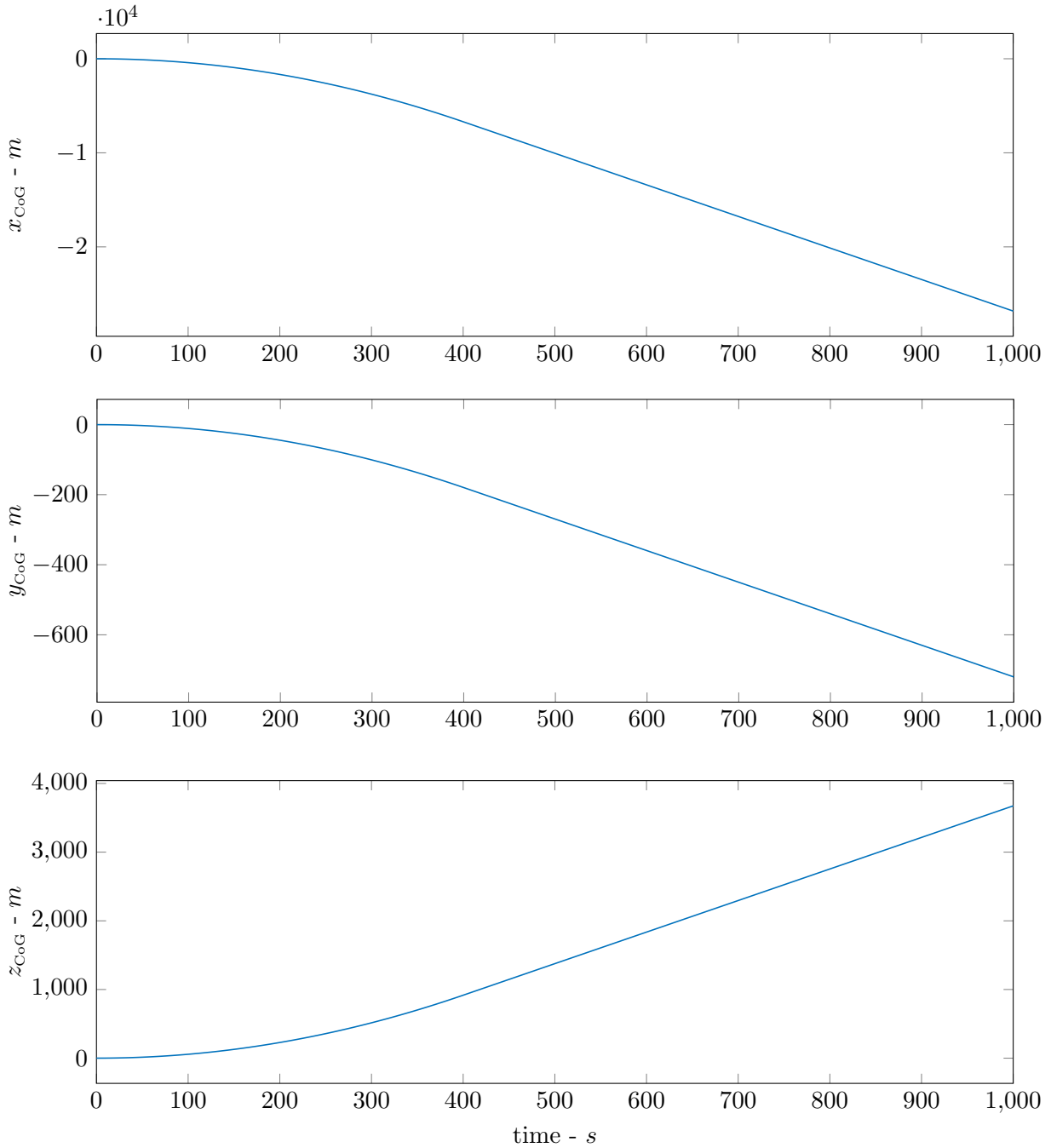


Figure 4.21: Position of the centre of gravity of the entire system during the simulation.

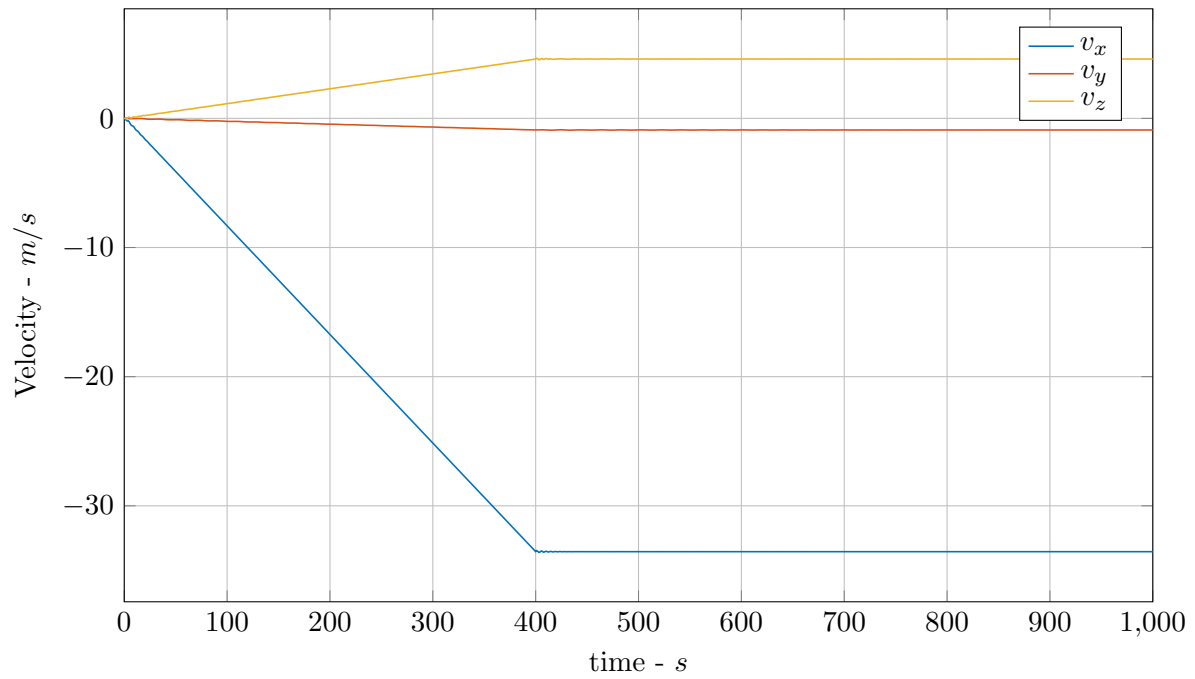
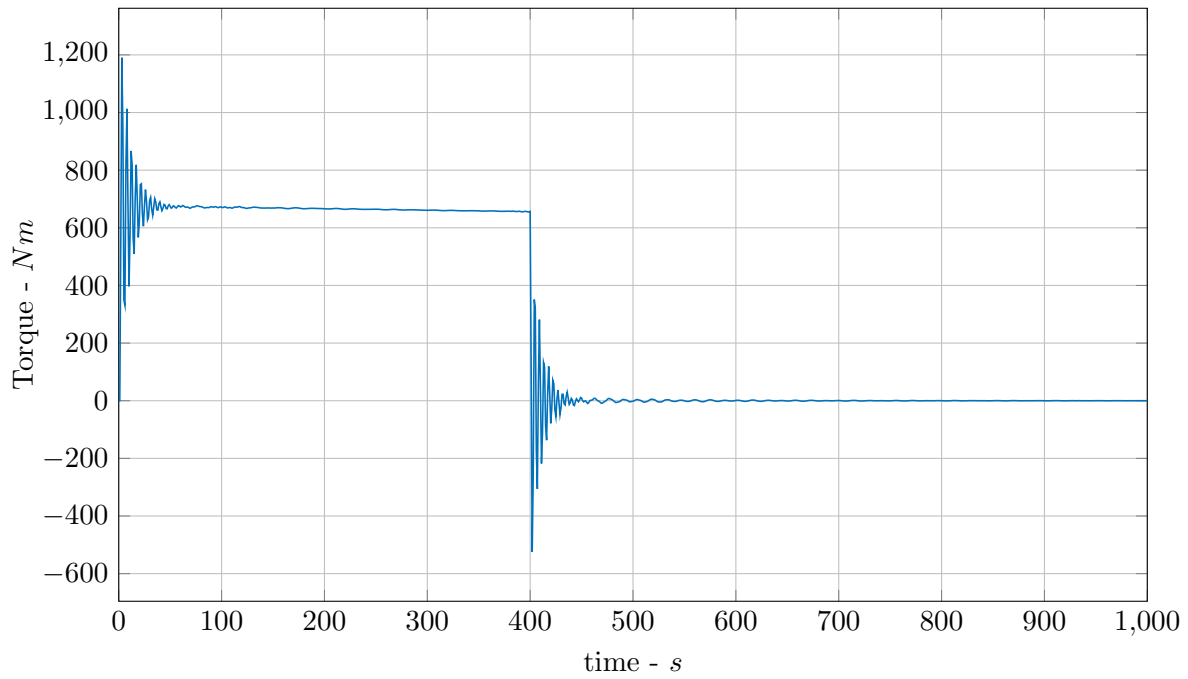
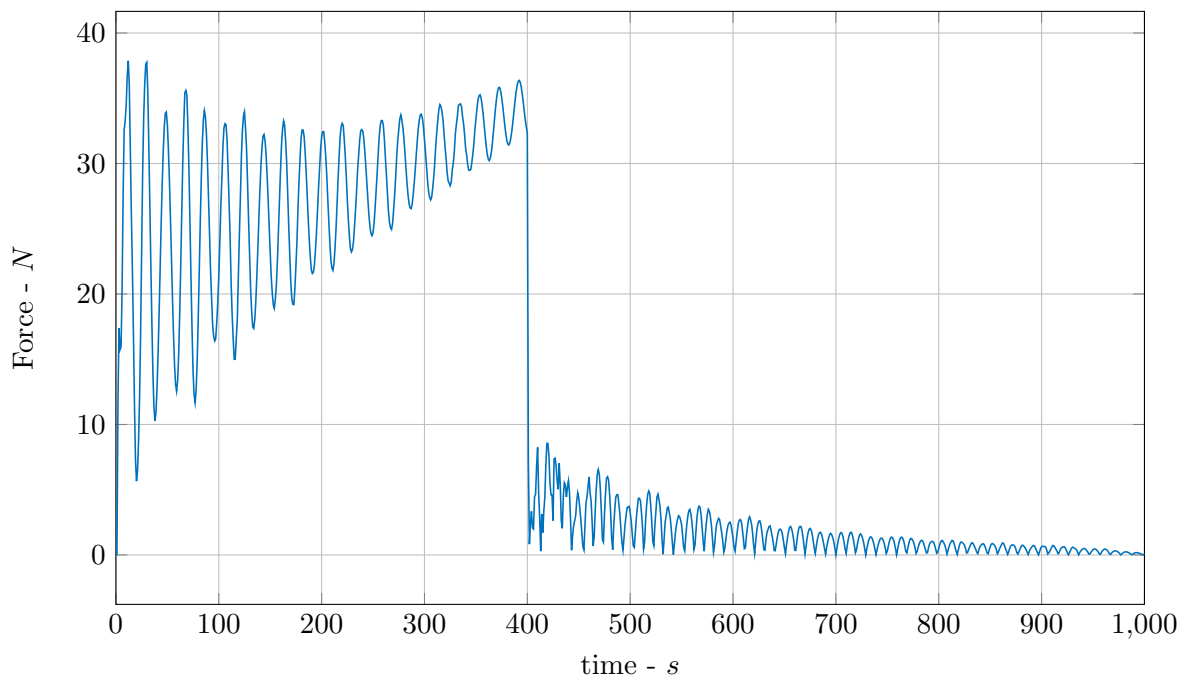


Figure 4.22: Velocity of the CoG of the system.



(a) Rotational



(b) Translational

Figure 4.23: Connection force and torque provided by the clamping mechanism in absolute value.

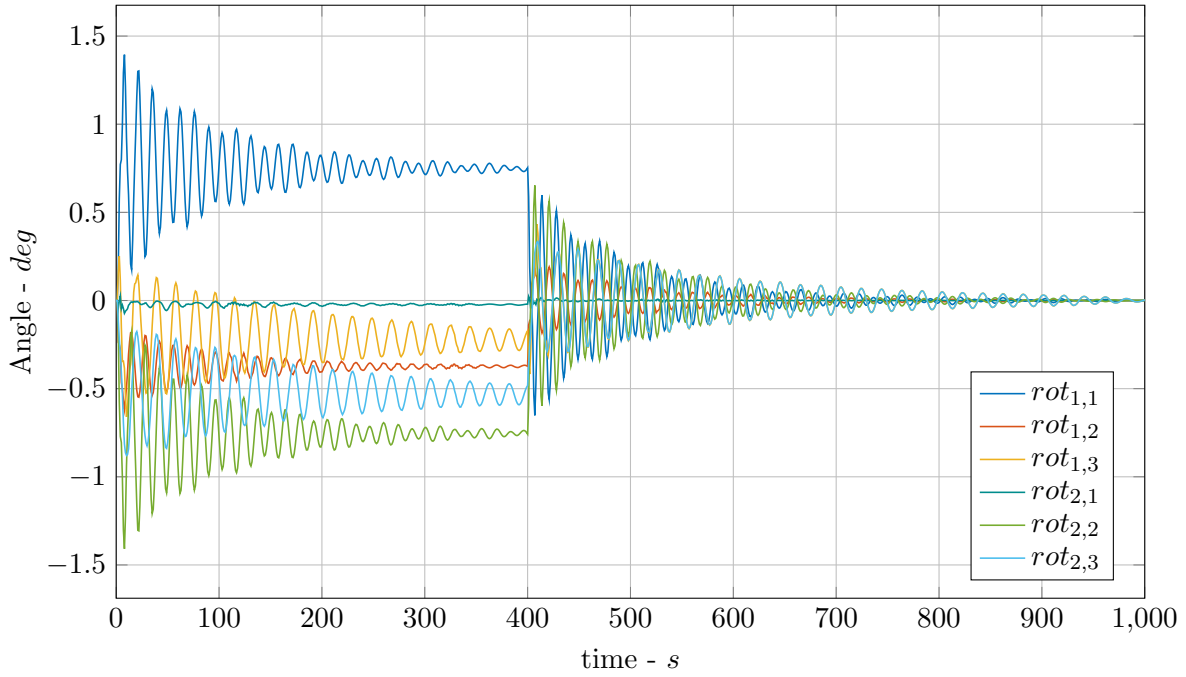


Figure 4.24: Rotation of the spherical joints of the boom.

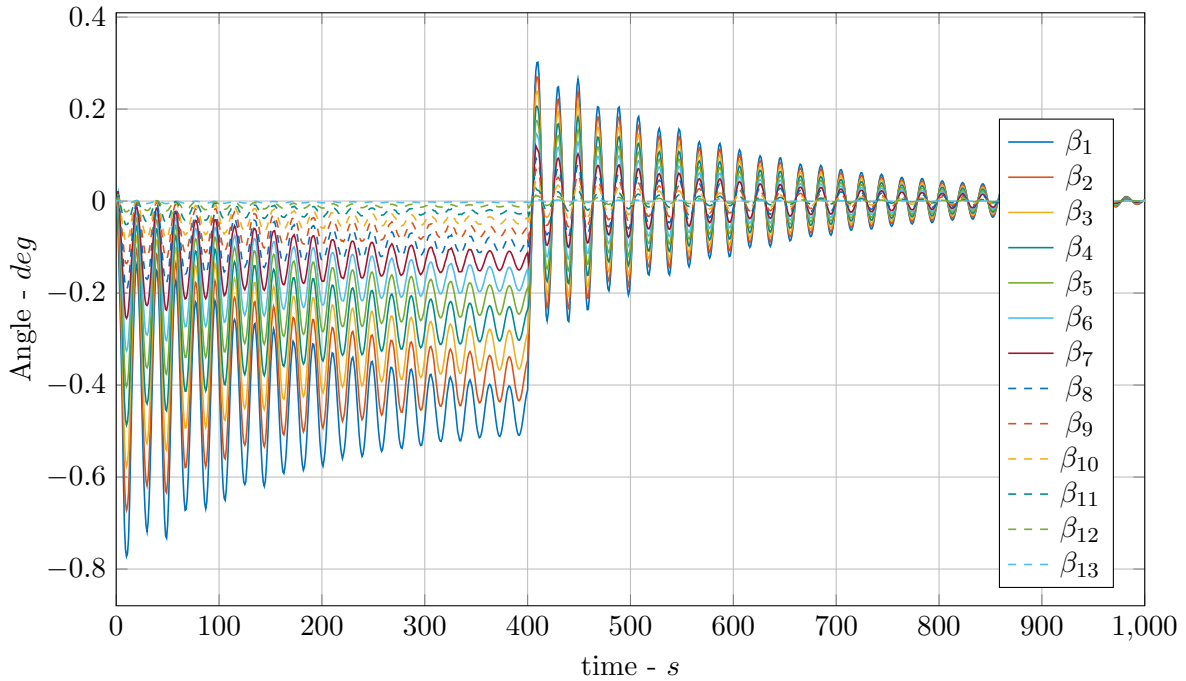


Figure 4.25: Rotation of the section of Envisat's solar panel.

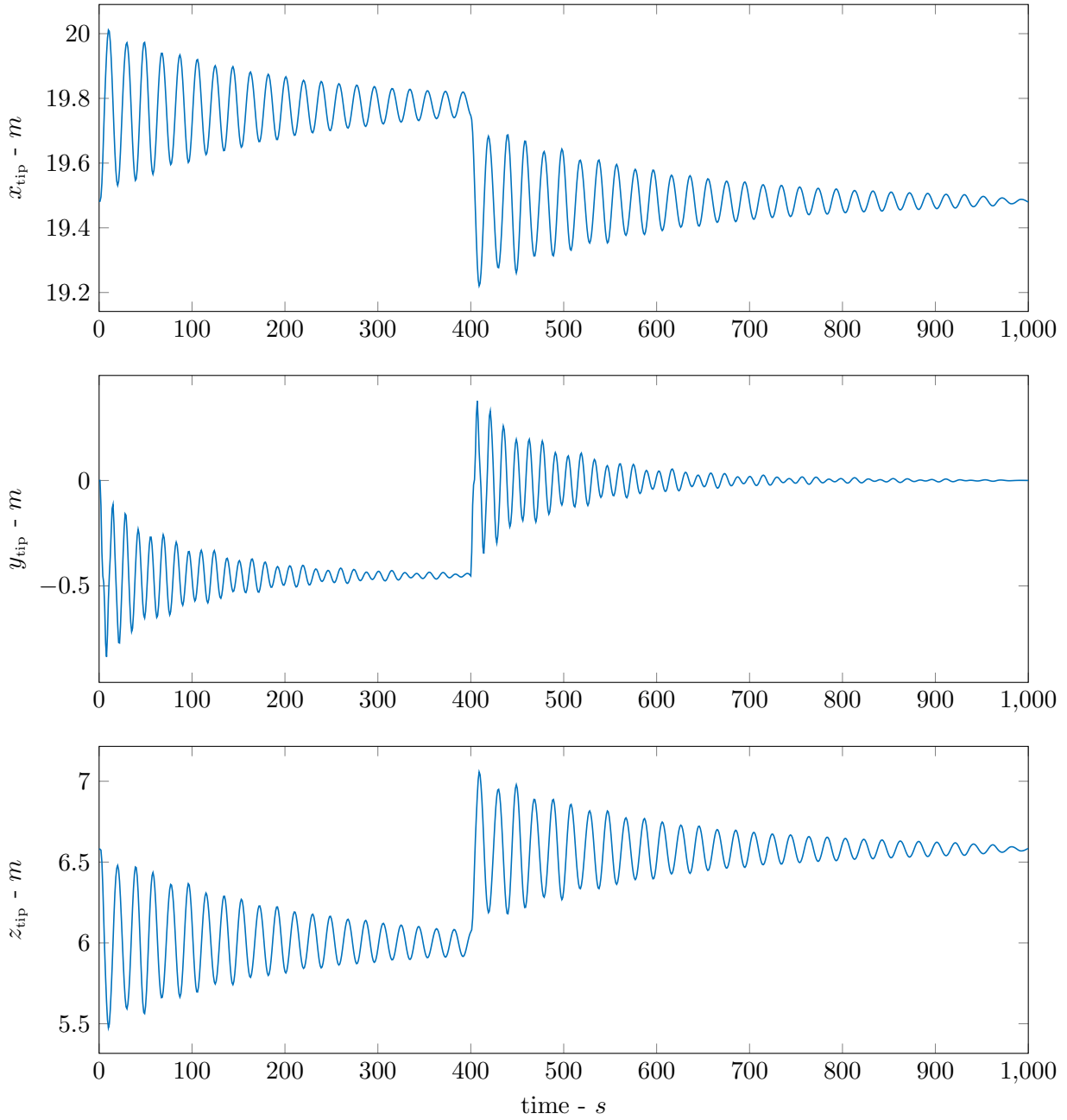


Figure 4.26: Position of the tip of the solar panel in Envisat RS.

4.6 Detumbling Scenarios

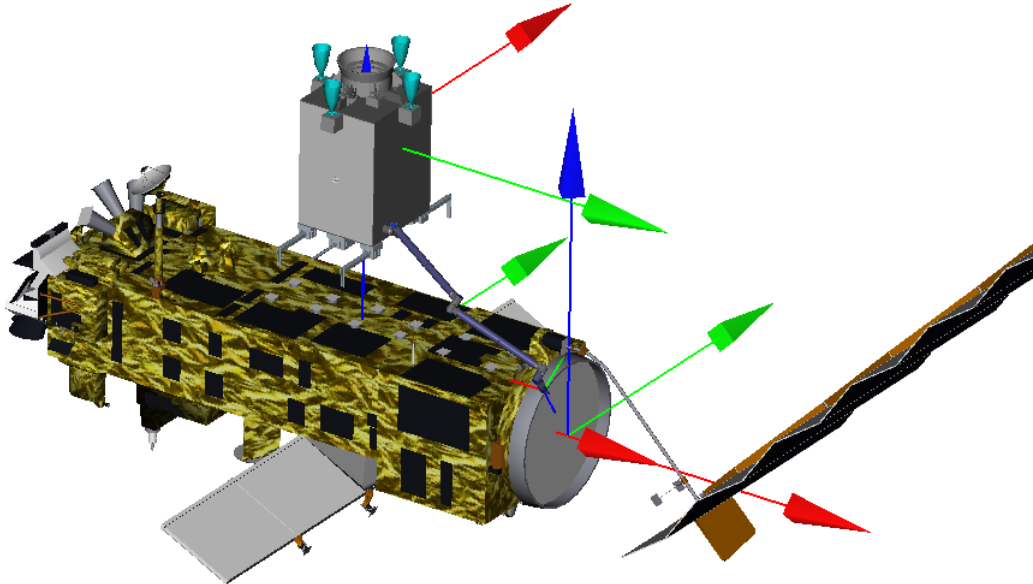


Figure 4.27: Representation of the system for detumbling configuration.

The observations of Envisat show a rotation of the satellite, but the quantitative results derived from the observations deviate significantly. For this reason a gravity stabilised Envisat cannot be assumed as a baseline due to this unexpected behaviour.

Since the basic physics of attitude dynamics are not understood, it shall be assumed that Envisat can rotate with an angular velocity of $5^\circ/s$ around any axis.

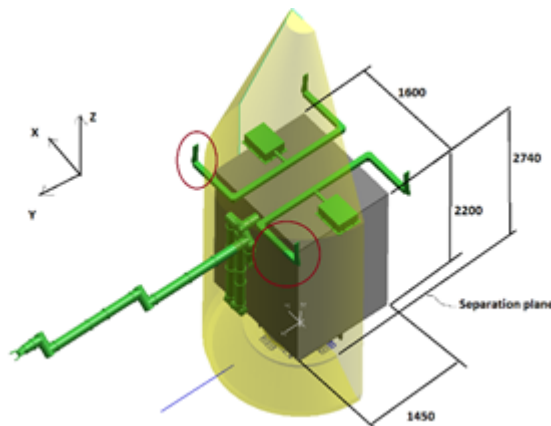


Figure 4.28: Representation of the Chaser Geometry Fixed Frame.

For this reason it is necessary to perform a detumbling manoeuvre before the deorbit. The dynamic of the system composed as shown in Figure 4.27 by Servicer module and Envisat, connected by the robotic arm, was analysed during this particular manoeuvre.

The manoeuvre was only simulated in Simpack and the proposed scenario are three: one rotation around each axis.

In Figure 4.28 it is shown the Chaser spacecraft Geometry Fixed Frame (CGFF) coordinate system: in this frame all the forces/torque provided by the thrusters are expressed. The origin of this reference frame is the geometrical centre of the separation plane between the launch adapter and the Chaser spacecraft (1.334 m in the z -component between the CoG).

Base						
<i>Mass [kg]</i>	1535			<i>Dimension [m]</i>	1.6 × 1.45 × 2.74	
<i>Inertia Matrix [kg m²]</i>	938.96	0	0	<i>Orientation [deg]</i>	<i>r</i>	0
	0	1242.82	0		<i>p</i>	0
	0	0	917.48		<i>y</i>	0
Rotational Joint 1 - Manipulator						
<i>Mass [kg]</i>	2.1668			<i>Dimension [m]</i>	0.168	
<i>Inertia Matrix [kg m²]</i>	0.0086	0	0	<i>Orientation [deg]</i>	<i>r</i>	90
	0	0.0069	0		<i>p</i>	0
	0	0	0.0086		<i>y</i>	0
Rotational Joint 2 - Manipulator						
<i>Mass [kg]</i>	24.5056			<i>Dimension [m]</i>	1.870	
<i>Inertia Matrix [kg m²]</i>	7.4113	0	0	<i>Orientation [deg]</i>	<i>r</i>	-90
	0	0.0784	0		<i>p</i>	0
	0	0	7.4113		<i>y</i>	0
Rotational Joint 3 - Manipulator						
<i>Mass [kg]</i>	2.1668			<i>Dimension [m]</i>	0.168	
<i>Inertia Matrix [kg m²]</i>	0.0086	0	0	<i>Orientation [deg]</i>	<i>r</i>	90
	0	0.0069	0		<i>p</i>	0
	0	0	0.0086		<i>y</i>	180
Rotational Joint 4 - Manipulator						
<i>Mass [kg]</i>	22.3130			<i>Dimension [m]</i>	1.730	
<i>Inertia Matrix [kg m²]</i>	5.6007	0	0	<i>Orientation [deg]</i>	<i>r</i>	-90
	0	0.0714	0		<i>p</i>	0
	0	0	5.6007		<i>y</i>	0

Rotational Joint 5 - Manipulator					
Mass [kg]	2.1668			Dimension [m]	0.168
Inertia Matrix [kg m²]	0.0086	0	0	Orientation [deg] <i>r</i>	90
	0	0.0069	0	<i>p</i>	0
	0	0	0.0086	<i>y</i>	180
Rotational Joint 6 - Manipulator					
Mass [kg]	2.1668			Dimension [m]	0.168
Inertia Matrix [kg m²]	0.0086	0	0	Orientation [deg] <i>r</i>	90
	0	0.0069	0	<i>p</i>	0
	0	0	0.0086	<i>y</i>	0
Rotational Joint 7 - Manipulator					
Mass [kg]	4.5142			Dimension [m]	0.350
Inertia Matrix [kg m²]	0.0533	0	0	Orientation [deg] <i>r</i>	-90
	0	0.0144	0	<i>p</i>	0
	0	0	0.0533	<i>y</i>	0
Envisat					
Mass [kg]	7828			Dimension [m]	10 x 2.75 x 2.075
Inertia Matrix [kg m²]	17023	397.1	-2171	Orientation [deg] <i>r</i>	180
	397.1	124826	344.2	<i>p</i>	0
	-2171	344.2	129112	<i>y</i>	90

Table 4.4: List of parameters of the model used for the Simpack simulation of the detumbling manoeuvre.

The grasping point is on the Envisat payload adapter: its coordinate in the reference system of Envisat CoG (see Figure 4.27) and the angle of the robotic arm are:

$$\mathbf{r}_{grasp} = \begin{bmatrix} 3.905 \\ -0.7 \\ 1.08 \end{bmatrix} m$$

$$\boldsymbol{\theta}_{grasp} = [125.438 \quad -27.053 \quad -63.216 \quad -45.961 \quad -39.113 \quad -50.135 \quad 0] \text{ deg}$$

The Inertial Reference Frame (IRF) is positioned at the initial time on the CoG of the Chaser Satellite. The used data of the model used in the simulation are listed in Table 4.4. The orientation of Envisat reference frame is shown in Figure 4.27 and its origin is in the CoG of Envisat (3.905 m in the *x*-component between the payload adapter plane).

In this analysis the force is the only input to the system, that is not rotating at the initial time: the manoeuvre is still the same, as the relative velocity between Envisat and the chaser is zero. The model consider also that the panel is a rigid structure connected to the main body of Envisat.

The forces and torques are considered constant during the 1 s period, as the considered strategy uses a ON/OFF thrusters without pulse modulation.

The plots in the following pages show, for each scenario considered:

- the force profile applied (Figure 4.29, 4.32 and 4.35);
- the torque applied by the thrusters (Figure 4.30, 4.33 and 4.36);
- the results in terms of the torques on the joints of the robotic arm (Figure 4.31, 4.34 and 4.37).

The highest torques result when the servicer stabilises the target satellite along its main axis of inertia; as expected, the torques in the second scenario are significant higher than the others.

However, in conclusion, for each scenario the robotic arm is not capable to support the detumbling manoeuvre because the maximum acceptable torque on the joints is limited to 80 Nm, so a clamping connection to Envisat must be taken into account also for this manoeuvre.

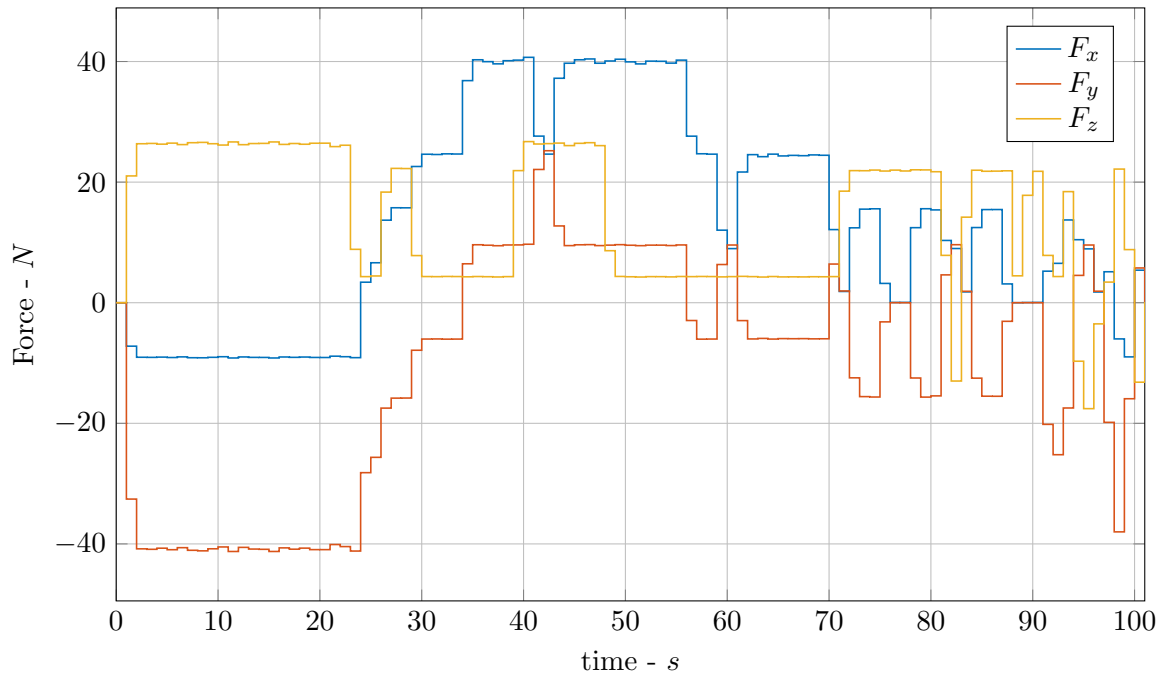


Figure 4.29: Force applied by the thruster on the Chaser base to stabilize a rotation around x -axis (Scenario 1).

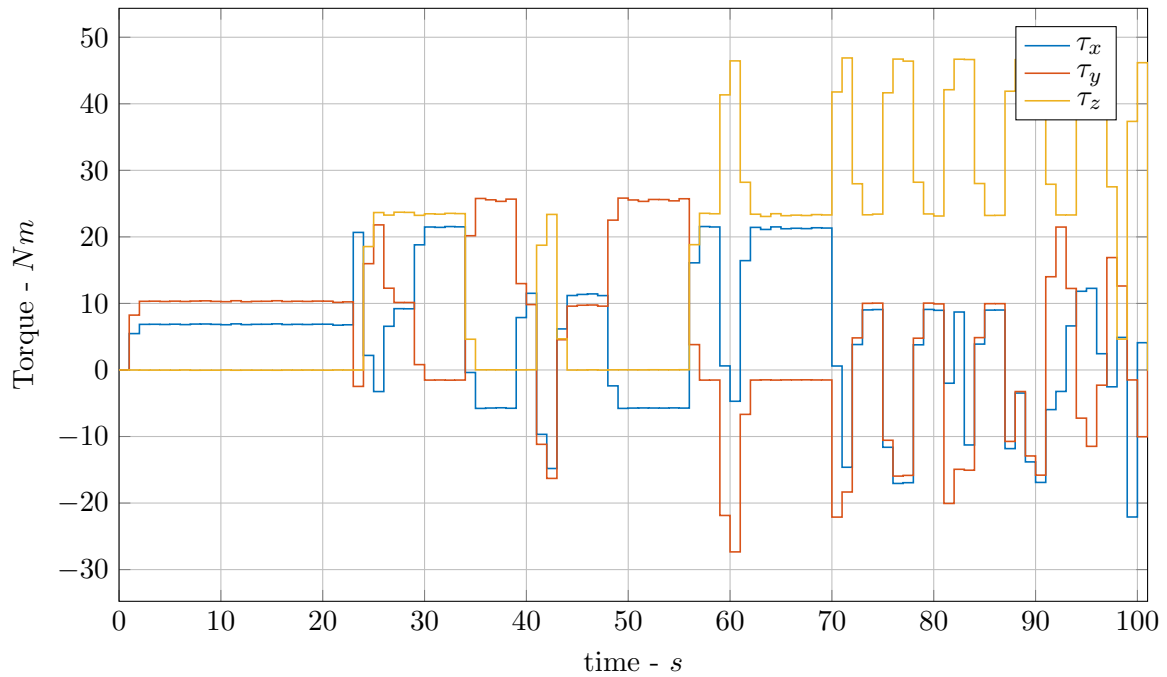


Figure 4.30: Torque applied by the thruster on the Chaser base to stabilize a rotation around x -axis (Scenario 1).

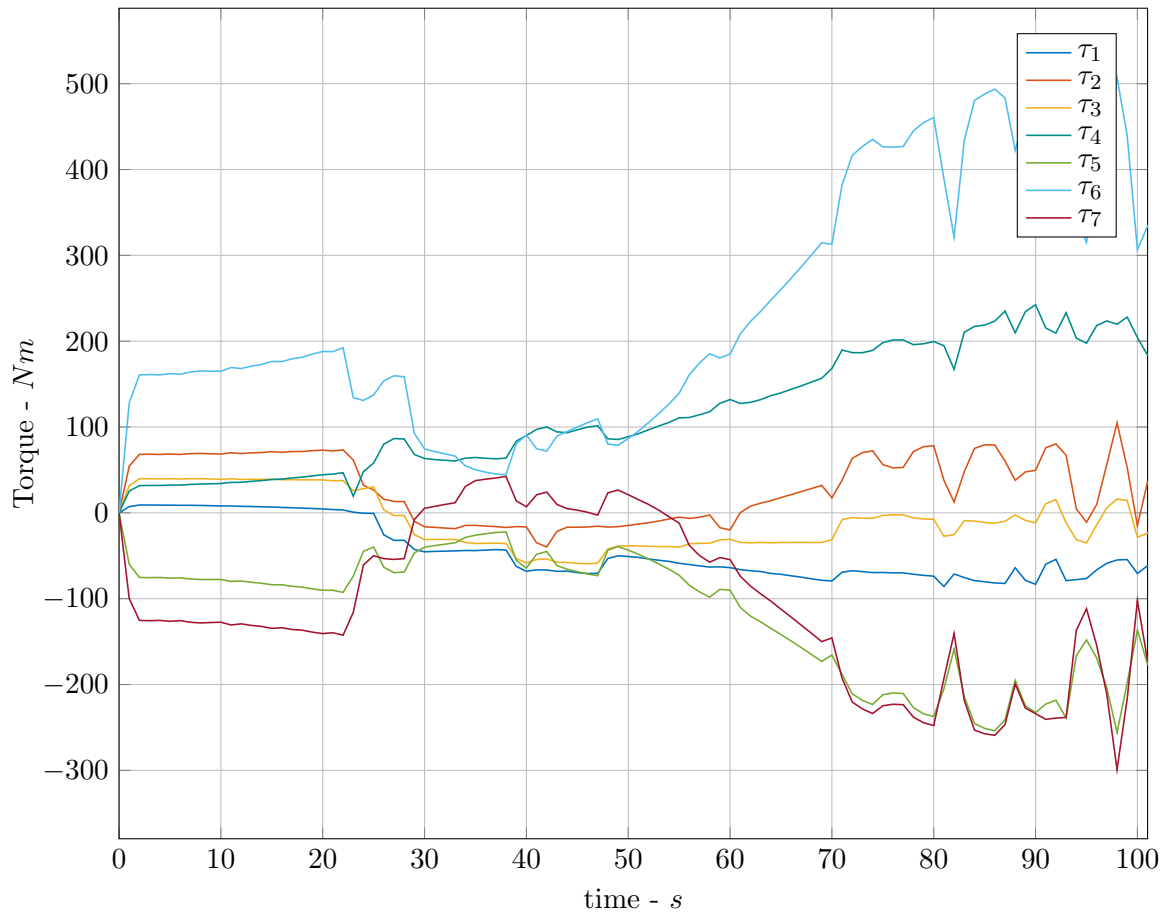


Figure 4.31: Torque in the arm Joint during the stabilisation of Scenario 1.

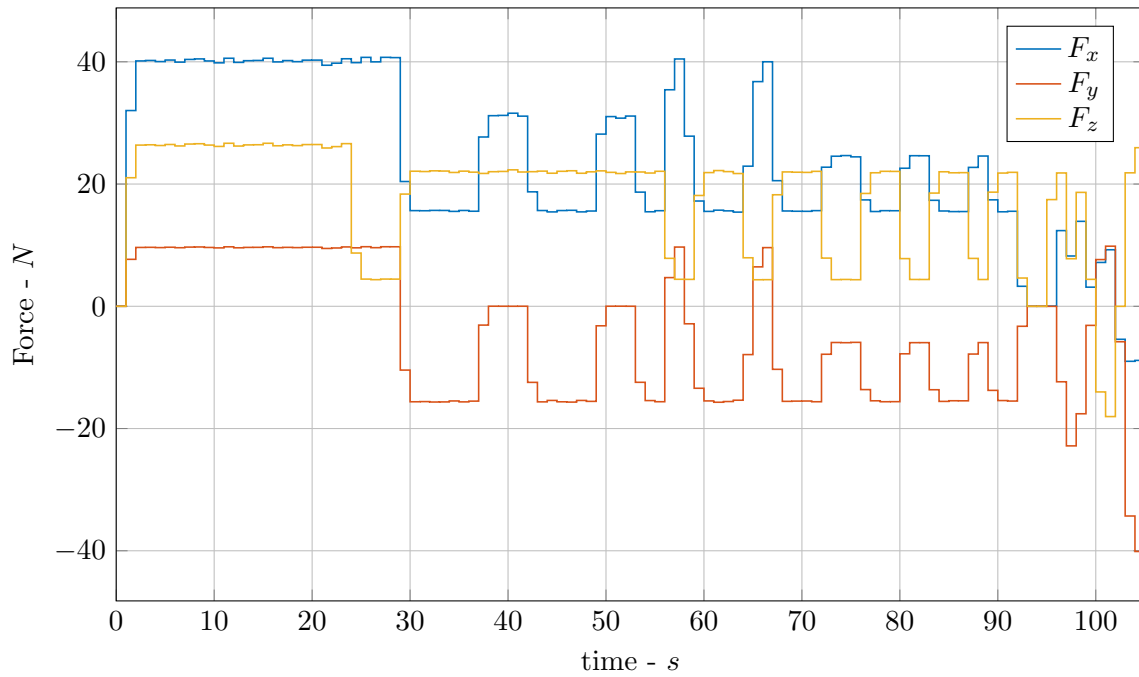


Figure 4.32: Force applied by the thruster on the Chaser base to stabilize a rotation around y -axis (Scenario 2).

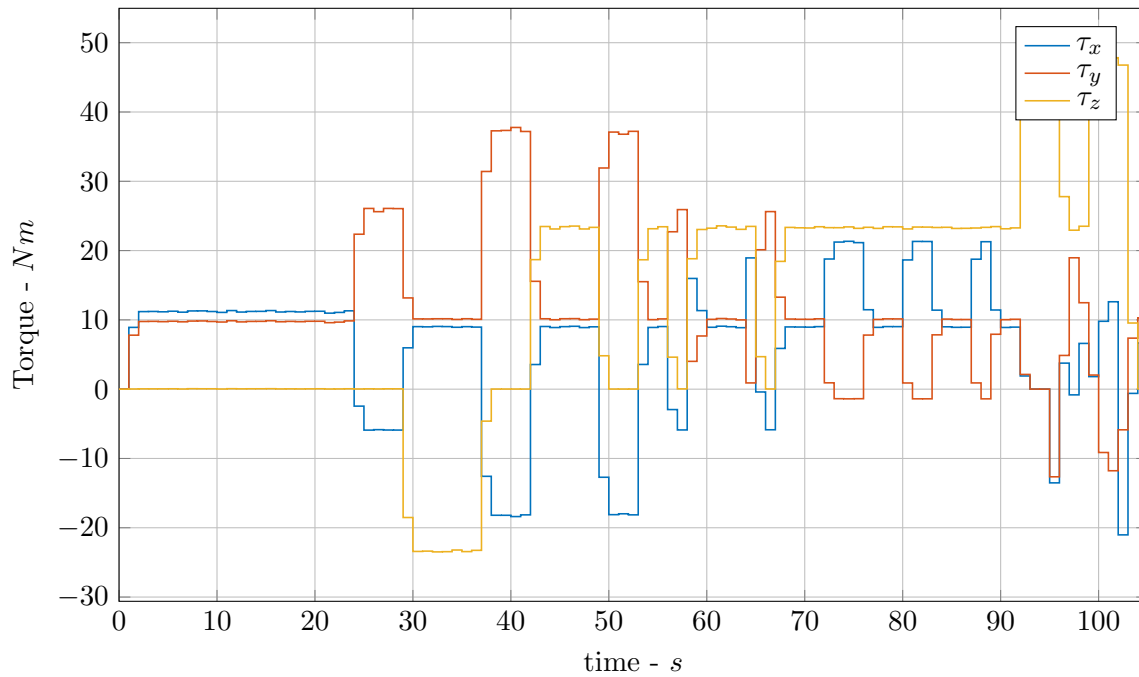


Figure 4.33: Torque applied by the thruster on the Chaser base to stabilize a rotation around y -axis (Scenario 2).

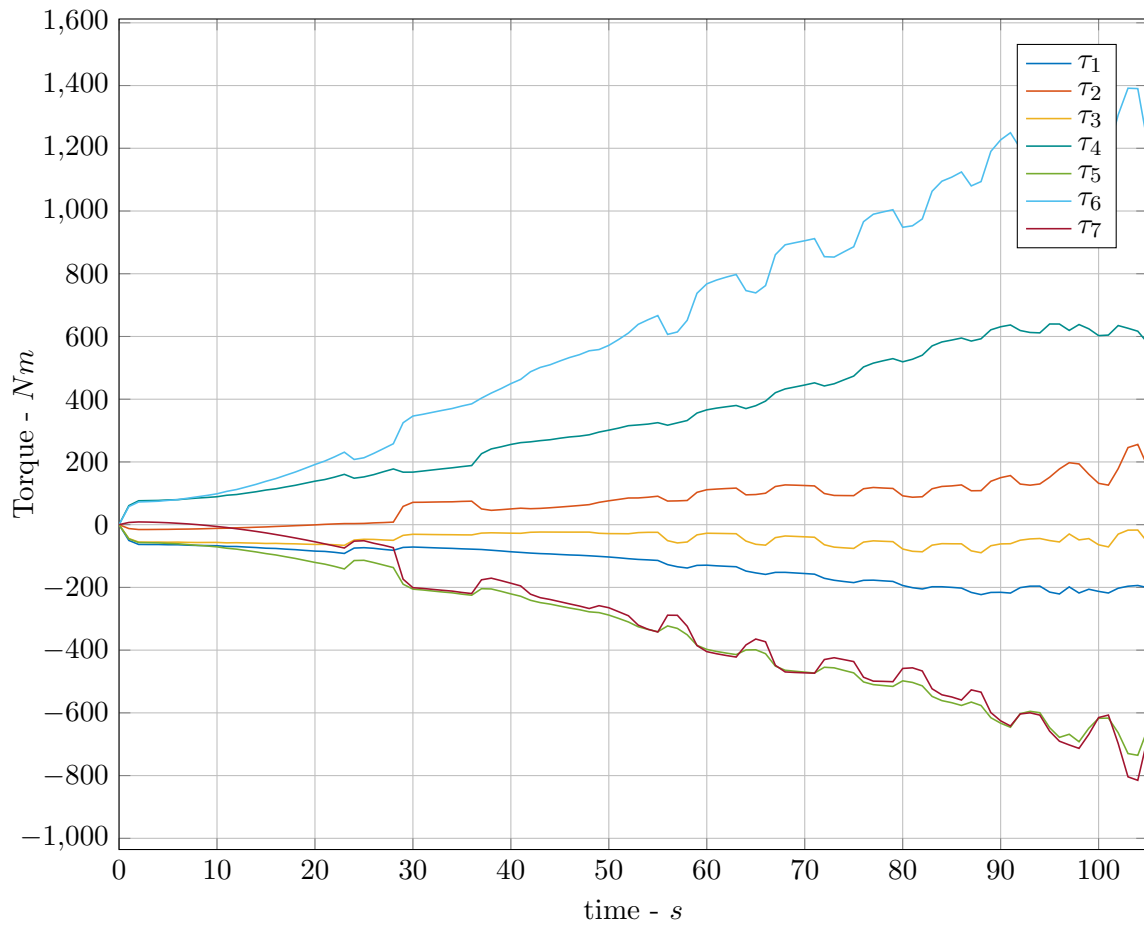


Figure 4.34: Torque in the arm Joint during the stabilisation of Scenario 2.

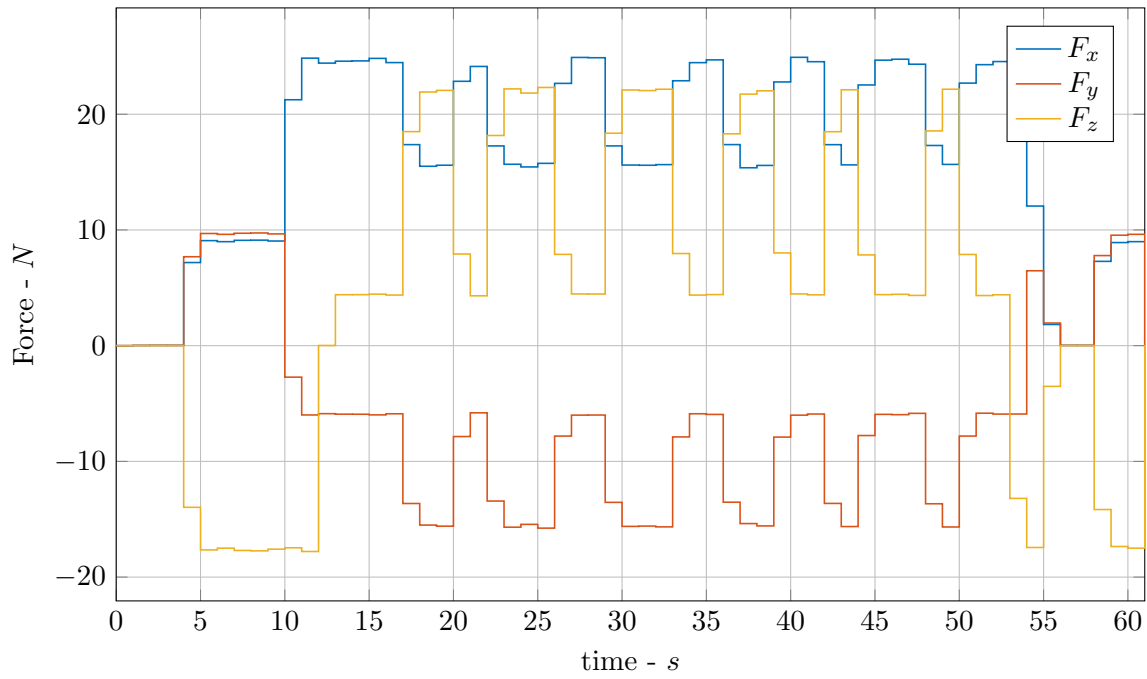


Figure 4.35: Force applied by the thruster on the Chaser base to stabilize a rotation around z -axis (Scenario 3).

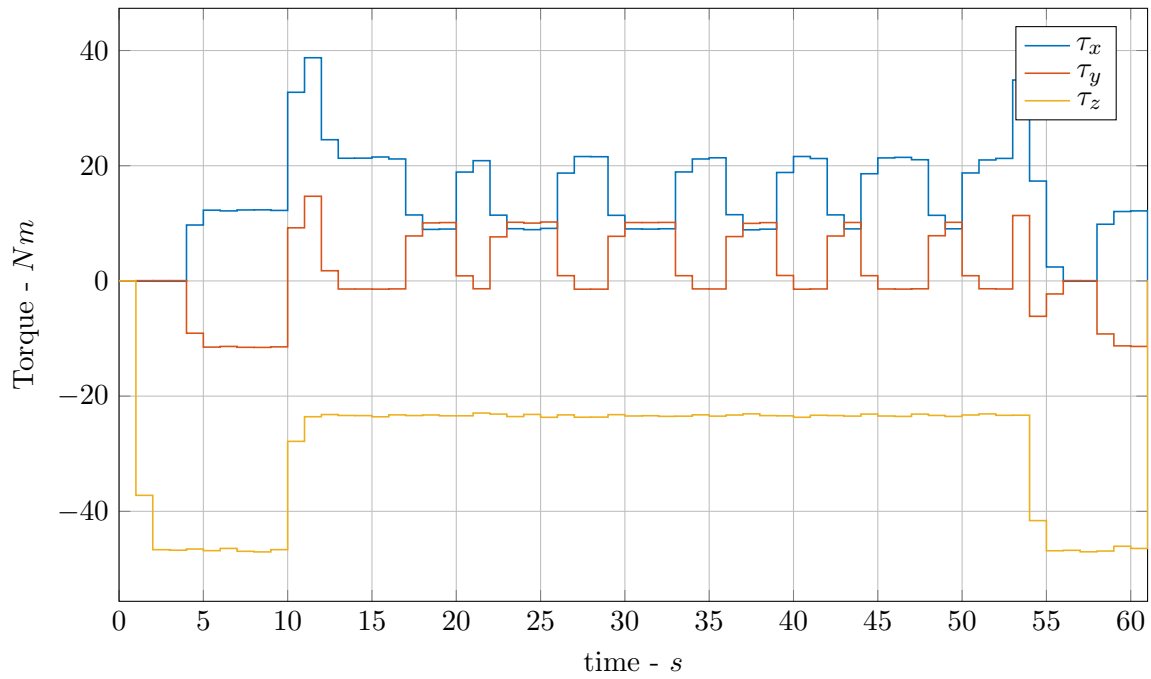


Figure 4.36: Torque applied by the thruster on the Chaser base to stabilize a rotation around z -axis (Scenario 3).

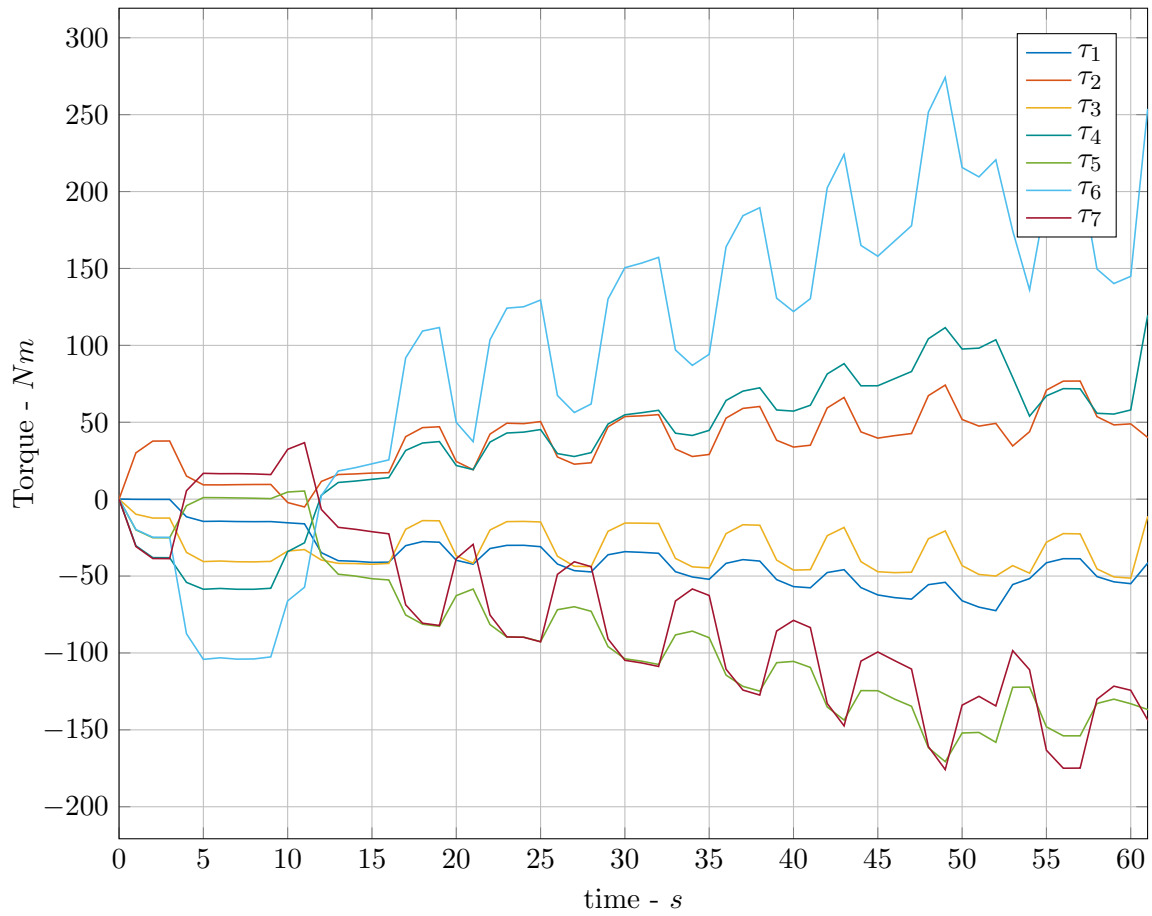


Figure 4.37: Torque in the arm Joint during the stabilisation of Scenario 3.

Chapter 5

Closed Loop Systems

5.1 Problem Statements

As analysed in the previous Chapter, the motion of the solar panel during the deorbiting phase is consistent and needs to be damped somehow. One method could be to use the manipulator: in order to do so, the robotic arm should grasp the solar panel and apply a force to damp its oscillations.

This case involves to consider a model with closed loop dynamics: this means that it is possible to trace a circuit from one link back to itself, without traversing any joint more than once.

The presence of kinematic loops brings a new level of complexity to the dynamics problem: new formulations are required, new problems arise and the systems exhibit new behaviours.

The SpaceDyn library, however, lacks the functionality of modelling robotic systems with closed kinematic loops, so a new algorithm was implemented and added to the library; the following Section explains the theory behind closed loops and how the implemented functions work.

5.2 Theoretical Background

There are two main strategies for formulating the equations of motion for a closed loop system; they are:

- start with a set of unconstrained bodies and apply all the joint constraints simultaneously;
- start with a spanning tree version of the system and apply the loop closure constraints.

The first method results in large, sparse matrix equations, but the second is the best choice for typical closed loop systems. In literature there are two different algorithms for this method: one was developed by Nakamura and

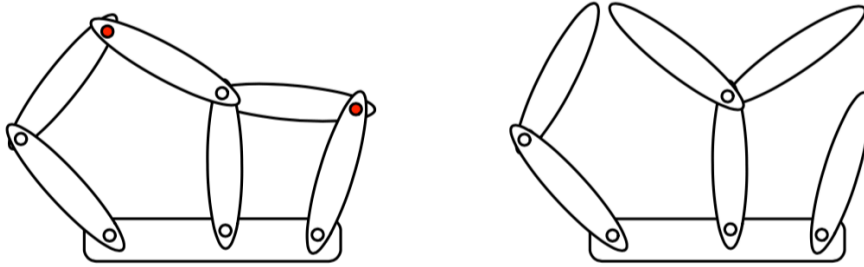


Figure 5.1: Representation of a closed loop configuration (left) with the selected loop joints in red and the corresponding spanning tree configuration (right).

Yamane [34] and it is based on the use of the generalised coordinates, which are the independent variables that represent the mobility of the kinematic loop; the other algorithm was set up by Featherstone and adds unknown reaction forces to replace the loop closing joints [31] [32] [35].

The latter was chosen for the implementation because more compatible with the already existing functions of the library and also because it automatically gives as outputs the forces of the closing joint even if it could be less efficient in terms of computational time.

The procedure can be summarised as follows:

1. formulate the equation of motion for a spanning tree (Section 4.2) of the closed loop system;
2. add terms to this equation representing the forces exerted on the tree by the loop joints;
3. formulate a kinematic equation describing the motion constraints imposed on the tree by the loop joints;
4. combine these two equations.

Taking as an example the system of Figure 5.1, if the spanning tree has n degrees of freedom, and the loop joints impose n^c constraints on the tree, then this procedure results in a system of $n + n^c$ equations in $n + n^c$ unknowns.

In the general case, defining n_k^c as the number of constraints imposed by loop joint k and N_{cl} as the number of closing loop joints, the number of constraints is:

$$n^c = \sum_{k=1}^{N_{cl}} n_k^c \quad (5.1)$$

Now, the only difference between the closed loop system and its spanning tree is that the former contains the loop joints: therefore, the equation of motion for the closed loop system can be obtained adding to the one for the spanning tree Eq. (4.1), the terms that account for the forces exerted on the tree by the loop joints.

$$\begin{bmatrix} \mathbf{H}_b & \mathbf{H}_{bm} \\ \mathbf{H}_{bm}^T & \mathbf{H}_m \end{bmatrix} \begin{bmatrix} \ddot{\mathbf{x}}_b \\ \ddot{\mathbf{q}} \end{bmatrix} + \begin{bmatrix} \mathbf{c}_b \\ \mathbf{c}_m \end{bmatrix} = \begin{bmatrix} \mathbf{F}_b \\ \boldsymbol{\tau}_m \end{bmatrix} + \begin{bmatrix} \mathbf{J}_b^T \\ \mathbf{J}_m^T \end{bmatrix} \mathbf{F}_{ee} + \begin{bmatrix} \boldsymbol{\tau}_b^a \\ \boldsymbol{\tau}_m^a \end{bmatrix} + \begin{bmatrix} \boldsymbol{\tau}_b^c \\ \boldsymbol{\tau}_m^c \end{bmatrix} \quad (5.2)$$

where $\boldsymbol{\tau}^a$ and $\boldsymbol{\tau}^c$ account respectively for the active forces and constraint forces produced by the loop joints on the base and on the manipulator.

Active forces arise from springs, dampers, actuators, acting at the loop joints; if there are no such forces acting at a particular joint, then that joint is said to be passive. On the other side, the constraint forces are the adding unknown of the system.

The loop joints impose a set of kinematic constraints on the tree, which can be collected into a single matrix equation of the form

$$\mathbf{K} \begin{bmatrix} \ddot{\mathbf{x}}_b \\ \ddot{\mathbf{q}} \end{bmatrix} = \mathbf{k} \quad (5.3)$$

where \mathbf{K} is an $n^c \times n$ matrix (remembering that n is including the 6-DoF of the base). This equation expresses the constraints at the *acceleration level*, on the grounds that it has been differentiated a sufficient number of times for the acceleration variables to appear.

As $\boldsymbol{\tau}^c$ is the force that imposes these constraints on the tree, it can be expressed in the form

$$\boldsymbol{\tau}^c = \mathbf{K}^T \boldsymbol{\lambda} \quad (5.4)$$

where $\boldsymbol{\lambda}$ is a vector of n^c unknown constraint force variables.

Equations Eq. (5.2), Eq. (5.3) and Eq. (5.4) can now be assembled into a single matrix equation, being the complete equation of motion for the closed loop system:

$$\begin{bmatrix} \mathbf{H}_b & \mathbf{H}_{bm} & & \\ \mathbf{H}_{bm}^T & \mathbf{H}_m & & \\ & & \mathbf{K}^T & \\ & & & \mathbf{0} \end{bmatrix} \begin{bmatrix} \ddot{\mathbf{x}}_b \\ \ddot{\mathbf{q}} \\ -\boldsymbol{\lambda} \end{bmatrix} = \begin{bmatrix} -\mathbf{c}_b + \mathbf{F}_b + \mathbf{J}_b^T \mathbf{F}_{ee} + \boldsymbol{\tau}_b^a \\ -\mathbf{c}_m + \boldsymbol{\tau}_m + \mathbf{J}_m^T \mathbf{F}_{ee} + \boldsymbol{\tau}_m^a \\ \mathbf{k} \end{bmatrix} \quad (5.5)$$

The coefficient matrix is symmetric, but not positive definite. If this matrix has full rank, then the equation can be solved for both $\ddot{\mathbf{q}}$ and $\boldsymbol{\lambda}$. If it does not have full rank, then some elements of $\boldsymbol{\lambda}$ will be indeterminate, but the equation can still be solved for $\ddot{\mathbf{q}}$.

5.2.1 Loop Constraint Equations

Now it is necessary to formulate the coefficients of the loop constraint equation. The velocity across loop joint k , which is denoted \mathbf{v}_{J_k} , is given by the equation:

$$\mathbf{v}_{J_k} = \mathbf{v}_{s(k)} - \mathbf{v}_{p(k)} \quad (5.6)$$

where $p(k)$ and $s(k)$ are respectively the predecessor and successor bodies of joint k . The constraint imposed by the same loop joint k is written as:

$$\mathbf{T}_k^T \mathbf{v}_{J_k} = \mathbf{0} \quad (5.7)$$

where \mathbf{T}_k denote the constraint-force subspace. Combining Eq. (5.6) and Eq. (5.7) gives a velocity constraint equation:

$$\mathbf{T}_k^T (\mathbf{v}_{s(k)} - \mathbf{v}_{p(k)}) = \mathbf{0} \quad (5.8)$$

which can be differentiated as follow to obtain an acceleration constraint equation

$$\mathbf{T}_k^T (\mathbf{a}_{s(k)} - \mathbf{a}_{p(k)}) + \dot{\mathbf{T}}_k^T (\mathbf{v}_{s(k)} - \mathbf{v}_{p(k)}) = \mathbf{0} \quad (5.9)$$

The velocity of any body in the corresponding kinematic tree can be expressed in terms of $\dot{\mathbf{q}}$ and $\dot{\mathbf{x}}_b$:

$$\mathbf{v}_i = \mathbf{J}_i \begin{bmatrix} \dot{\mathbf{x}}_b \\ \dot{\mathbf{q}} \end{bmatrix} \quad (5.10)$$

where \mathbf{v}_i is the velocity of body i , and \mathbf{J}_i is the Jacobian of same body. Likewise, the acceleration of the i -th body can be expressed in terms of $\ddot{\mathbf{q}}$ and $\ddot{\mathbf{x}}_b$ by derivating the previous:

$$\mathbf{a}_i = \mathbf{J}_i \begin{bmatrix} \ddot{\mathbf{x}}_b \\ \ddot{\mathbf{q}} \end{bmatrix} + \dot{\mathbf{J}}_i \begin{bmatrix} \dot{\mathbf{x}}_b \\ \dot{\mathbf{q}} \end{bmatrix} = \mathbf{J}_i \begin{bmatrix} \ddot{\mathbf{x}}_b \\ \ddot{\mathbf{q}} \end{bmatrix} + \mathbf{a}_i^{vp} \quad (5.11)$$

\mathbf{a}^{vp} is the ‘velocity-product’ acceleration of body i , which is the acceleration it would have if all the tree joint acceleration variables were zero. Combining Eq. (5.9) and Eq. (5.11) gives:

$$\mathbf{T}_k^T (\mathbf{J}_{s(k)} - \mathbf{J}_{p(k)}) \begin{bmatrix} \ddot{\mathbf{x}}_b \\ \ddot{\mathbf{q}} \end{bmatrix} + \mathbf{T}_k^T (\mathbf{a}_{s(k)}^{vp} - \mathbf{a}_{p(k)}^{vp}) + \dot{\mathbf{T}}_k^T (\mathbf{v}_{s(k)} - \mathbf{v}_{p(k)}) = \mathbf{0} \quad (5.12)$$

The next step is to define \mathbf{K}_{kl} and \mathbf{k}_l , constructing the matrix and the vector for Eq. (5.3):

$$\mathbf{K}_{kl} := \mathbf{T}_k^T (\mathbf{J}_{s(k)} - \mathbf{J}_{p(k)}) \quad (5.13a)$$

$$\mathbf{k}_l := -\mathbf{T}_k^T (\mathbf{a}_{s(k)}^{vp} - \mathbf{a}_{p(k)}^{vp}) - \dot{\mathbf{T}}_k^T (\mathbf{v}_{s(k)} - \mathbf{v}_{p(k)}) \quad (5.13b)$$

5.2.2 Constraint Stabilisation

The system of equations written until now is theoretically correct, but is not stable during numerical integration. The problem is this: in principle, the Eq. (5.3) behaves like a differential equation of the form

$$\ddot{\mathbf{e}} = \mathbf{0}$$

where \mathbf{e} denotes a loop closure position error; but in practice it behaves like

$$\ddot{\mathbf{e}} = \text{noise}$$

where *noise* is a small-magnitude signal representing numerical errors, such as the truncation errors in the numerical integration process.

Thus, the use of Eq. (5.3) will ensure that the acceleration errors are kept small, but there is nothing to stop an unbounded accumulation of position and velocity errors. The problem can be solved by adding a stabilisation term, \mathbf{k}_{stab} :

$$\mathbf{K} \begin{bmatrix} \ddot{\mathbf{x}}_b \\ \ddot{\mathbf{q}} \end{bmatrix} = \mathbf{k} + \mathbf{k}_{stab} \quad (5.14)$$

This standard technique is due to Baumgarte and in formulas is:

$$\mathbf{k}_{stab} = -2\alpha (\mathbf{v}_{s(k)} - \mathbf{v}_{p(k)}) - \beta^2 \boldsymbol{\delta} \quad (5.15)$$

where $\boldsymbol{\delta}$ is a measure of the degree to which the position of the spanning tree violates the constraint imposed by loop joint and α and β are two constants, usually chosen as follows:

$$\alpha = \beta = 1/t_{stab}$$

However, there is no systematic rule for choosing t_{stab} . If it is too long, then loop constraint errors accumulate faster than they decay; if it is too short, then the equations of motion become excessively stiff. A reasonable value for a large, slow industrial robot is $t_{stab} = 0.1$ s, while a smaller, faster robot might need $t_{stab} = 0.01$ s [31].

There is a temptation to choose t_{stab} as small as possible, so that position and velocity errors will decay as quickly as possible, in order to maximise the accuracy of the simulation. This is a bad strategy: the purpose of constraint stabilisation is to achieve stability, not accuracy. If the simulation is not accurate enough, then the best way to improve it is to use a better integration method and/or a shorter integration time step.

5.2.3 Loop Joint Forces

Let \mathbf{f}_k denote the force transmitted across loop joint k in the closed loop system. The effect of joint k on the spanning tree is therefore to exert a force of \mathbf{f}_k on body $s(k)$ and a force of $-\mathbf{f}_k$ on body $p(k)$. Now, if a spatial force of \mathbf{f} is applied to body i in a kinematic tree, then it has the same effect on the tree as a joint-space force of τ , where:

$$\tau = \mathbf{J}_i^T \mathbf{f}$$

Therefore, the effect of joint k on the spanning tree is equivalent to a joint-space constrained force:

$$\tau = \left(\mathbf{J}_{s(k)}^T - \mathbf{J}_{p(k)}^T \right) \mathbf{f}_k^c = \mathbf{J}_l^T \mathbf{f}_k^c$$

Then, if τ_c represents the net effect of all the constraint forces at the loop joints, each loop joint should be taken into account:

$$\tau_c = \sum_{l=1}^{N_{cl}} \mathbf{J}_l^T \mathbf{f}_k^c \quad (5.16)$$

However, the constraint force at joint k can also be expressed in the form of generalised force $\boldsymbol{\lambda}$ with the use of a transformation matrix:

$$\mathbf{f}_k^c = \mathbf{T}_k \boldsymbol{\lambda} \quad (5.17)$$

Now, substituting Eq. (5.17) in Eq. (5.16) it is possible to recognise the definition of the matrix of constraints \mathbf{K} (defined in Eq. (5.12) and Eq. (5.13)).

$$\tau_c = \sum_{l=1}^{N_{cl}} \mathbf{J}_l^T \mathbf{T}_k \boldsymbol{\lambda} = \mathbf{K} \boldsymbol{\lambda} \quad (5.18)$$

5.2.4 Model Assumptions

The SpaceDyn library used until here does not have any functions for the closed loop analysis, so, focusing on the forward dynamics, some functions were created. In order to do this, for the first time with this theory and

with the free floating system, the following assumptions were considered to create simple, but effective extension of SpaceDyn to closed loop.

Each Closing Joint has zero-DoF. This means that the predecessor and the successor bodies of this joint are considered as the same body. Having no relative translation and rotation means that any relative velocity or relative acceleration are considered. For this reason, the constraint-force subspace in Eq. (5.7) is equal to the identity matrix and its time derivate is zero.

$$\mathbf{T}_k^T = \mathbf{I} \quad \text{and} \quad \dot{\mathbf{T}}_k^T = \mathbf{0}$$

Each Closing Joint is Passive. This means that any torque is applied on the closing joint, so in the Eq. (5.2) each τ^a is zero. This simplified version of the Featherstone theory is still very useful, because if one would model a closing joint which can rotate or has a torque acting at the loop joint, it is possible to add a mass-less link to include that features and virtually cut the loop in another position, as shown in Figure 5.2. It would mean increasing the complexity of the model definition, instead of the functions implemented.

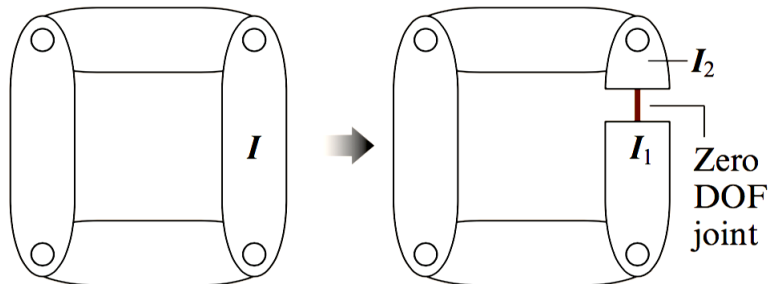


Figure 5.2: Example of virtual cutting a closed loop system to an equivalent one that respect the assumptions made.

The Equation of motion is solved directly. The Eq. (5.5), in this implementation is directly solved for the acceleration of the base, acceleration of joints and constraints; this would increment the computational time, especially if the time step is very small. Other solution for the equation are exposed by Featherstone and could be implemented in the future to increase the computational effectiveness.

5.2.5 Description of the Implemented Algorithm

In this section the algorithms implemented were briefly described.

calc_loopConstr. Table 5.1 shows the code to calculate \mathbf{K} and \mathbf{k} via Eq. (5.13), and \mathbf{k}_{stab} via Eq. (5.14).

These calculations involve combining vectors and matrices expressed in the inertial reference frame, which are the standard outputs for the already implemented SpaceDyn functions.

All the calculations are written in the 6D Vector notation, entirely compatible with the SpaceDyn library. The local variables ${}^I\mathbf{X}_p$ and ${}^I\mathbf{X}_s$ contain the Plücker transforms from inertial reference frame to the predecessor and successor frames respectively, of loop joint k . The expression ${}^I\mathbf{X}_p {}^I\mathbf{X}_s^{-1}$ is therefore the transform from the joint's predecessor frame to its successor frame, which is the input for `delta_calc`.

\mathbf{K} is calculated by first initialising the whole matrix to zero, and then calculating the non-zero submatrices. For each loop l , the submatrix \mathbf{K}_{li} is nonzero for every tree joint i that lies on the path of the loop. These quantities are calculated in a `while` loop that employs two loop variables, i and j . These variables are initially set to $p(k)$ and $s(k)$ and then stepped back toward the base in an order that guarantees they meet at the nearest common ancestor of $p(k)$ and $s(k)$. At this point, when $i = j$ the termination condition of the loop is reached, it is possible that i or j are zero, and this means that the base lies on the path of the closed loop: in this case the correspondent submatrix is filled.

j_calc. This function is used to calculate the joint transform ${}^I\mathbf{X}_j$ with respect to the inertial reference frame, the velocity \mathbf{v}_j and the acceleration \mathbf{a}_j of the joint expressed in 6D Space and inertial reference frame and also the motion subspace matrix \mathbf{S} .

The argument for `j_calc` are the body position, velocity and acceleration vectors already calculated by the SpaceDyn functions. The conversion in the Plücker notation is easily made by applying the its definition. For the motion subspace matrix, the only output expressed in the joint frame instead of inertial, it is necessary only to know the type of the joint:

$$\begin{array}{l} \text{Revolute} \\ \text{Joint (z)} \end{array} \mathbf{S} = \begin{bmatrix} 0 \\ 0 \\ 1 \\ 0 \\ 0 \\ 0 \end{bmatrix} \quad \begin{array}{l} \text{Prismatic} \\ \text{Joint (z)} \end{array} \mathbf{S} = \begin{bmatrix} 0 \\ 0 \\ 0 \\ 0 \\ 0 \\ 1 \end{bmatrix} \quad \begin{array}{l} \text{6-DoF} \\ \text{Joint (base)} \end{array} \mathbf{S}_0 = \mathbf{I}_6$$

delta_calc. Let ${}^s\mathbf{X}_p$ be the coordinate transform from the predecessor frame to the successor frame of a loop joint, as determined by the position variables of the spanning tree. In general, this transform will not comply exactly with the motion constraint imposed by the loop joint.

```

calc  $\mathbf{X}_0, \mathbf{v}_0, \mathbf{a}_0$ 
 $\mathbf{K} = \mathbf{0}, \mathbf{k} = \mathbf{0}$ 
for  $l = 1$  to  $N_l$ 
   $i = p(k)$ 
  calc  $\mathbf{X}_i, \mathbf{v}_i, \mathbf{a}_i$  → via j_calc
   $j = s(k)$ 
  calc  $\mathbf{X}_j, \mathbf{v}_j, \mathbf{a}_j$  → via j_calc
  calc  $\delta$  → via delta_calc
   $\mathbf{k}_{stab} = 2\alpha(\mathbf{v}_j - \mathbf{v}_i) - \beta^2\delta$ 
   $\mathbf{k}_l = -(\mathbf{a}_j - \mathbf{a}_i) - \mathbf{k}_{stab}$ 
  while  $i \neq j$ 
    if  $i > j$ 
       $\mathbf{K}_{li} = -\mathbf{X}_i \mathbf{S}_i$  → via j_calc
       $i = \text{BB}(i)$ 
    else
       $\mathbf{K}_{lj} = \mathbf{X}_j \mathbf{S}_j$  → via j_calc
       $j = \text{BB}(j)$ 
    end
  end
end
if  $i = 0$  or  $j = 0$ 
   $\mathbf{K}_0 = \mathbf{X}_0 \mathbf{S}_0$ 
end
end
end

```

Table 5.1: Code used to calculate the closed loops constraints.

The aim is to obtain expressions for the elements of \mathbf{X}_{err} , spatial vector that represent the error in position, in terms of ${}^s\mathbf{X}_p$. Given that this error vector is composed by small displacement, there exists a vector δ that approximate this error; each different joint type has different expressions for δ . As previously declared in Section 5.2.4, the closing loop joint has zero-DoF, so it is possible to define δ univocally from ${}^s\mathbf{X}_p$:

$$\delta = \frac{1}{2} \begin{bmatrix} X_{23} - X_{32} \\ X_{31} - X_{13} \\ X_{12} - X_{21} \\ X_{53} - X_{62} \\ X_{61} - X_{43} \\ X_{42} - X_{51} \end{bmatrix}$$

5.2.6 Code Testing

The implemented algorithm was verified with the use of Simpack: a simple model composed by a base and five links was considered in both

simulators. The closing joint was connecting the last link to the base and all the joint are revolute joints. Different types of inputs were applied: force or torque on the base and on the joints; after the simulations, the results were compared: the difference in terms of rotation of joints at the end of a 10 s simulation was minimal, in order of 0.1%. The huge difference is in the computational time: the Simulink integration is really slow compared to the fast Simpack simulation; the 10 s of simulation correspond in about 10 min in the first case, less then 1 s in the latter. Further implementations should deal with that.

5.3 Damping Control

As previously said in Section 5.1, the closed loop model was built to reduce the oscillation of the solar panel during the deorbit operations. The first simple analysis is to model a damper in each joint and grasp to the panel structure of Envisat.

A structure capable to sustain a certain amount of forces is the boom that connect Envisat to the solar panel; for this reason was chosen as a grasp target, otherwise grasping on one section of the solar panel would mean break it.

The grasping point is also an important parameter to analyse; if it is too close to panel the end effector motion could be too high and, consequently, the manipulator joint are not capable to support high torques, on the other side, a far grasping point would mean that only a small component of motion could be damped out. For this reason, two grasping position were taken in account:

- in the central part of the boom,
- in end part of it, close to the spherical joint that connect the boom to the panel.

Two different model previously analysed in the open loop configuration were modelled with closed loop; in the following pages there is the model description and the result of each analysis.

5.3.1 Clamping on Payload Adapter - Configuration 1

The first simulation with closed loops was made using the worst clamping configuration in terms of panel oscillation. As previously analysed, the oscillation of the solar panel tip were 1 m amplitude in x -direction and 2 m in z -direction, with respect to the Envisat reference frame.

In this model a damping torque was modelled in the joints of the robotic arm and the stiffness parameter used is $600 \text{ Nm}^2/\text{rad}$.

The angle used for the initial grasp position, in the middle of the 3 m long boom, are:

$$\mathbf{q} = [-109.1 \quad -61.5 \quad 198.1 \quad -103 \quad -44.7 \quad -22.8 \quad 147] [deg]$$

For the other grasping point, the angle chosen are:

$$\mathbf{q} = [-130 \quad -59.9 \quad 181 \quad -102.5 \quad -2.9 \quad -17.5 \quad 78.6] [deg]$$

These configurations are also shown in Figure 5.3.

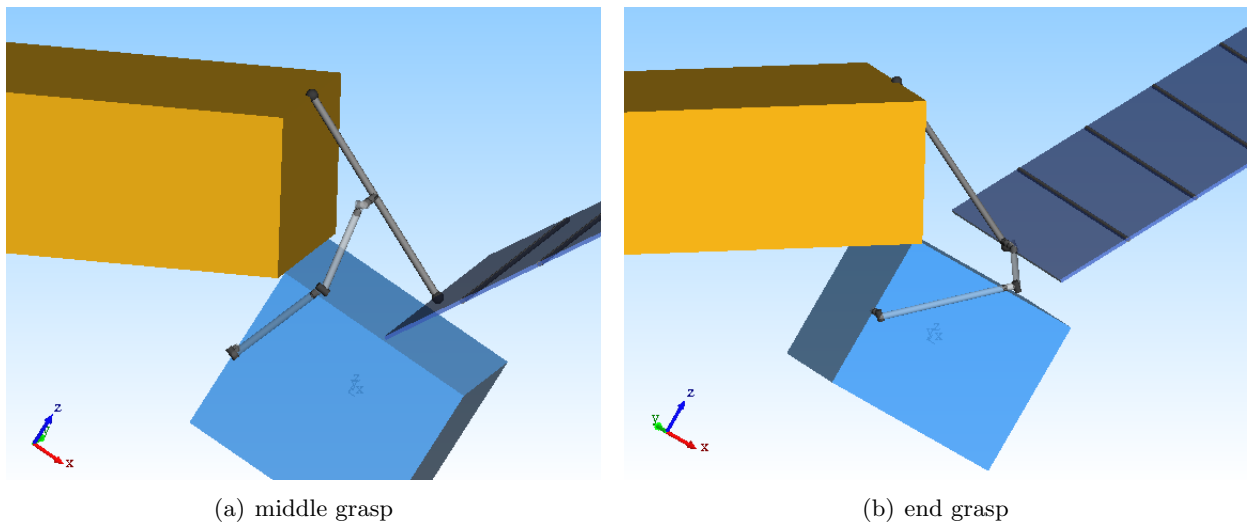


Figure 5.3: Model representations for the first configuration of the closed loops analysis.

As results of this simulation, the comparison of two positions is presented: the position of the end effector and the position of the grasping point in the open loop case, both expressed in the servicer reference frame (oriented as the inertial and located at CoG of the servicer). For both grasping configuration proposed, Figure 5.4 and Figure 5.5, the motion of this point in x - and z - direction is less in the closed loop model than in the open branch one, but an opposite trend is shown in y -direction. This because the forces acting in the second direction were zero without applying the closing loop constraint, on the other side, the constraint forces the boom to move in the y -axis, even though in the order of centimetres.

Another proposed result is the solar panel tip motion, Figure 5.6, the reference frame used is relative to Envisat. The goal is reached in both the grasping configurations, even if the y -component present the same behaviour as the boom: the movement is even more (about 10 cm), because it is propagated on the entire length of the panel.

The last plots, Figure 5.7 show the torques acting on the joint: this damping torque is higher in the first joint with respect to the others. It could be possible to optimise the initial joints angles in order to reduce it or try to use a slightly different model of that torque, for example an active control.

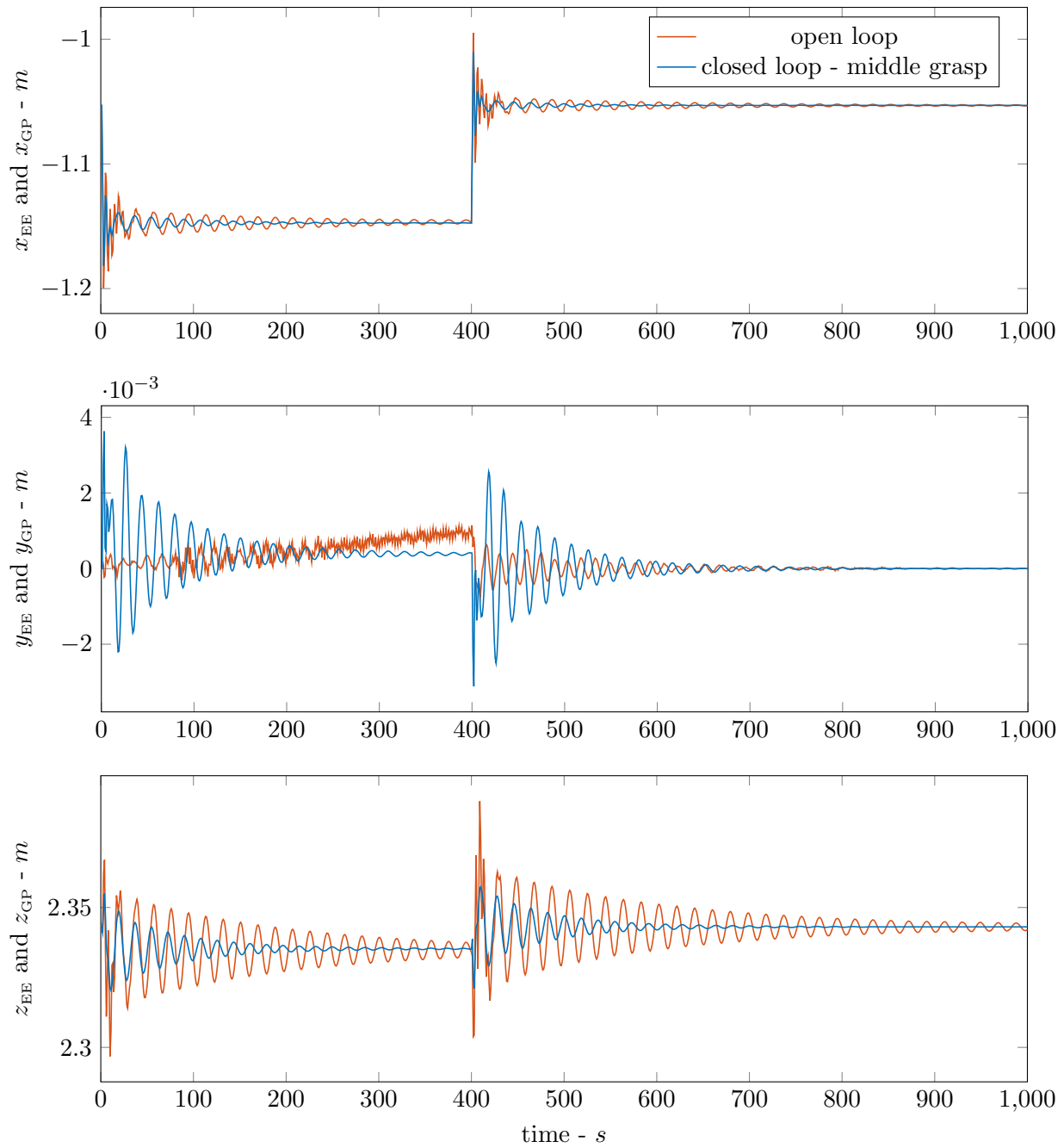


Figure 5.4: Position of the end effector of the manipulator in the closed loop simulation compared with the position of the grasping point in the open loop simulation; grasping point: middle of the boom.

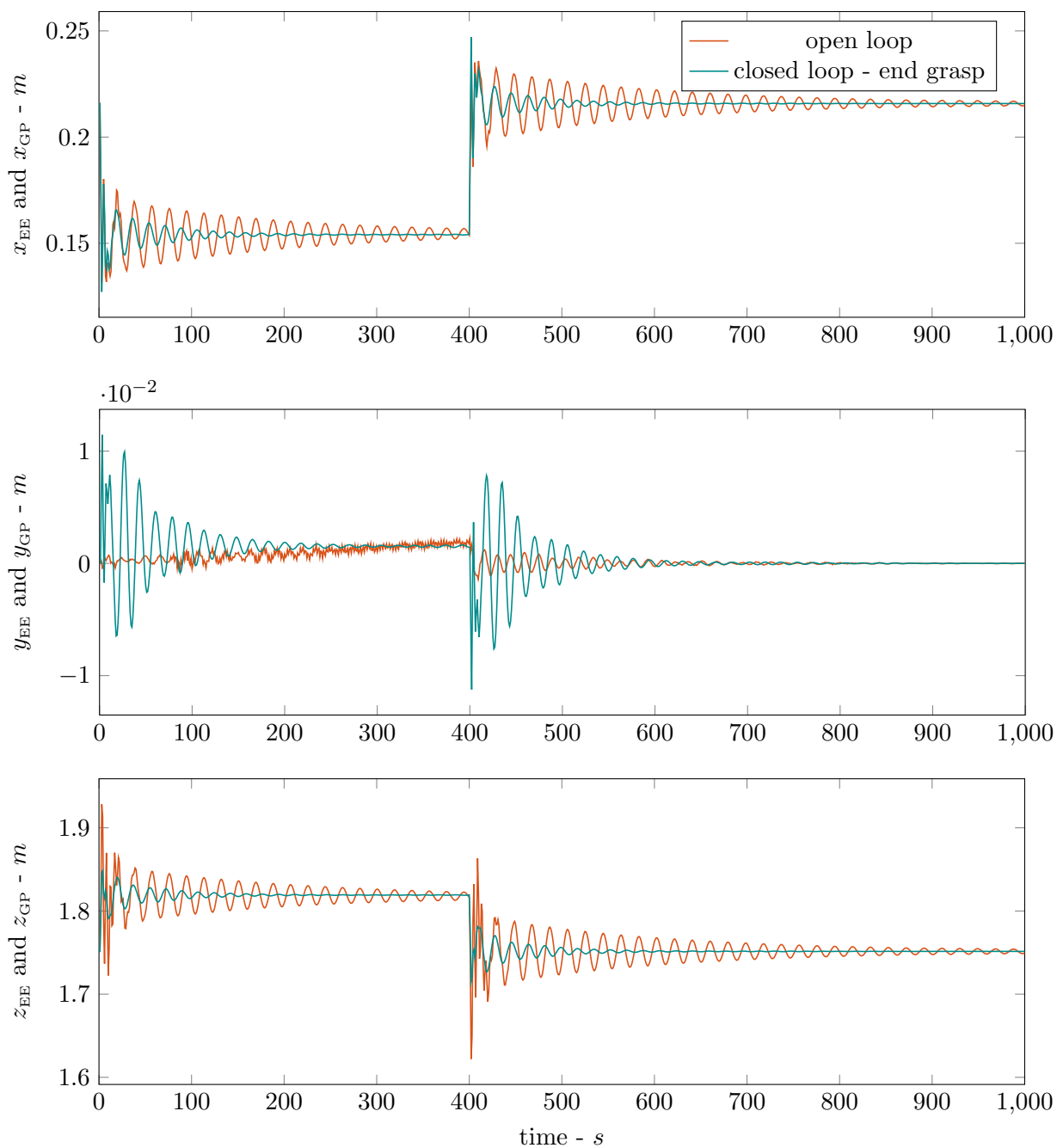


Figure 5.5: Position of the end effector of the manipulator in the closed loop simulation compared with the position of the grasping point in the open loop simulation; grasping point: end of the boom close to the first solar panel segment.

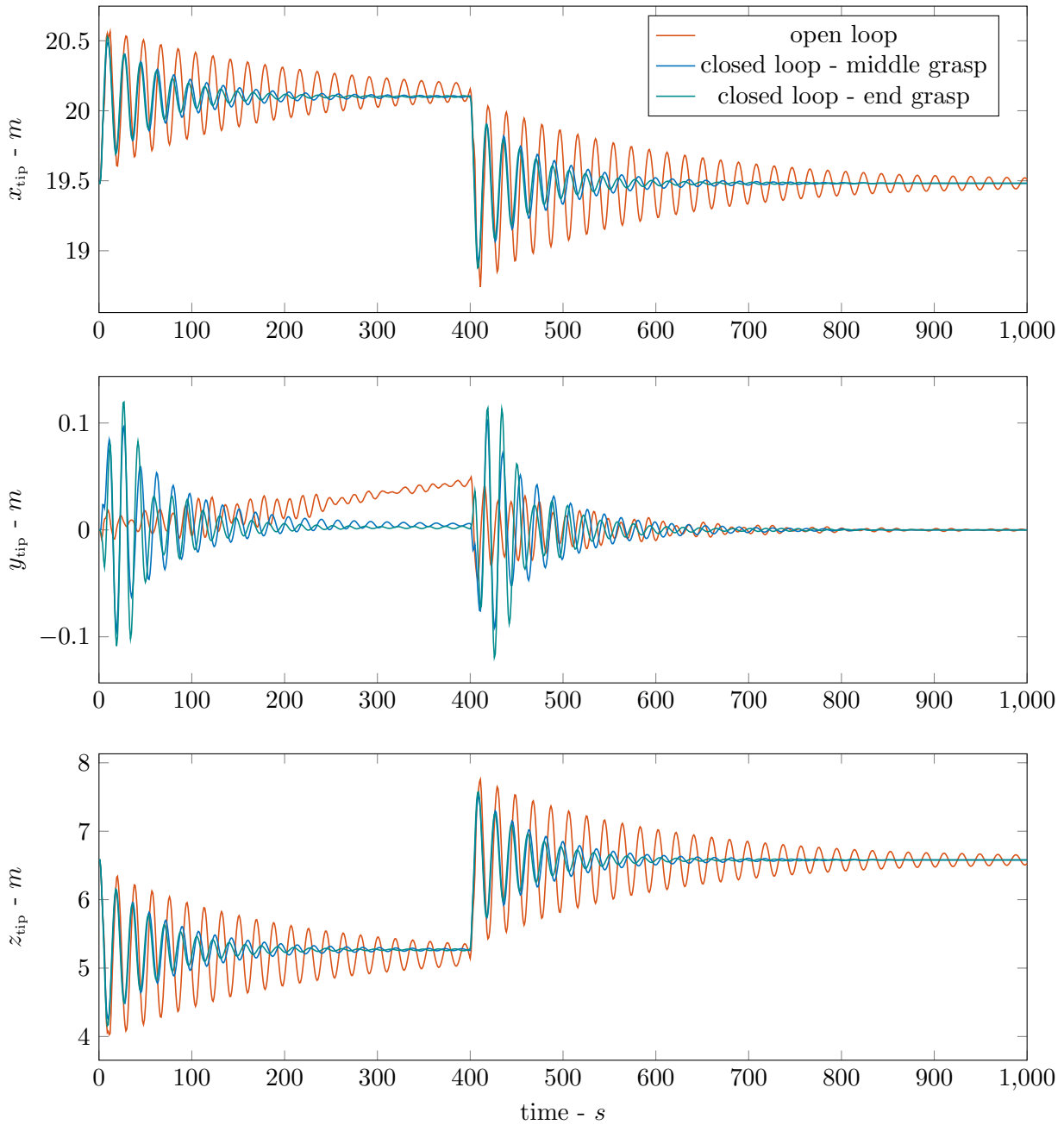
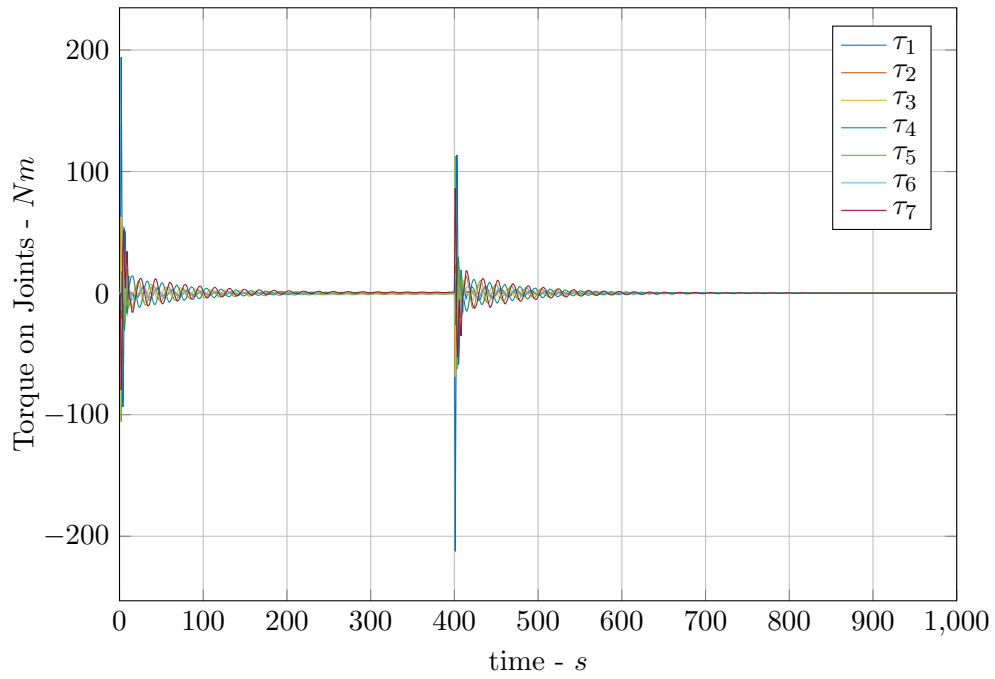
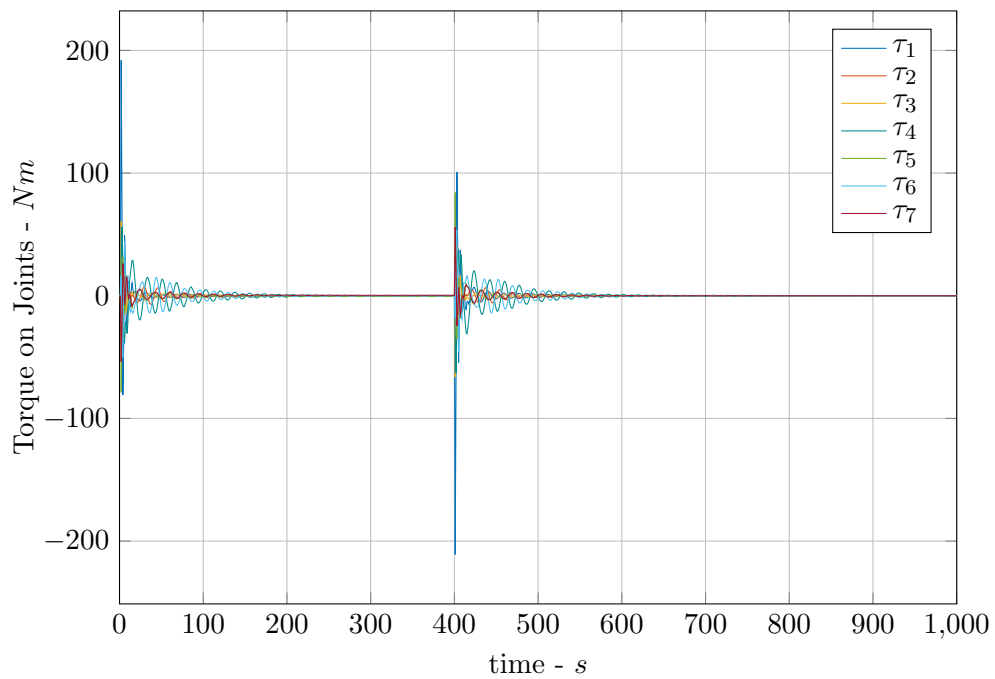


Figure 5.6: Position of the Envisat's solar panel tip.



(a) middle grasp



(b) end grasp

Figure 5.7: Torques in the joint produced by the passive damping of the solar panel oscillations.

5.3.2 Clamping on Payload Adapter - Configuration 2

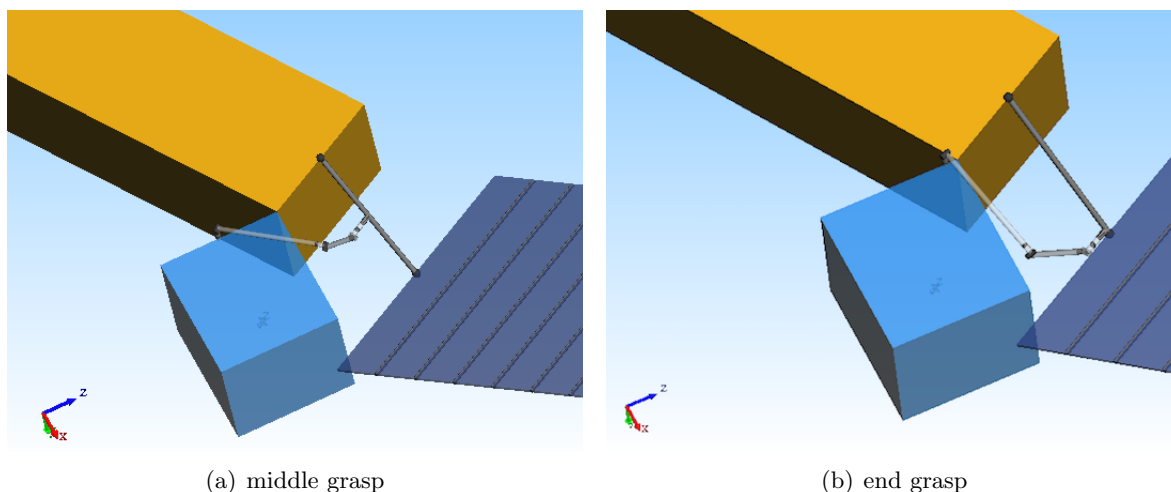


Figure 5.8: Model representations for the second configuration of the closed loops analysis.

A similar analysis was conducted on the other deorbiting configuration: the chaser is clamped to the payload adapter of Envisat and tilted of 90° . Both the grasping configurations were simulated and the angle of the manipulator joints are, for Figure 5.8(a):

$$\mathbf{q} = [50.1 \quad 91 \quad -40.9 \quad -90.1 \quad -115.6 \quad -52.3 \quad 127.7] [deg]$$

and for Figure 5.8(b):

$$\mathbf{q} = [22.7 \quad -124.4 \quad -44.4 \quad -67.9 \quad -120 \quad 49.4 \quad 146.7] [deg]$$

As shown on the results plot, this configuration is even better in terms of motion of the boom (Figure 5.9 and Figure 5.10), because every component is damped out with respect to the open loop configuration.

Also the panel oscillation, showed in Figure 5.11 in the Envisat reference frame, is damped and it is mostly independent from the grasping position choice.

Concerning the damping torques acting on the joints, the better configuration is the one that grasp the boom in its central part, as shown in Figure 5.12.

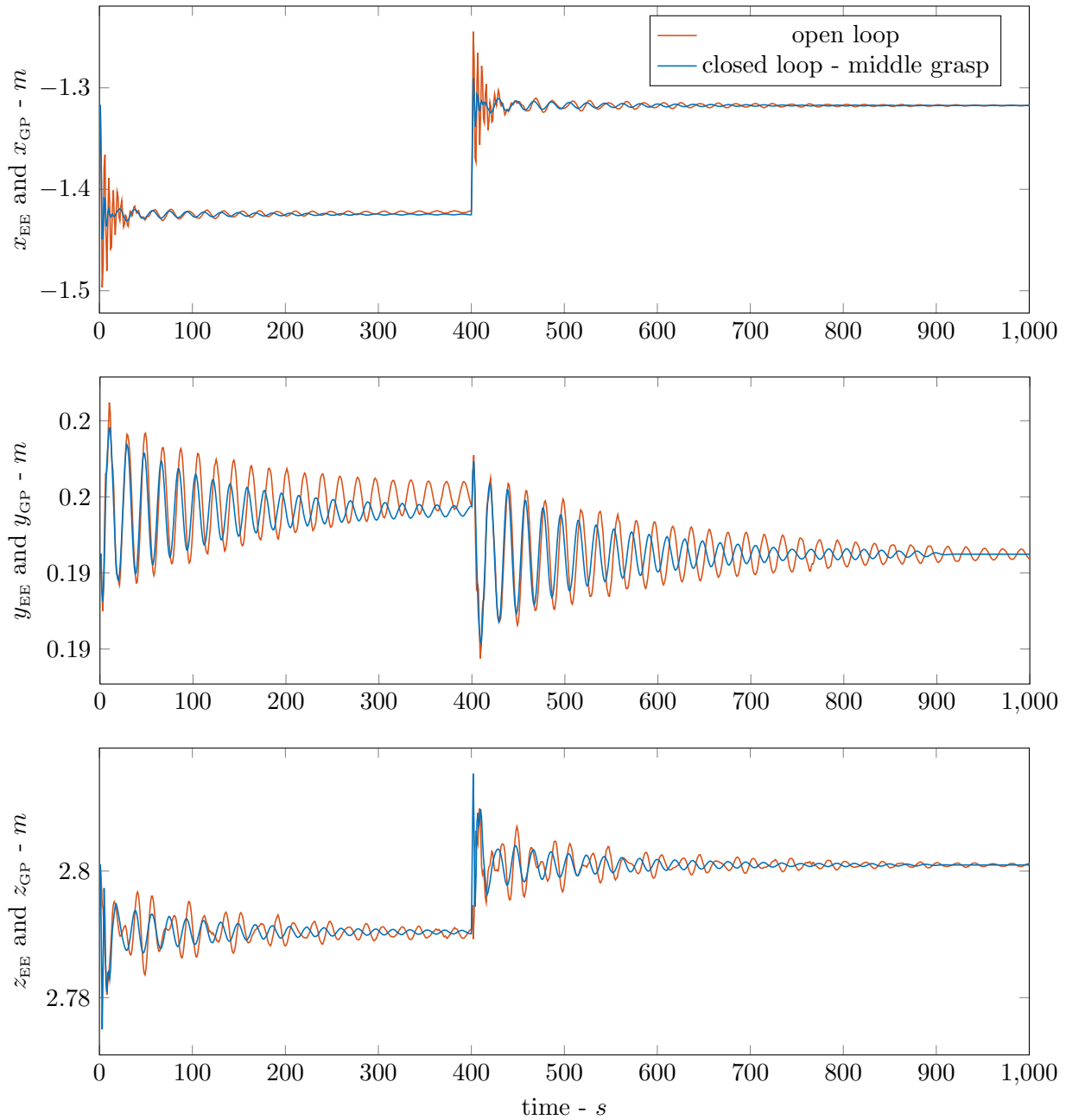


Figure 5.9: Position of the end effector of the manipulator in the closed loop simulation compared with the position of the grasping point in the open loop simulation; grasping point: middle of the boom; tilted clamping position.

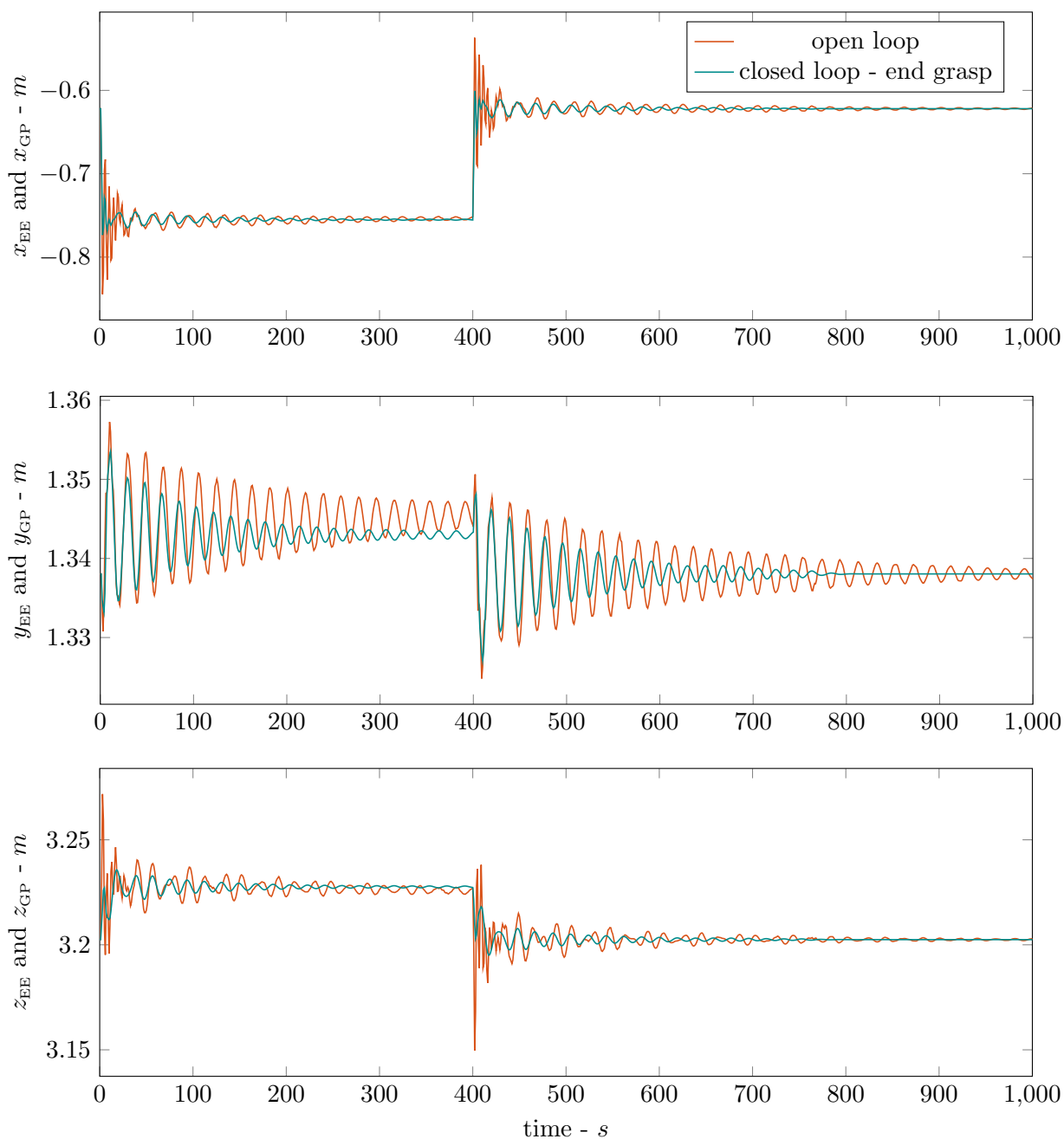


Figure 5.10: Position of the end effector of the manipulator in the closed loop simulation compared with the position of the grasping point in the open loop simulation; grasping point: end of the boom close to the first solar panel segment; tilted clamping position.

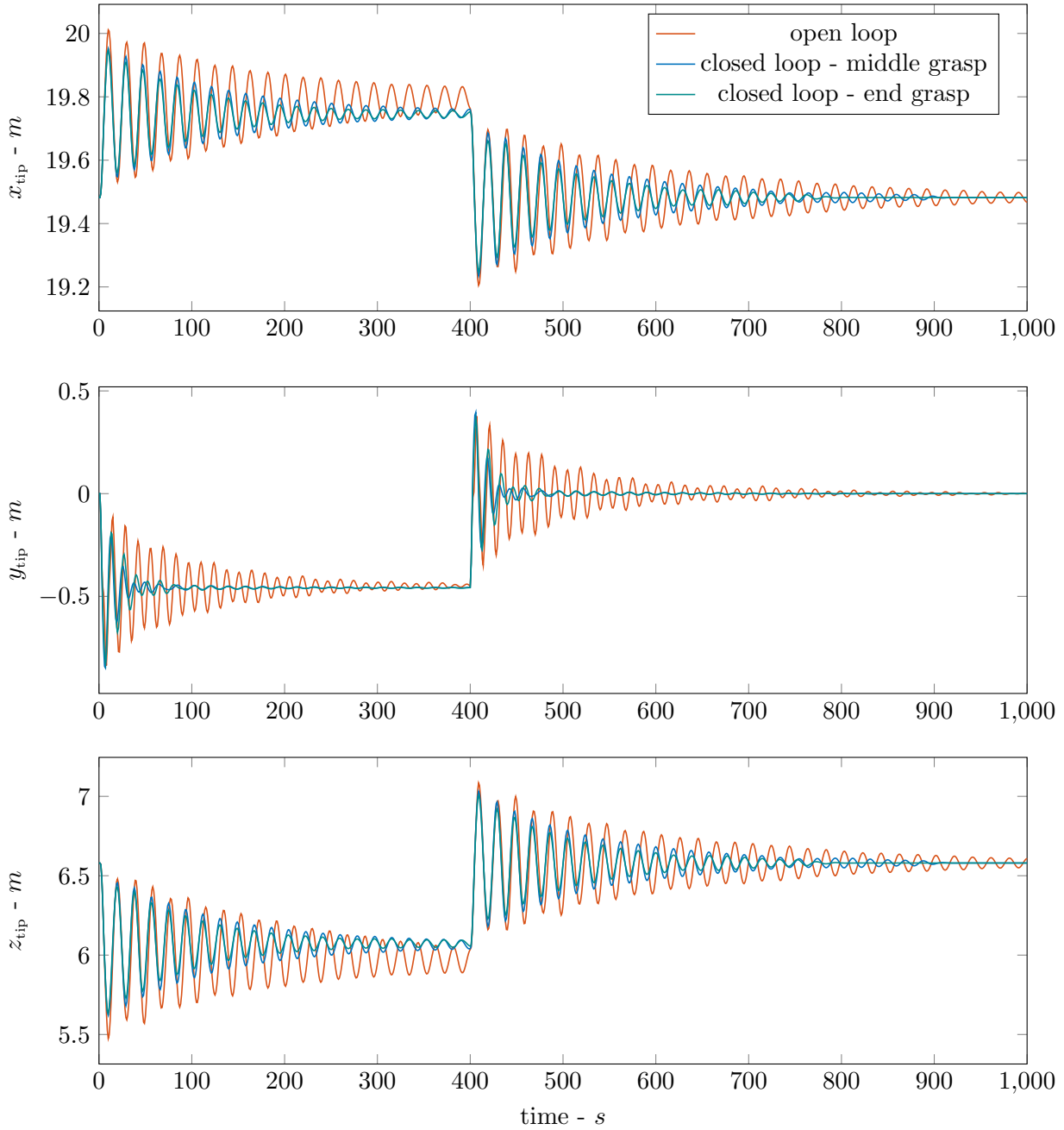
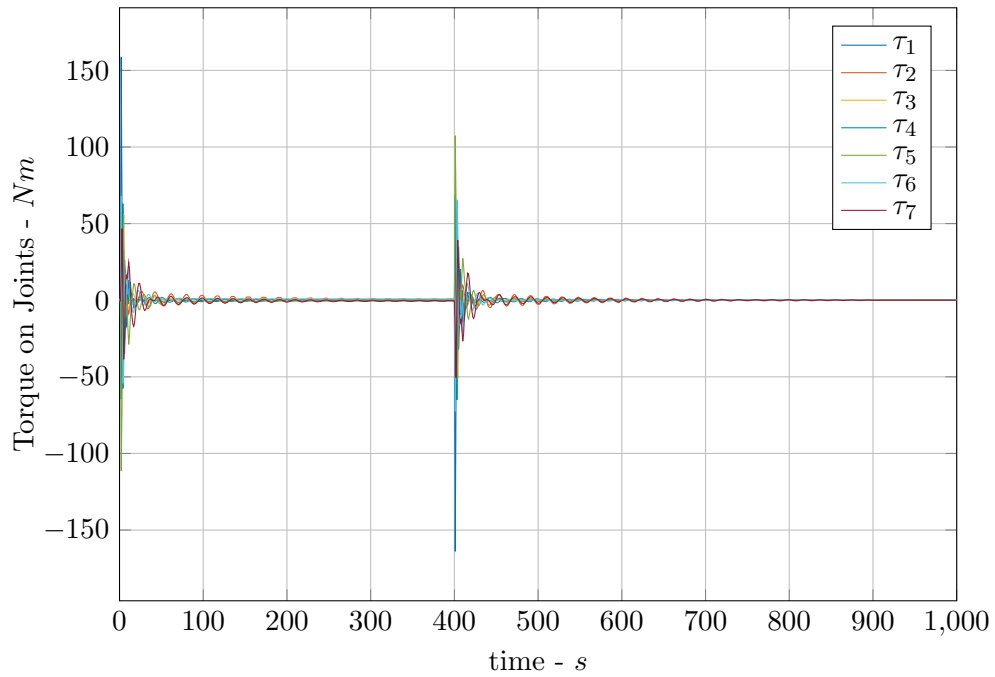
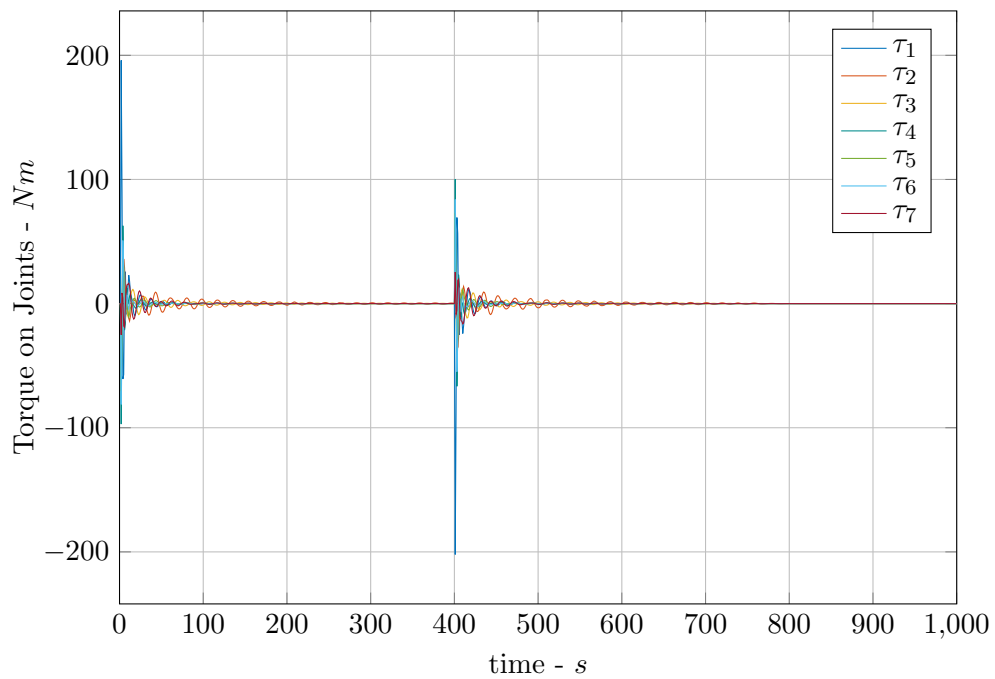


Figure 5.11: Position of the Envisat's solar panel tip; tilted clamping position.



(a) middle grasp



(b) end grasp

Figure 5.12: Torques in the joint produced by the passive damping of the solar panel oscillations; tilted clamping position.

Chapter 6

Conclusion & Future Work

6.1 Conclusions

This thesis focused on different aspects having a relevance for investigating an on-orbit servicing mission. As an example the European satellite Envisat was taken.

The first analysis about the detachment has shown that it is not possible to perform a deorbiting manoeuvre without considering a clamping mechanism. A detachment between the Servicer module and Envisat should be avoided in order to have the right control of the target during the thrust phase and also after that, between two burns of the thruster.

After considering that, the Phase A configuration was analysed: in terms of the simulation about the behaviour of the multi-body system, the results shown a deorbiting manoeuvre performed correctly. Thanks to the four point clamping mechanism, the two main bodies were strictly in contact during the mission. However, two main aspects should be considered: the stiffness of the structure exposed to the thrust force and the correct position of clamping. The first because the main body of Envisat was not built to sustain a lateral acceleration as provided by the Servicer (the internal structure of the bus is a cylinder with transversal flanges); the latter because a wrong position of the connection produces a wrong direction of thrust and a rotation of the target instead of a change of the orbit.

For these reasons, two different configurations were considered in the Phase B of the project. These avoid at least the structural problem considered before, because the clamping mechanism is attached to the payload adapter of Envisat: this was built to sustain the force during the launch and it is the right point to transfer the deorbiting force. However, the multi-body simulations shown a consistent oscillation of the solar panel both for the two clamping points analysed. The first configuration produces more than 2.5 *m* as panel tip motion, the second (tilted with respect to the previous) interests more the boom and the joint connected to it.

As an extension of this work, the detumbling manoeuvre to stabilise Envisat (supposed to rotate around one axis at $5^\circ/s$) was analysed as a phase just before the clamping and the deorbiting. A proposed grasping only with the robotic arm to the payload adapter of the target was simulated. The weakness of this manoeuvre is that the thrusters of the Chaser are producing small forces, but the lever arm is long (the robotic arm is 4.2 m) thus the torques in the joints are over the limits of the robotic arm and a clamping connection is necessary.

The main part of this work regards the closed loop analysis: the aim was to damp out the oscillation of the panel during the deorbiting phase (shown in the open chain configurations analysed). The inclusion of the theory in the algorithms of the library was a key point and the validation of the code with Simpack showed good performances of the code. Also the simulation with the closed loop configuration and a damping control showed promising results in terms of reducing the oscillation of the entire panel.

6.2 Future Works

The main weakness of the code implemented for the closed loop calculation is the computational time: this should be considered as a future aspect to improve to get faster integrations. It is also possible to do further implementations in order to include the complete Featherstone theory: considering the loop joints as active and of different types (Section 5.2.4).

Regarding the detumbling manoeuvre, a fixed configuration of the joint was considered and the manipulator cannot sustain that: in order to perform also this manoeuvre it could be possible to alternate the fixed joint motion with the release of rotation and a simultaneous zeroing the force.

The promising results obtained with the damping control in closed loop configuration could be improved. One way to do that could be to select a varying damping parameter, in order to reduce the torques when the oscillation are higher (at the beginning of the thrust phase and at the end of it); another way is to implement an active control of the end effector position and, knowing the position of the grasping point in the open chain configuration, give to the end effector an anti-phase oscillation.

Appendix A

Integration Methods

In this Appendix the solver used in the Simulink and in Simpack integrations are described.

Starting from Simulink, in order to obtain the right accuracy a variable-step solver was chosen; some attempts with the fixed-step integration solvers were done, but for the models with a lot of state variables to compute and with closed loop models (constrained stated) this type of integration produce a consistent numerical error and long simulations can not be performed.

Variable-step solvers dynamically vary the step size during the simulation. Each of these solvers increases or reduces the step size using its local error control to achieve the tolerances that you specify. Computing the step size at each time step adds to the computational overhead. However, it can reduce the total number of steps, and the simulation time required to maintain a specified level of accuracy.

The variable-step solvers use standard control techniques to monitor the local error at each time step. During each time step, the solvers compute the state values at the end of the step and determine the local error and the estimated error of these state values. They then compare the local error to the acceptable error, which is a function of both the relative tolerance (*rtol*) and the absolute tolerance (*atol*). If the local error is greater than the acceptable error for any one state, the solver reduces the step size and tries again.

- Relative tolerance measures the error relative to the size of each state. The relative tolerance represents a percentage of the state value. The default, 1e-3, means that the computed state is accurate to within 0.1%; this default value was used for the simulations done.
- Absolute tolerance is a threshold error value. This tolerance represents the acceptable error as the value of the measured state approaches zero; the value chosen for this threshold was 1e-3, too.

The problem analysed is a stiff one, for this reason `ode15s` was selected. `ode15s` is a variable-order solver based on the numerical differentiation formulas (NDFs). NDFs are related to, but are more efficient than the backward differentiation formulas (BDFs), which are also known as Gear's method.

For the `ode15s` solver, it is possible to choose the maximum order of the numerical differentiation formulas (NDFs) that the solver applies. Since the `ode15s` uses first- through fifth-order formulas, the Maximum order parameter allows you to choose 1 through 5. For that case, the order 2 was selected.

For the software Simpack, the default integrator was used, SODASRT 2. This is very fast, accurate and robust, for example it can start from extreme non-equilibrium situations. Its main features are:

- allows constraints and algebraic states,
- is suitable for stiff models,
- allows root functions,
- is possible to set the maximum order of errors.

SODASRT 2 is based on Backward Differentiation Formula (BDF), an implicit multistep integration scheme. The high efficiency of this integrator is the basis of the small computational time of Simpack compared to Simulink. The order of maximum error chosen was $1e-3$; all the other parameters were selected as default. It is also possible to use parallel solver, for this work sometimes this option was used: this reduce even more the computational time.

References

- [1] IADC, *IADC Space Debris Mitigation Guidelines*, 2007.
- [2] J.C. Liou, *Modeling the Large and Small Orbital Debris Populations for Environment Remediation*, Third European Workshop on Space Debris Modeling and Environment Remediation, CNES HQ, Paris, France, 16-18 June 2014.
- [3] M. Castronuovo, *Active Space Debris Removal — A Preliminary Mission Analysis and Design*, *Acta Astronautica*, [vol. 69, pp 848–859], 2011.
- [4] J.C. Liou, N.L. Johnson, *A Sensitivity Study of the Effectiveness of Active Debris Removal in LEO*, *Acta Astronautica*, [vol. 64, pp 236–243], 2009.
- [5] K. Yoshida, *Space Robot Dynamics and Control: to Orbit, from Orbit, and Future*, The Ninth International Symposium of Robotics Research, 1999.
- [6] A. Albu-Schaeffer, W. Bertleff, B. Rebele, B. Schaefer, K. Landzettel, G. Hirzinger, *ROKVISS – Robotics Component Verification on ISS Current Experimental Results on Parameter Identification*, 2006 IEEE Robotic Space Journal - International Conference on Robots and Automation, Orlando, Florida, May 2006.
- [7] G. Hirzinger, N. Sporer, A. Albu-Schaeffer, M. Hdmle, R. Krenn, A. Pascucci, M. Schedl, *DLR's Torque-Controlled Light Weight Robot III - Are We Reaching the Technological Limits Now?*, 2002 IEEE Robotic Space Journal - International Conference on Robots and Automation, Washington, DC, May 2002.
- [8] R. Lampariello, G. Hirzinger, *Generating Feasible Trajectories for Autonomous On-Orbit Grasping of Spinning Debris in a Useful Time*, 2013 IEEE Robotic Space Journal - International Conference on Intelligent Robots and Systems, Tokyo, Japan, 3-7 November 2013.

-
- [9] K. Landzettel, C. Preusche, A. Albu-Schaeffer, D. Reintsema, B. Rebele, G. Hirzinger, *Robotic On-Orbit Servicing - DLR's Experience and Perspective*, 2006 IEEE Robotic Space Journal - International Conference on Intelligent Robots and Systems, Beijing, China, 9-15 October 2006.
- [10] R. Lampariello, *On Grasping a Tumbling Debris Object with a Free-Flying Robot*, 19th IFAC Symposium on Automatic Control in Aerospace, 2013.
- [11] M. Mejia-Kaiser, *ESA's Choice of Futures: Envisat Removal or First Liability Case*, 63rd IAC - International Astronautical Congress, 2012.
- [12] OHB, *Target Analysis Report*, e.Deorbit Mission Phase B1, EDE-B1-OHB-RP-009, 2016.
- [13] R. Zwanenburg, *The Qualification Test Programme of the Envisat Solar Array Mechanism*, 6th European Space Mechanism and Tribology Symposium, Zurich, Switzerland, 4-6 October 1995.
- [14] M. Wieser, R. Haarmann, G. Hausmann, J.C. Meyer, S. Jaekel, M. Lavagna, R. Biesbroek, *e.Deorbit Mission: OHB Debris Removal Concepts*, ASTRA 2015 - 13th Symposium on Advanced Space Technologies in Robotics and Automation, ESA/ESTEC Noordwijk, the Netherlands, 11-13 May 2015.
- [15] S. Jaekel, R. Lampariello, G. Panin, M. Sagardia, B. Brunner, O. Porges, E. Kraemer, M. Wieser, R. Haarmann, M. Pietras, R. Biesbroek, *Robotic Capture and Deorbit of a Heavy, Uncooperative and Tumbling Target Satellite in Low Earth Orbit*, ASTRA 2015 - 13th Symposium on Advanced Space Technologies in Robotics and Automation, ESA/ESTEC Noordwijk, the Netherlands, 11-13 May 2015.
- [16] Philipp Gahbler, R. Lampariello, J. Sommer, *Analysis of a Deorbiting Manoeuvre of a Large Target Satellite Using a Chaser Satellite With a Robot Arm*, ASTRA 2015 - 13th Symposium on Advanced Space Technologies in Robotics and Automation, ESA/ESTEC Noordwijk, the Netherlands, 11-13 May 2015.
- [17] I. Stroe, S. Staicu, A. Craifaleanu, *Internal Forces Calculus of Compass Robotic Arm Using Lagrange Equations*, ASTRA 2011 - 11th Symposium on Advanced Space Technologies in Robotics and Automation, ESA/ESTEC Noordwijk, the Netherlands, 12-14 April 2011.
- [18] S. Graham Kelly, *Mechanical Vibrations: Theory and Applications*, SI Edition, 2012.

-
- [19] Singiresu S. Rao, *Mechanical Vibrations*, Prentice Hall, 2011.
- [20] K. Yoshida, *The SpaceDyn: a MATLAB Toolbox for Space and Mobile Robots*, Department of Aeronautics and Space Engineering, Tohoku University, 1999.
- [21] R. Lampariello, S. Abiko, G. Hirzinger, *Dynamics Modeling of Structure-Varying Kinematic Chains for Free-Flying Robots*, 2008 IEEE International Conference on Robotics and Automation, Pasadena, California USA, 19-23 May 2008.
- [22] S. A. A. Moosavian, E. Papadopoulos, *Free-Flying Robots in Space: an Overview of Dynamics Modeling, Planning and Control*, Robotica, 2007.
- [23] Y. Ishijima, D. Tzeranis, S. Dubowsky, *The On-orbit Maneuvering of Large Space Flexible Structures by Free-Flying Robots*, Proceedings of ISAIRAS 2005.
- [24] Abhinandan Jain, *Robot and Multibody Dynamics - Analysis and Algorithms*, Springer, 2011.
- [25] G. Rekleitis, E. Papadopoulos, *On On-Orbit Passive Object Handling by Cooperating Space Robotic Servicers*, 2011 IEEE Robotic Space Journal - International Conference on Intelligent Robots and Systems, San Francisco, California USA, 25-30 September 2011.
- [26] G. Rouleau, I. Rekleitis, R. L'Archeveque, E. Martin, K. Parsa, E. Dupuis, *Autonomous Capture of a Tumbling Satellite*, 2006 IEEE International Conference on Robotics and Automation, Orlando, Florida USA, 15-19 May 2006.
- [27] K. Seweryn, M. Banaszkiwicz, B. Maediger, T. Rybus, J. Sommer, *Dynamics of Space Robotic Arm During Interactions with Non-Cooperative Objects*, ASTRA 2011 - 11th Symposium on Advanced Space Technologies in Robotics and Automation, ESA/ESTEC Noordwijk, the Netherlands, 12-14 April 2011.
- [28] G. Rekleitis, E. Martin, G. Rouleau, Re. L'Archeveque, K. Parsa, E. Dupuis, *Autonomous Capture of a Tumbling Satellite*, Journal of Field Robotics, Wiley InterScience, 2007.
- [29] O. Ruf, *Dynamic Modelling of Robots with Kinematic Loops*, Master Thesis, 2014.
- [30] R. Featherstone, *Rigid Body Dynamics Algorithms*, Springer, 2008.
- [31] B. Siciliano, O. Khatib, *Springer Handbook of Robotics*, Springer, 2008.

- [32] J. Cortes, *Motion Planning Algorithms for General Closed-Chain Mechanisms*, Doctorat de l'Institut National Polytechnique de Toulouse Ecole Doctorale Systemes, 2003.
- [33] Y. Nakamura, K. Yamane, *Dynamic Computation of Structure-Varying Kinematic Chain and its Application to Human Figures*, IEEE Transactions on Robotics and Automation, 2000.
- [34] R. Featherstone, *Robot Dynamics Algorithms*, The Springer International Series in Engineering and Computer Science Series, Kluwer Academic Pub, 1987.
- [35] K. W. Lilly, C. S. Bonaventura, *A Generalized Formulation for Simulation of Space Robot Constrained Motion*, 1995 IEEE International Conference on Robotics and Automation, 1995.
- [36] S. Abiko, R. Lampariello, G. Hirzinger, *Impedance Control for a Free-Floating Robot in the Grasping of a Tumbling Target with Parameter Uncertainty*, IEEE International Conference on Intelligent Robots and Systems, Beijing, China, 9-15 October 2006.